UNIVERSIDADE DE LISBOA
INSTITUTO SUPERIOR TÉCNICO

Design, Development, and Integration of a Flexible Array of Magnetoresistive Sensors for Tactile Sensing

Miguel Sérgio de Abreu Neto

Supervisor: Doctor Susana Isabel Pinheiro Cardoso de Freitas

Co-supervisor: Doctor Alexandre José Malheiro Bernardino

Thesis approved in public session to obtain the Ph.D. Degree in

Leaders for Technical Industries

Jury final classification: **PASS**

2021

UNIVERSIDADE DE LISBOA

INSTITUTO SUPERIOR TÉCNICO

Design, Development, and Integration of a Flexible Array of Magnetoresistive Sensors for Tactile Sensing

Miguel Sérgio de Abreu Neto

Supervisor: Doctor Susana Isabel Pinheiro Cardoso de Freitas

Co-supervisor: Doctor Alexandre José Malheiro Bernardino

Thesis approved in public session to obtain the Ph.D. Degree in

Leaders for Technical Industries

Jury final classification: **PASS**

Jury

Chairperson: Doctor Hélder Carriço Rodrigues, Instituto Superior Técnico, Universidade de Lisboa

Members of the Committee:

Doctor: Paulo Jorge Peixeiro de Freitas, Instituto Superior Técnico, Universidade de Lisboa, em cedência de funções ao International Iberian Nanotechnology Laboratory, Braga

Doctor: Lorenzo Jamone, School of Electronic Engineering and Computer Science, Queem Mary University of London, UK;

Doctor: Susana Isabel Pinheiro Cardoso de Freitas, Instituto Superior Técnico, Universidade de Lisboa

Doctor: Gonçalo Nuno Gomes Tavares, Instituto Superior Técnico, Universidade de Lisboa;

Doctor: Alexandre Manuel Teixeira de Barros Ferreira da Silva, Escola de Engenharia, Universidade do Minho

Funding Institutions

Fundação para a Ciência e Tecnologia and MIT Portugal

I declare that this document is an original work of my own authorship and that it fulfills all the requirements of the Code of Conduct and Good Practices of the *Universidade de Lisboa*.

Acknowledgments

I was fortunate to have received a great deal of support and compassion. Such an ambitious project required me to learn and constantly adapt, which was only possible with the support and patience of the people who helped throughout this period.

I would first like to thank my supervisor, Professor Susana Freitas, whose expertise was invaluable in formulating the research questions and methodology. Your insightful feedback pushed me to sharpen my thinking and brought my work to a higher level.

I would particularly like to single out my co-supervisor at ISR, Professor Alexandre Bernardino. I want to thank you for your patient support and for all of the opportunities I was given to further my research. A special thank you to Ricardo Nunes, who was essential in prototyping the first devices.

I would also like to thank my tutors, Dr. Paulo Freitas, Dr. Lorenzo Jamone, and Dr. Manuel Heitor, for their valuable guidance throughout my studies. You provided me with the tools that I needed to choose the right direction and complete my dissertation.

Colleagues have a central role in the discussion and development of ideas, and I have always been very fortunate to be surrounded by people I learned so much from over the years. Some of the most relevant are Pedro Ribeiro, Marilia Silva, Fernando Franco, João Valadeiro, Paulo Francisco, and Diogo Rechena, who provided stimulating discussions and support over long periods of time. There were so many other colleagues, from younger to senior, that left an impact. Hopefully, we can catch up after you read this.

It would have been impossible without the emotional stability my family and friends provided me throughout the years. Thank you for happy distractions to rest my mind outside of my research. A special thank you to Ana and my parents for their wise counsel and sympathetic ear. Overall, you are always there for me. The unconditional love from family and friends was essential to go through the most challenging times.

I will forever be grateful for this opportunity. I got to know myself and all of you in the process. It was a pleasure.

Thank you for everything,

Miguel Neto

Abstract

The development of tactile sensors systems can provide critical information that will enable humanoid robots, such as Vizzy, to perform grasping and object manipulation actions. Magnetic tactile sensors measure a change in the magnetic field resulting from an applied mechanical force. Several approaches use magnetics to estimate the applied force, and we particularly describe and discuss the most common one. The method involves embedding a magnet in an elastomeric part and using a sensor to detect its displacement in space. The drawback of this approach is that the applied force can cause the magnet to tilt, which can significantly influence the estimation of the applied force. The advantages of magnetic tactile sensors over competing technologies are their low cost, low hysteresis, ease to fabricate, and robustness.

Our approach combines flexible arrays of magnetoresistive (MR) sensors distributed across the finger surface with a fixed magnet on the finger part. Each output allows us to infer the sensor position in space and reconstruct the tactile sensor surface. As opposed to previously available solutions in the literature of this design, the significant advantage is its ability to detect the contact areas and track the variation of contact points.

From an engineering design and manufacturing perspective, the main challenge is in the fabrication of this novel sensor design is the placement of the sensors on the surface of the finger, as opposed to embedding a permanent. We developed manufacturing processes for flexible electronics to read the sensor's output to meet the mechanical, electronic, and magnetic requirements.

We designed and fabricated a flexible 4x2 matrix of Si chips of magnetoresistive spin valve sensors that, coupled with a single small magnet, can measure contact forces from 0.1 to 5 N on multiple locations over the surface of a robotic fingertip. : this design is innovative concerning previous works in the literature, and it is made possible by careful engineering and miniaturization of the custom-made electronic components that we employ. In addition, we characterize the behavior of the sensor through a COMSOL simulation, which can be used to generate optimized designs for sensors with different geometries.

Keywords

Magnetic Tactile Sensors ; flexible arrays of magnetoresistive sensors; robot finger integration

Resumo

O desenvolvimento de sensores táteis e de pressão é um requisito para fornecer dados que, em última análise, permitirão que robôs humanóides, como o Vizzy, manipulem objetos. Neste trabalho, focamos nos sensores táteis magnéticos, cujo princípio de funcionamento se baseia na medição indireta da distância entre um ímã e um sensor na compressão, traduzida pela variação de tensão do sensor. As vantagens sobre as tecnologias concorrentes são seu baixo custo, baixa histerese, fácil de fabricar e robustez. A desvantagem dessa abordagem é que a força aplicada pode fazer com que o ímã incline, resultando em uma variação do campo magnético que não pode ser distinguida, resultando em um erro de medição, porque essa alteração será interpretada como um movimento linear.

Esta abordagem combina matrizes flexíveis de sensores magnetoresistivos (MR) distribuídos pelo dedo com ímã fixo no dedo. Cada saída do sensor é usada para inferir sua posição no espaço em relação a um ímã fixo, resolvendo o problema inverso, permitindo assim a reconstrução da superfície do dedo. A principal vantagem, em oposição às soluções disponíveis anteriormente na literatura deste projeto, é sua capacidade de detectar as áreas de contato e rastrear a variação dos pontos de contato durante a manipulação, calculando a posição de todos os sensores na matriz, permitindo a determinação do contato. ponto e a área total de contato, aproximando os sensores táteis magnéticos de um passo para permitir a manipulação de objetos em robôs do que nunca.

Palavras-chave

Sensores táteis magnéticos; matrizes flexíveis de sensores magnetoresistivos; integração de dedo do robô

Table of Contents

List of Figures

List of Tables

Chapter 1

Designing a tactile system

1.1 Motivation

Sensorial perception plays a critical role in understanding our environment and has gone through an evolutionary process to acquire information vital for preserving our existence and wellbeing. The Umwelt, the world as a particular organism experiences it, is a mixture of sensorial perception and reasoning. The actions of an organism are a function of its Umwelt, making the relationship between perception, reasoning, and action a fascinating but highly complex topic. This complexity manifests itself in the numerous areas and methodologies that several scientific fields adopt to describe these relationships, such as biology, psychology, and all types of behavioral sciences.

A human has five senses: vision, hearing, taste, smell, and touch, from which vision and touch are essential for actively manipulating external objects. Humans have shaped their environment, and tactile sensing has helped us develop and use tools for millennia. Successful grasping and object manipulation allowed us to build and use tools to improve the efficiency and extent of our actions. Today, examples of our ability to act and change our environment are all around us.

Humanoid robots are a futuristic idea since early computers, and even though we have some working proof of concepts, creating a humanoid robot to help us in our daily tasks has proven to be highly challenging. Robotic arms and more complex machines are very appealing for industrial environments because they excel in precise and repeatable tasks, which are the majority of factory operations. However, outside the factories, we strive to tailor our environment to maximize our well-being. We design new objects, tools, processes, and forms of interacting with reality at an ever-increasing rate, making the variability of the environment a significant challenge.

Vision-based systems have evolved significantly, especially in image processing capabilities for image recognition and collision avoidance. These goals have shown great promise for mobility for robots, drones, and other unmanned vehicles, especially when communicating to deal with the environment variability. Grasping and object manipulation are complex tasks that can benefit from spatial awareness and image recognition but require tactile information to supply extra sensorial information. This synergy between vision and tactile systems requires parallel development and integration to benefit from each other.

This thesis describes the design process of a new tactile system to support Vizzy in grasping and object manipulation tasks. Chapter 1 discusses the state of the art of humanoids hands and tactile sensing requirements. Chapter 2, a detailed state of the art on magnetic tactile sensors and their working principle is discussed, and novel design is proposed. Chapter 3 describes each iteration phase of the sensor design and fabrication process and electronic interface. Chapter 4 focuses on the results from the last version of the sensor and the discussion of its significance. Finally, Chapter 5 is the conclusion and final remarks.

1.2 Who cares?

Vizzy is a humanoid robot designed to interact with human beings, requiring, amongst other things, such as greeting, offering, receiving, and manipulating objects. All these tasks require accurate tactile feedback during the interaction so that the appropriate decision can follow up. It is not a trivial task because it requires the successful coordination of body parts (i.e. head and eyes, arm, hand, fingers) and sensory channels (i.e. vision, touch, proprioception) [1].

Object manipulation is a continuous cycle, where the robot must evaluate the situation, devise action, and adapt depending on the feedback to reach the desired result. The interdependency between the sensory channels and movement freedom (i.e. position and precision of the motors, number of motors) is an important design aspect. The higher the number of movements possibilities, the more possibilities it must choose from, which requires better decision-making processes, requiring better sensory channels, and information processing.

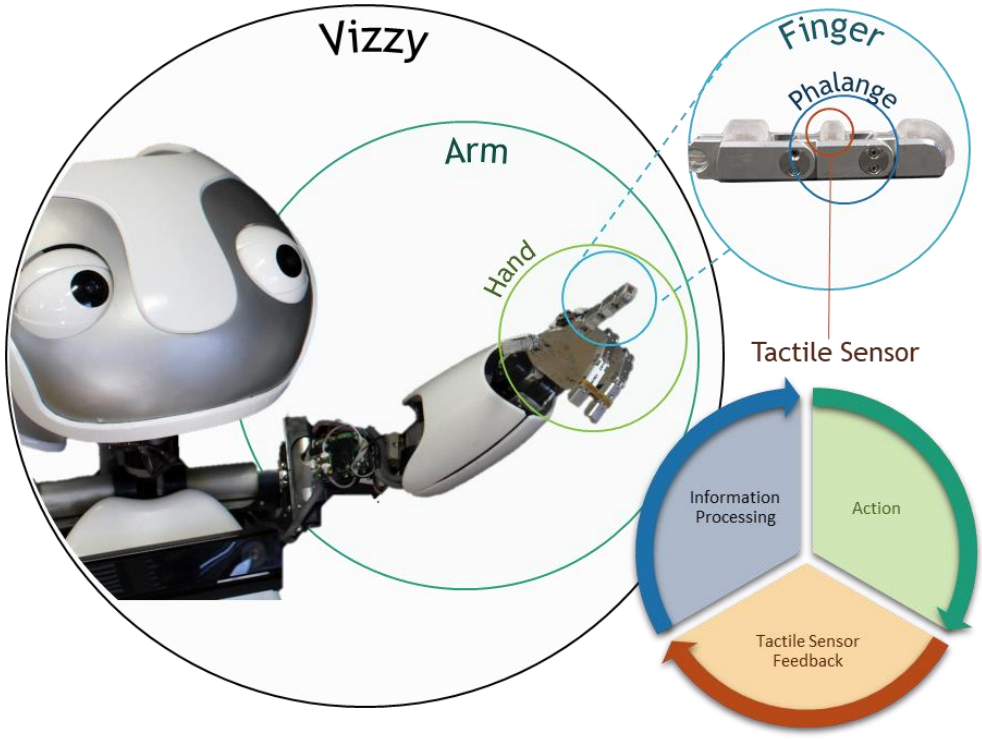

Figure 1 – Vizzys' left arm, hand, finger, and motors required on the shoulder, elbow, and hand. Continuous cycle from acquiring the signal from the tactile sensor, processing and extracting meaning from the sensor output, and decision-making process for a new action.

Designing and developing a tactile system must account for the interdependency of a tactile system with other sensory channels and movement freedom. This complexity makes it very challenging from a scientific and engineering point of view because it requires a multi-disciplinary background. The most common approaches in the academic literature are to manage complexity are either to discard the

sensor variability and use commercially available sensors or the design and development of new sensors and working principles and not focus on the robot integration.

The first type of research focuses primarily on taking the most from the commercially available sensors, so the advantage lies in the information processing method rather than the sensor. The second focuses primarily on the sensor working principle, so the discussions are targeted for the information, measurement accuracy, and sources of error, while implementation in the robotic hand is rarely a matter of focus.

The commercial sensors provide higher technology readiness solutions but lower potential to significantly design new solutions and working principles to improve the system. The majority of improvements are usually incremental and dependent on artificial intelligence and information processing algorithms. In contrast, the second approach can design new sensor concepts. However, the integration complexity (i.e. number of wires and analog-digital interfaces), low technology readiness, and multidisciplinary required to design such systems make the number of occasions they are integrated on the robot very rare.

This thesis mainly falls into the second approach of designing a new tactile sensor system but has a strong commitment to integrating the sensor in a robot, Vizzy in this case. We propose a novel magnetic tactile sensor from a conceptual perspective and design, fabricate, partially integrate, test, and characterize it. The main challenge this work raises relies on the multidisciplinarity of the work, from defining valuable information for the robot without compromising the feasibility of the design. The discussion on valuable information is detailed in Chapter 1, while the design and integration challenges details are in Chapter 2. However, because we have yet to attempt object manipulation with this sensor, more comprehensive testing is required to determine the proposed concept's potential fully.

1.3 Requirements for tactile systems

As of today, most robots are built “in-house” resulting in unique geometrical and application requirements. The low standardization brings an extra layer of complexity since it can be hard to generalize or compare integration solutions and/or working principles. Their uses can be as broad as human prostheses or parts of robots that perform assistive, military, medical, or industrial functions.

Nevertheless, the goal of the tactile system is to provide the correct information for grasping and object manipulation. Grasping can be defined as every static hand posture with which an object can be held securely with one hand [2].

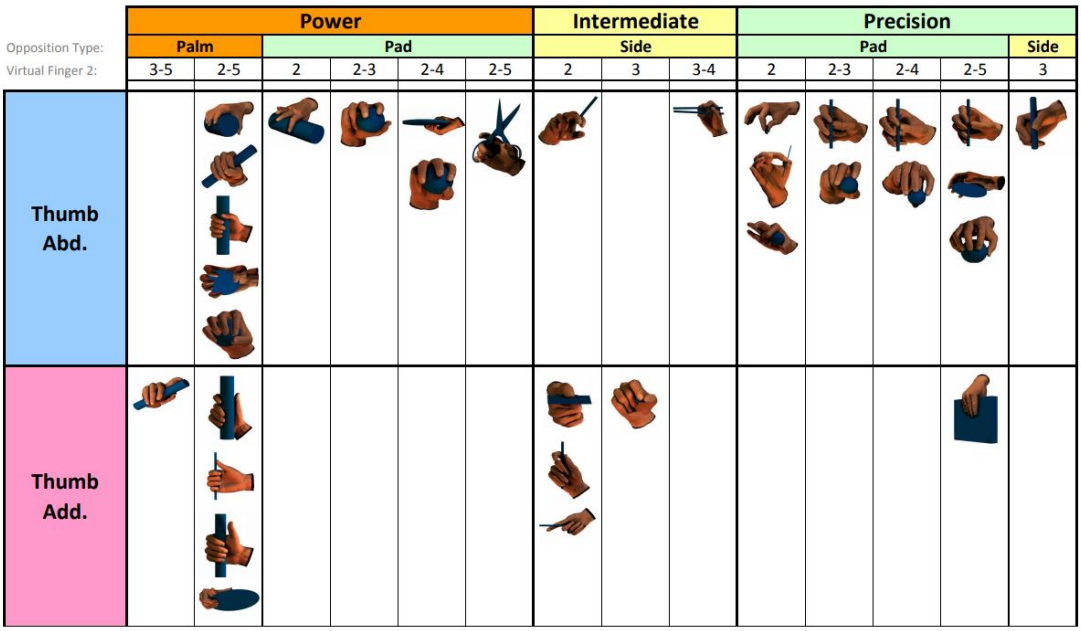

Figure 2 – Grasping taxonomy including 33 grasp types from [2]

(a) (b) (c) (d) (e)

Figure 3 – Different hand morphologies with different degrees of freedom: (a) Schunk Dexterous Hand (b) Robotiq Adaptive Gripper (c) Allegro Hand (d) Vizzy Hand [1] (e) iCub hand icub [3].

Hand posture relies significantly on the hand design, specifically, its physical hand size, the number of joints, degrees of freedom. As the tactile sensor system must provide relevant information to the hand, it also must influence such criteria, not only from a geometrical design but also from a functional one. Grasping is a static action, and it can already be overwhelming designing a tactile system. Because object manipulation aims for dynamic control of the objects, the challenge can be even higher.

The design of a tactile sensor system must consider the hand's design and purpose it will be integrated on. Even though very challenging, these will be specific requirements, mainly regarding integration, that can be solved using clever engineering strategies. However, regardless of the hand's design and tactile system performing grasping and object manipulation task it must perform specific list of requirements (Table 1). These will be the guidelines used for the tactile system in this work.

Functional requirements relate the sensor's information with the requirements we need to define grasping [4,5]. Integration requirements focus on the interface between the sensor and the robot interface, such as communication interface with the robot, and physical integration requirements, such as the geometrical constraints that do not impact the hand movement.

Table 1 - Detection requirements for grasping and manipulating object [6]

#	*Functional Requirements*
F-Rq1	Detect the contact and release of an object.
F-Rq2	Detect lift and replacement of an object.
F-Rq3	Detect shape and force distribution of a contact region for object recognition.
F-Rq4	Detect contact force magnitude and direction for maintaining a stable grasp during manipulation.
F-Rq5	Detect both dynamic and static contact forces.
F-Rq6	Track variation of contact point during manipulation.
F-Rq7	Detect force and magnitude of contact forces due to the motion of the hand during manipulation.
F-Rq8	Detect tangential forces due to the weight and shape of the object to prevent slip.
#	*Integration Requirements*
I-Rq1	Reading time
I-Rq2	Type of communication interface
I-Rq3	It fits the hand and allows unrestrained movement
I-Rq4	Is Robust
I-Rq5	Parts are replaceable

1.4 Metrics and standards

The guidelines are not sufficient for the development and further optimization of tactile sensor systems. This is because the requirement list is a checklist and provides no basis for comparing different tactile systems. In essence, using the requirement list, we can know if a tactile system is suitable but not how it compares to other systems that serve the same purpose.

Metrics are the quantification of the requirements and should provide a measurement of the performance of the tactile sensor system for a specific requirement. The ideal metric must not rely on the working principle but on how accurately a sensor can provide the required information. Depending on the application and purpose of the sensor, each metric can also have different degrees of importance. Table 2 defines the relationship between the requirements from Table 1 and the metrics.

Table 2 – Requirement-Metrics matrix for grasping and manipulating objects.

		Minimum Force detection (N)	*Maximum Force detection (N)*	*Minimum Torque detection (N.mm)*	*Maximum Torque detection (N.mm)*	*Number of cycles until rupture (ncycles)*	*Contact point precision (mm^2)*	*Normal Force Hysteresis (%)*	*Tangencial Force Hysteresis (%)*	*Type of communication interface (Dig/Analg)*	*Time Response (ms)*	*Number of assembly parts (nparts)*	*% Comercially availabile parts (%)*	*Sensor dimentions (mm^2)*
F-Rq1	Detect the contact and release	x		x										
F-Rq2	Detect lift and replacement	x		x										
F-Rq3	Detect shape and force	x		x										
F-Rq4	Stable grasp during manipulation		x				x							
F-Rq5	Dynamic and static forces.						x	x						
F-Rq6	Track variation of contact point.						x							
F-Rq7	Detect force and magnitude of contact forces due to the motion of the hand during manipulation.		x		x						x			
F-Rq8	Detect tangential forces due to the weight and shape of the object to prevent slip.	x		x										
I-Rq1	Reading time										x			
I-Rq2	Type of communication interface									x				
I-Rq3	It fits the hand and allows unrestrained movement											x		x
I-Rq4	Is Robust					x		x	x					
I-Rq5	Parts are replaceable												x	

Designing and optimizing the sensors to achieve better performance for these metrics, we should inevitably reach systems that are better suited for grasping and object manipulation. Defining the metrics is not a trivial job that requires a much thorough job than what we present. The metrics selected are based on the most common quantities reported in academic literature and their ability to quantify the requirements. The latter is a subjective observation and holds minor to no value, but it allows us to compare the different solutions in the literature as a starting point.

Ideally, a metric should define only one requirement quantitatively; thus, Table 2 shows that we still have significant room for improvement. A good metric must depend on a reliable and reproducible measurement testing procedure, which is a significant challenge for the tactile sensing community to agree upon due to the different types of hands and geometries. Reasonable efforts have been made to standardize these methodologies by the National Institute of Standards and Technology (NIST) [7], by defining metrics that depend on the hand and the sensor system.

1.5 Tactile sensors

Object manipulation is an essential skill for robots to interact with the external world, especially in environments designed for human beings. It is not a trivial task because it requires the successful coordination of body parts (i.e., head and eyes, arm, hand, fingers) and sensory channels (i.e., vision, touch, proprioception). One crucial component in object manipulation, but still not fully developed in robotic manipulation, is tactile sensing [7].

In fact, although tactile sensing has been an active research area for more than three decades [8], the effective integration of tactile sensing systems into robots is still limited [9], even for robotic hands [10,11]. One of the biggest challenges is to cover small multi-curved surfaces, such as the fingertip of a robot hand, with several sensors to measure the contact forces on multiple locations simultaneously.

A tactile sensor is a device that correlates a mechanical stimulus, usually a force or a torque, with an electrical signal. In terms of transduction methods, several solutions have been proposed, including capacitive [5], piezoresistive [6], piezoelectric [7], optical [8–10], and magnetic [11,12]. The magnetic tactile sensors usually benefit from high robustness, low or inexistent mechanical hysteresis, low cost, and are relatively easy to assemble [12,13]. A few companies have also started to produce tactile sensors for robotic applications, for example, the FlexiForce from Tekscan ,[13] the 3D Force Sensor from OptoForce [14], the QTC sensors from Peratech [15], and the BioTac fingertip from Syntouch [16]. Creativity plays a role in the method used to translate the mechanical stimuli into an electrical signal, as many geometries and configurations can be found in industry and academic literature.

Tactile sensors are a significant engineering challenge mainly due to their robustness and performance requirements, aggravated by integration complexity that fits them in geometrically limited places (e.g. fingertips). This challenge can be tackled by using miniaturized components and flexible electronics, in addition to clever design solutions that would minimize the number of components without sacrificing the quality of the measurements. Miniaturization and mechanical robustness have been drivers for the recent increase in scientific interest in soft robotics [17] and flexible electronics [12,18]. The combination of INESC-MN microfabrication facilities and ISR design and development of Vizzy brought together an exceptional opportunity that this thesis aims to capitalize on.

Vizzy's initial design integrated commercial magnetic tactile sensors and a magnet embedded in an elastomer. That decision aimed to capitalize on this approach their low cost, low hysteresis, ease to fabricate, and robustness, when compared to other existing tactile technologies[12]. Leveraging INESC-MN know-how and experience in magnetic sensors, this thesis proposes improvements for the current tactile system.

Table 3 – Overview of different working principles and their respective advantages and disadvantages.

Adapted from [7].

TRANSDUCTION MECHANISMS	ADVANTAGES	DISADVANTAGES
CAPACITIVE/MAGNETIC	High sensitivity High spatial resolution Large dynamic range Temperature independent	Stray capacitance Complex measurement circuit Cross-talk between elements Susceptible to noise Hysteresis
PIEZORESISTIVE	Simple construction High spatial resolution Low cost Compatible with VLSI	Hysteresis High power consumption Lack of reproducibility
PIEZOELECTRIC	High-frequency response High accuracy High sensitivity High dynamic range	Poor spatial resolution Charge leakages Dynamic sensing only
OPTICAL	Good reliability Wide sensing range High repeatability High spatial resolution	Non-conformable Bulky in size Susceptible to temperature or misalignment
INDUCTIVE	Linear output High sensitivity High power output High dynamic range	Low-frequency response Poor reliability More power consumption

1. Moreno, P.; Nunes, R.; Figueiredo, R.; Ferreira, R.; Bernardino, A.; Santos-Victor, J.; Beira, R.; Vargas, L.; Aragão, D.; Aragão, M. Robot 2015: Second Iberian Robotics Conference: Advances in Robotics, Volume 1. *Advances in Intelligent Systems and Computing* **2016**, *417*, 17–28, doi:10.1007/978-3-319-27146-0.

2. Feix, T.; Pawlik, R.; Schmiedmayer, H.-B.; Romero, J.; Kragi, D. A Comprehensive Grasp Taxonomy. *Robotics, Science and Systems Conference: Workshop on Understanding the Human Hand for Advancing Robotic Manipulation* **2009**, 2–3.

3. Parmiggiani, A.; Maggiali, M.; Natale, L.; Nori, F.; Schmitz, A.; Tsagarakis, N.; Victor, J.S.; Becchi, F.; Sandini, G.; Metta, G. The Design of the ICub Humanoid Robot. *International Journal of Humanoid Robotics* **2012**, *9*, 1–24, doi:10.1142/S0219843612500272.

4. Youssefian, S.; Rahbar, N.; Torres-Jara, E. Contact Behavior of Soft Spherical Tactile Sensors. *IEEE Sensors Journal* **2014**, *14*, 1435–1442, doi:10.1109/JSEN.2013.2296208.

5. Bicchi, A. Hands for Dexterous Manipulation and Robust Grasping: A Difficult Road toward Simplicity. *IEEE Transactions on Robotics and Automation* **2000**, *16*, 652–662, doi:10.1109/70.897777.

6. Yousef, H.; Boukallel, M.; Althoefer, K. Tactile Sensing for Dexterous In-Hand Manipulation in Robotics - A Review. *Sensors and Actuators, A: Physical* **2011**, *167*, 171–187, doi:10.1016/j.sna.2011.02.038.

7. Mason, M.T. Toward Robotic Manipulation. *Annual Review of Control, Robotics, and Autonomous Systems* **2018**, *1*, 1–28, doi:10.1146/annurev-control-060117-104848.

8. Li, Q.; Kroemer, O.; Su, Z.; Veiga, F.F.; Kaboli, M.; Ritter, H.J. A Review of Tactile Information: Perception and Action through Touch. *IEEE Transactions on Robotics* **2020**, *36*, 1619–1634, doi:10.1109/TRO.2020.3003230.

9. Dahiya, R.S.; Valle, M.; Metta, G. System Approach: A Paradigm for Robotic Tactile Sensing. *International Workshop on Advanced Motion Control, AMC* **2008**, *1*, 110–115, doi:10.1109/AMC.2008.4516050.

10. Dahiya, R.S.; Mittendorfer, P.; Valle, M.; Cheng, G.; Lumelsky, V.J. Directions toward Effective Utilization of Tactile Skin: A Review. *IEEE Sensors Journal* **2013**, *13*, 4121–4138, doi:10.1109/JSEN.2013.2279056.

11. Kappassov, Z.; Corrales, J.A.; Perdereau, V. Tactile Sensing in Dexterous Robot Hands - Review. *Robotics and Autonomous Systems* **2015**, *74*, 195–220, doi:10.1016/j.robot.2015.07.015.

12. Paulino, T.; Ribeiro, P.; Neto, M.; Cardoso, S.; Schmitz, A.; Santos-Victor, J.; Bernardino, A.; Jamone, L. Low-Cost 3-Axis Soft Tactile Sensors for the Human-Friendly Robot Vizzy. In Proceedings of the Proceedings - IEEE International Conference on Robotics and Automation; 2017; pp. 966–971.

13. Tekskan FlexiForce Load/Force Sensors and Systems Available online: http://www.tekscan.com/flexiforce.html.

14. Uart, W.; Voltage, D. OptoForce Analog Signal Converter. **2015**.

15. Peratech Touch Development Kit Available online: http://www.peratech.com/qtc-touch-processing-unit.html.

16. SynTouch Sensor Technology Available online: https://www.syntouchinc.com/sensor-technology/.

17. Whitesides, G.M. Soft Robotics. *Angewandte Chemie - International Edition* **2018**, *57*, 4258–4273, doi:10.1002/anie.201800907.

18. Lu, N.; Kim, D.H. Flexible and Stretchable Electronics Paving the Way for Soft Robotics. *Soft Robotics* **2014**, *1*, 53–62, doi:10.1089/soro.2013.0005.

19. Wattanasarn, S.; Noda, K.; Matsumoto, K.; Shimoyama, I. 3D Flexible Tactile Sensor Using Electromagnetic Induction Coils. *Proceedings of the IEEE International Conference on Micro Electro Mechanical Systems (MEMS)* **2012**, 488–491, doi:10.1109/MEMSYS.2012.6170230.

20. Ribeiro, P.; Alfhadel, A.; Franco, F.; Freitas, S.; Bernardino, A.; Schmitz, A.; Jamone, L. Bio-Inspired Ciliary Force Sensor for Robotic Platforms. **2016**.

21. Alfadhel, A.; Khan, M.A.; Freitas, S.C. de; Kosel, J.; Member, S. Magnetic Tactile Sensor for Braille Reading. **2016**, 1–6, doi:10.1109/JSEN.2016.2558599.

22. Hellebrekers, T.; Zhang, K.; Veloso, M.; Kroemer, O.; Majidi, C. Localization and Force-Feedback with Soft Magnetic Stickers for Precise Robot Manipulation. *IEEE International Conference on Intelligent Robots and Systems* **2020**, 8867–8874, doi:10.1109/IROS45743.2020.9341281.

23. Clark, J.J. A Magnetic Field Based Compliance Matching Sensor for High Resolution, High Compliance Tactile Sensing. *Robotics and Automation, 1988. Proceedings., 1988 IEEE International Conference on* **1988**, 772–777 vol.2, doi:10.1109/ROBOT.1988.12152.

24. Takenawa, S. A Magnetic Type Tactile Sensor Using a Two-Dimensional Array of Inductors. *Proceedings - IEEE International Conference on Robotics and Automation* **2009**, 3295–3300, doi:10.1109/ROBOT.2009.5152420.

25. Goka, M.; Nakamoto, H.; Takenawa, S. A Magnetic Type Tactile Sensor by GMR Elements and

Inductors. *IEEE/RSJ 2010 International Conference on Intelligent Robots and Systems, IROS 2010 - Conference Proceedings* **2010**, 885–890, doi:10.1109/IROS.2010.5650283.

26. Ledermann, C.; Wirges, S.; Oertel, D.; Mende, M.; Woern, H. Tactile Sensor on a Magnetic Basis Using Novel 3D Hall Sensor - First Prototypes and Results. *INES 2013 - IEEE 17th International Conference on Intelligent Engineering Systems, Proceedings* **2013**, 55–60, doi:10.1109/INES.2013.6632782.

27. Wang, H.; de Boer, G.; Kow, J.; Ghajari, M.; Alazmani, A.; Hewson, R.; Culmer, P. A Low-Cost Soft Tactile Sensing Array Using 3D Hall Sensors. *Procedia Engineering* **2016**, *168*, 650–653, doi:10.1016/j.proeng.2016.11.237.

28. Hackwood, S.; Beni, G. Shear-Sensitive Magnetoresistive Robotic Tactile Sensor. *IEEE Transactions on Magnetics* **1986**, *22*, 394–396, doi:10.1109/TMAG.1986.1064386.

29. Hackwood, S.; Beni, G.; Hornak, L. a.; Wolfe, R.; Nelson, T.J.J. A Torque-Sensitive Tactile Array for Robotics. *The International Journal of Robotics Research* **1983**, *2*, 46–50, doi:10.1177/027836498300200204.

30. Tomo, T.P.; Wong, W.K.; Schmitz, A.; Kristanto, H.; Sarazin, A.; Jamone, L.; Somlor, S.; Sugano, S. A Modular, Distributed, Soft, 3-Axis Sensor System for Robot Hands. *IEEE-RAS International Conference on Humanoid Robots* **2016**, 454–460, doi:10.1109/HUMANOIDS.2016.7803315.

31. Tomo, T.P.; Somlor, S.; Schmitz, A.; Jamone, L.; Huang, W.; Kristanto, H.; Sugano, S. Design and Characterization of a Three-Axis Hall Effect-Based Soft Skin Sensor. *Sensors (Switzerland)* **2016**, *16*, doi:10.3390/s16040491.

32. Yan, Y.; Hu, Z.; Yang, Z.; Yuan, W.; Song, C.; Pan, J.; Shen, Y. Soft Magnetic Skin for Super-Resolution Tactile Sensing with Force Self-Decoupling. *Science Robotics* **2021**, *6*, eabc8801, doi:10.1126/scirobotics.abc8801.

33. Tomo, T.P.; Schmitz, A.; Wong, W.K.; Kristanto, H.; Somlor, S.; Hwang, J.; Jamone, L.; Sugano, S. Covering a Robot Fingertip With USkin: A Soft Electronic Skin With Distributed 3-Axis Force Sensitive Elements for Robot Hands. *IEEE Robotics and Automation Letters* **2018**, *3*, 124–131, doi:10.1109/LRA.2017.2734965.

34. Tomo, T.P.; Regoli, M.; Schmitz, A.; Natale, L.; Kristanto, H.; Somlor, S.; Jamone, L.; Metta, G.; Sugano, S. A New Silicone Structure for USkin - A Soft, Distributed, Digital 3-Axis Skin Sensor and Its Integration on the Humanoid Robot ICub. *IEEE Robotics and Automation Letters* **2018**, *3*, 2584–2591, doi:10.1109/LRA.2018.2812915.

35. COEY, J.M.D. *Magnetism and Magnetic Materials*; Cambridge University Press: Dublin, 2009;

ISBN 9780521816144.

36. Model, R.; Trahms, L. An Inverse Problem of Magnetic Source Localization. *Numer Algor* **1993**, *5*, 603–610, doi:10.1007/bf02221587.

37. Wang, X.; Meng, M.Q.H.; Hu, C. A Localization Method Using 3-Axis Magnetoresistive Sensors for Tracking of Capsule Endoscope. *Annual International Conference of the IEEE Engineering in Medicine and Biology - Proceedings* **2006**, *1*, 2522–2525, doi:10.1109/IEMBS.2006.260711.

38. Sun, Z.; Foong, S.; Marechal, L.; Teo, T.H.; Tan, U.X.; Shabbir, A. Using Heterogeneous Sensory Measurements in a Compliant Magnetic Localization System for Medical Intervention. *IEEE/ASME International Conference on Advanced Intelligent Mechatronics, AIM* **2015**, *2015-Augus*, 133–138, doi:10.1109/AIM.2015.7222521.

39. Marechal, L.; Foong, S.; Sun, Z.; Wood, K.L. Design Optimization of the Sensor Spatial Arrangement in a Direct Magnetic Field-Based Localization System for Medical Applications. *Proceedings of the Annual International Conference of the IEEE Engineering in Medicine and Biology Society, EMBS* **2015**, *2015-Novem*, 897–900, doi:10.1109/EMBC.2015.7318507.

40. Ribeiro, P.; Neto, M.; Cardoso, S. Strategy for Determining a Magnet Position in a 2-D Space Using 1-D Sensors. *IEEE Transactions on Magnetics* **2018**, *54*, doi:10.1109/TMAG.2018.2851928.

41. Wu, F.Y.; Foong, S.; Sun, Z. A Hybrid Field Model for Enhanced Magnetic Localization and Position Control. *IEEE/ASME Transactions on Mechatronics* **2015**, *20*, 1278–1287, doi:10.1109/TMECH.2014.2341644.

42. Wu, F.; Robert, N.M.; Frey, D.D.; Foong, S. Enhanced Magnetic Localization with Artificial Neural Network Field Models. *Robotics and Automation (ICRA), 2013 IEEE International Conference on* **2013**, 1560–1565, doi:10.1109/ICRA.2013.6630778.

43. Derby, N.; Olbert, S. Cylindrical Magnets and Ideal Solenoids. *American Journal of Physics* **2010**, *78*, 229–235, doi:10.1119/1.3256157.

44. Silva, A. v.; Leitao, D.C.; Valadeiro, J.; Amaral, J.; Freitas, P.P.; Cardoso, S. Linearization Strategies for High Sensitivity Magnetoresistive Sensors. *The European Physical Journal Applied Physics* **2015**, *72*, 10601, doi:10.1051/epjap/2015150214.

45. Parkin, S.S.P. Flexible Giant Magnetoresistance Sensors. *Applied Physics Letters* **1996**, *69*, 3092–3094, doi:10.1063/1.117315.

46. Gaspar, J.; Fonseca, H.; Paz, E.; Costa, M.; Martins, M.; Ferreira, R.; Cardoso, S.; Freitas, P.P. Fabrication and Mechanical Characterization of Flexible Devices with Sensors with

Magnetoresistance Responses above 150 %. 10–12.

47. Valadeiro, J.; Amaral, J.; Leitao, D.C.; Silva, A. v.; Gaspar, J.; Silva, M.; Costa, M.; Martins, M.; Franco, F.; Fonseca, H.; et al. Bending Effect on Magnetoresistive Silicon Probes. *IEEE Transactions on Magnetics* **2015**, *51*, 3–6, doi:10.1109/TMAG.2015.2441956.

48. Makarov, D.; Melzer, M.; Karnaushenko, D.; Schmidt, O.G.; Makarov, D.; Melzer, M.; Karnaushenko, D.; Schmidt, O.G. Shapeable Magnetoelectronics. *Applied Physics Review* **2016**, *3*, 011101, doi:10.1063/1.4938497.

49. Uhrmann, T.; Bär, L.; Dimopoulos, T.; Wiese, N.; Rührig, M.; Lechner, a. Magnetostrictive GMR Sensor on Flexible Polyimide Substrates. *Journal of Magnetism and Magnetic Materials* **2006**, *307*, 209–211, doi:10.1016/j.jmmm.2006.03.070.

50. Karnaushenko, D.; Makarov, D.; St??ber, M.; Karnaushenko, D.D.; Baunack, S.; Schmidt, O.G. High-Performance Magnetic Sensorics for Printable and Flexible Electronics. *Advanced Materials* **2015**, *27*, 880–885, doi:10.1002/adma.201403907.

51. Singh, M.; Haverinen, H.M.; Dhagat, P.; Jabbour, G.E. Inkjet Printing-Process and Its Applications. *Advanced Materials* **2010**, *22*, 673–685, doi:10.1002/adma.200901141.

52. Singh, W.S.; Rao, B.P.C.; Thirunavukkarasu, S.; Jayakumar, T. Flexible GMR Sensor Array for Magnetic Flux Leakage Testing of Steel Track Ropes. *Journal of Sensors* **2012**, *2012*, doi:10.1155/2012/129074.

53. Gaspar, J.; Fonseca, H.; Paz, E.; Martins, M.; Valadeiro, J.; Cardoso, S.; Ferreira, R.; Freitas, P.P. Flexible Magnetoresistive Sensors Designed for Conformal Integration. *IEEE Transactions on Magnetics* **2017**, *53*, 5–8, doi:10.1109/TMAG.2016.2623669.

54. Melzer, M.; Makarov, D.; Calvimontes, A.; Karnaushenko, D.; Baunack, S.; Kaltofen, R.; Mei, Y.; Schmidt, O.G. Stretchable Magnetoelectronics. *Nano Letters* **2011**, *11*, 2522–2526, doi:10.1021/nl201108b.

55. Melzer, M.; Lin, G.; Makarov, D.; Schmidt, O.G. Stretchable Spin Valves on Elastomer Membranes by Predetermined Periodic Fracture and Random Wrinkling. *Advanced Materials* **2012**, *24*, 6468–6472, doi:10.1002/adma.201201898.

56. Mimoun, B.; Pham, H.T.M.; Henneken, V.; Dekker, R. Residue-Free Plasma Etching of Polyimide Coatings for Small Pitch Vias with Improved Step Coverage. *Journal of Vacuum Science & Technology B: Microelectronics and Nanometer Structures* **2013**, *31*, 021201, doi:10.1116/1.4788795.

57. Dick, A.R.; Bell, W.K.; Luke, B.; Maines, E.; Mueller, B.; Rawlings, B.; Kohl, P.A.; Grant Willson, C. High Aspect Ratio Patterning of Photosensitive Polyimide with Low Thermal

Expansion Coefficient and Low Dielectric Constant. *Journal of Micro/Nanolithography, MEMS, and MOEMS* **2016**, *15*, 033503, doi:10.1117/1.JMM.15.3.033503.

58. Gehanno, V.; Freitas, P.P.; Veloso, A.; Ferreira, J.; Almeida, B.; Sousa, J.B.; Kling, A.; Soares, J.C.; da Silva, M.F. Ion Beam Deposition of Mn-Ir Spin Valves. *IEEE Transactions on Magnetics* **1999**, *35*, 4361–4367, doi:10.1109/20.799086.

59. Alfadhel, A.; Khan, M.A.; Cardoso, S.; Leitao, D.; Kosel, J. A Magnetoresistive Tactile Sensor for Harsh Environment Applications. *Sensors (Switzerland)* **2016**, *16*, doi:10.3390/s16050650.

60. Fu, Y.B.; Ogden, R.W. *Nonlinear Elasticity: Theory and Applications*; Cambridge University Press: Cambrigde, 2001; ISBN 9780511526466.

Chapter 2

Designing a Magnetic Tactile Sensor

2.1 Magnetic Tactile Sensors

Magnetic tactile sensors correlate a change in the magnetic field to an applied force. First can be categorized by the magnetic field source: permanent magnets and electromagnetic coils. Furthermore, we can divide permanent magnets into bulk or magnetized nanoparticle clusters (see Figure 4).

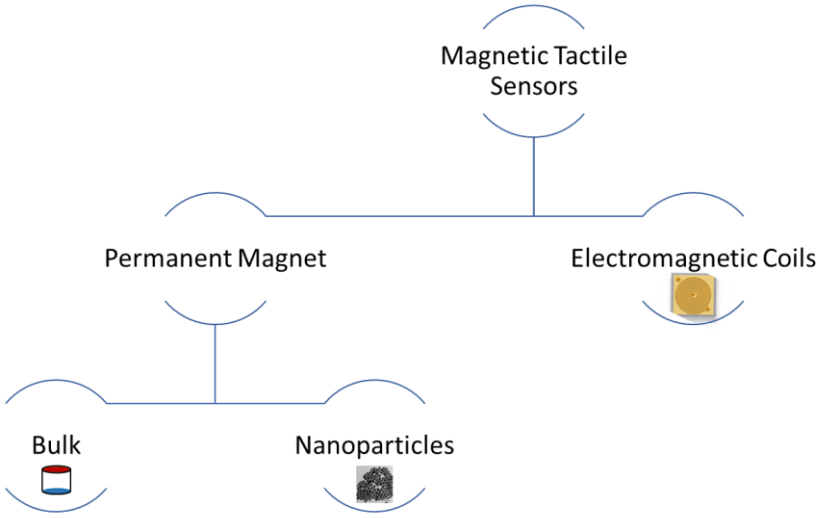

Figure 4 – Types of magnetic tactile sensors, categorized by the source of magnetic field and type of magnet.

The most common working principle relies on a permanent magnet, a magnetic sensor, and an elastomeric medium that embedded the magnet(s). Changing the distance between the magnet and the sensor results in a change in the sensor output, inevitably correlated to the elastomeric part's deformation and, consequently, the applied force. The electromagnetic coils take advantage of Faraday's law of induction, where applying a current to the coil results in the generation of a magnetic field.

The magnetic field generation by a coil requires an additional current source, inevitably increasing power consumption and the size of the electronic interface required, both relevant to integrating the sensor in the robot hand. However, if programmed to emit the magnetic field at a specific frequency, this could be a good solution for removing external magnetic forces from the measurement or having several coils know the coil that is the magnetic field source. Moreover, using coils for magnetic sources instead of permanent magnets could be an elegant solution since the signal can have a distinct frequency [8]. This is potentially beneficial for two reasons, first, to distinguish from other environmental factors, and second, because each magnet source is identifiable. However, the current required to generate significant magnetic fields, coil dimensions, density, and heat dissipation can be unsurmountable for practical applications of these designs.

The main drawbacks are the required current to operate the coils, while the permanent magnets do not allow frequency identification. An intermediate solution could hold good promise by using a

permanent magnet as a magnetic flux guide and amplifying an AC field generated by a coil, but integrating such a system would be a significant engineering challenge.

Coils could be promising solutions, especially for dynamic slip detection. However, we will discard them as a solution mainly to the increase in power consumption and integration complexity. There are two main types in the permanent magnet's category: a bulk NdFeB magnet embedded on an elastomer or magnetized nanoparticles incorporated distributed in an elastomer.

2.1.1 Magnetized nanoparticles

Magnetic nanoparticles can offer new geometries and different permanent shapes, providing new tactile responses. They can provide magnets with more complex physical geometries that create more interesting magnetic fields. With magnetized nanoparticles, the idea of a deformable magnet is a possibility. A magnetic cilia approach has shown high potential for high precision tactile sensing for small normal and tangential forces. It has shown potential for detecting surface roughness [9] and Braille reading [10]. However, as high precision sensors, their force range is also minimal for 300 µN to 30 mN, while the recommended range for object manipulation being 0.01N to 10N [6]

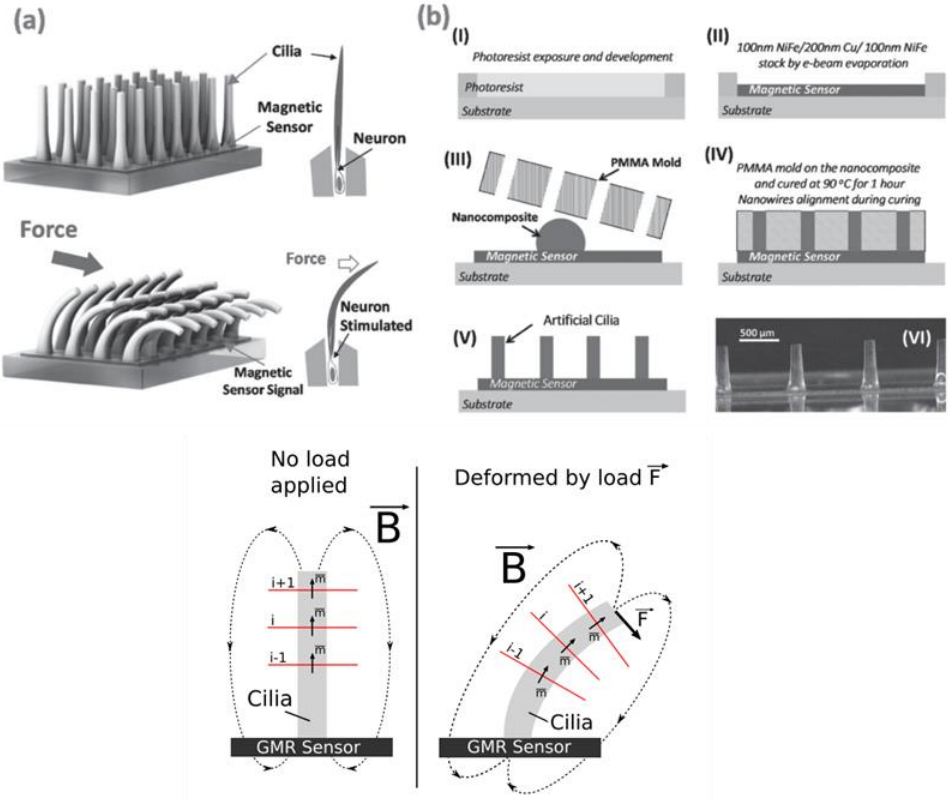

Figure 5 – a) Illustration of the nanocomposite cilia tactile sensor. The sensor is made of permanent magnetic nanocomposite cilia integrated on a magnetic sensor that mimics the neuron in natural cilia. When the cilia get deflected by external forces such as fluid flow or hand touch, the stray field at the magnetic sensor changes, which also changes its impedance. b) The fabrication process of the tactile sensor. c) Schematics of the pillar deformation model used to determine its magnetization. On the left, the pillar is non-deformed, and, all dipoles point in the direction of the pillar long axis. On the right, the pillar suffered deformation and the dipoles rotated, changing the incident field over the sensor.

Another use of magnetic nanoparticles is to use all the part is magnetic and deformable, we can also have access to information such as contact point can be estimated. However, the minimum force it can detect is 20N, mainly due to each local particle's low magnetic contribution to the signal.

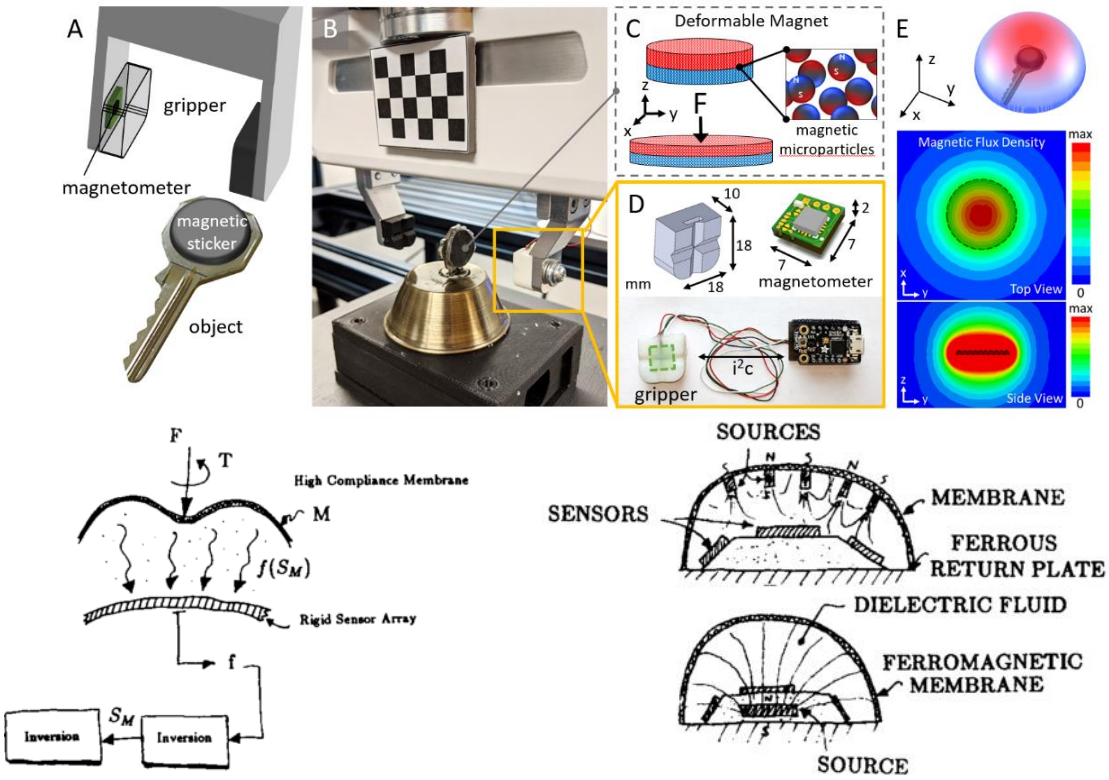

Figure 6 - A) Overview and B) image of modified Franka Gripper localizing to a soft magnetic sticker on a key. C) By embedding magnetic microparticles in an elastomer, we can create a soft and deformable magnetic sticker. D) Combined with a 3-axis magnetometer inside the gripper, E) the magnetic flux surrounding the sticker can be used for 3D localization, contact detection, and force estimation. Adapted from [11]. F) Compliance matching the tactile sensor. G) An active magnetic field-based compliance matcher. H) A passive magnetic field-based compliance matcher. [12]

2.1.2 Bulk Permanent Magnet

The most straightforward solution is to have a magnetic sensor and a bulk permanent magnet embedded in an elastomer in **Figure 7**. In this approach, the magnet's relative position to the sensor provides information regarding the stimuli applied.

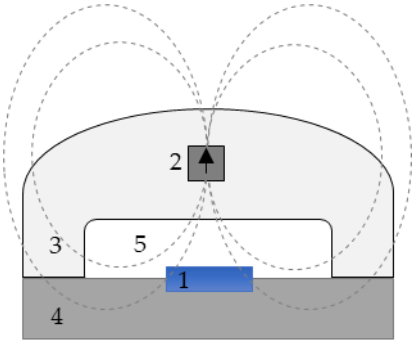

Figure 7. Schematic view of the devices' working principle concept currently integrated in Vizzy hand [13]; The numbers in the Figure stand for: 1 – Sensors (blue); 2 – Cylindrical Nd Permanent Magnet; 3 – Polymeric silicone part; 4 – Robotic finger; 5 – Air gap; (- - -) Magnetic field lines for the permanent magnet. **(c)** 3D view of the FPC with the Si Chips embedded in the Elastomer part.

This approach's simplicity enables an easy integration on the finger because it only requires an elastomer, a magnet, and a sensor. Its simplicity, ease of fabrication, and robustness are attractive features to the robotics community, and the number of academic papers and similar solutions that use this principle is a testament to it.

Its simplicity comes with a cost, where measurement errors undermine its ability to provide critical and reliable information regarding an applied stimulus. In the literature, two main issues are discussed: magnet tilting and external magnetic fields. We can find three main strategies that minimize these issues.1) Increasing the number of sensors; 2) Repeat the magnet-sensor pair in space as a unit cell.

One permanent magnet and one sensor provide a relative amount of information, so other incremental strategies to improve the information are common, such as increasing the number of sensors [22] and using neural networks and magnetoresistive sensors to reduce magnet tilting error, or adding more magnets. Increasing the number of sensors allows us to gather more information about the same magnet. The idea behind it is to improve the ability to measure the position and tilting of the magnet. The increase in the number of sensors can be done in two ways: we can measure more field dimensions at the same point or create an array of sensors measuring the field in an area.

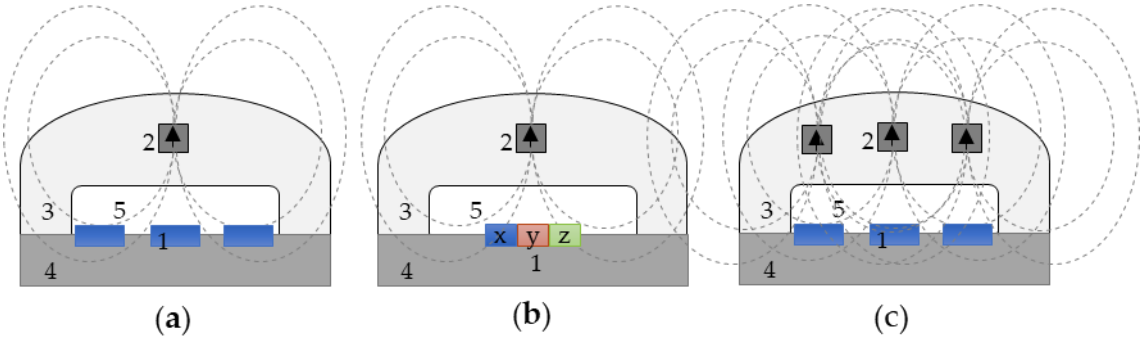

Figure 8. Schematic view of the alternative solutions: a) array of sensors; b) higher number of sensors in the same place in different orientations; c) repeating the sensor-magnet unit cell. The numbers in the Figure stand for: 1 – Sensors (blue); 2 – Cylindrical Nd Permanent Magnet; 3 – Polymeric silicone part; 4 – Robotic finger; 5 – Air gap; (- - -) Magnetic field lines for the permanent magnet. **(c)** 3D view of the FPC with the Si Chips embedded in the Elastomer part.

Approaches a) and b) aim to reduce the measurement errors, while c) focus on achieving a reasonable control of the contact point variation. Examples of the a) show that it can be implemented with a detection range of 0.1 to 1N for normal Fz and shear forces Fx and Fy [4]. However, the increased footprint area and the inability of determination were still significant issues, whether the technology is induction [14] or GMR sensors [15].

The commercialization of the 3D hall sensor technology enabled the concept b), which has been prolific recently [13,16,17], but no improvements to the original issues are reported.

Strategy c) has been done using 1D [18,19] to recreate the sensor surface by understanding where each magnet is in the space. A system with an array of sensors is fixed on a rigid surface while a "high compliance magnetic membrane" adapts to the mechanical stimuli [11]. High mathematical complexity and limitation for the surface's recalculation due to respective magnetic field sources' influence cannot be distinguished individually, making it very challenging to take advantage of this concept [21]. At the time, the sensors available were sensitive to one direction, and no neural networks or significant computational power was commonly available. Towards this goal, the 3D hall sensors [20,21] do not provide surface information.

Recently, a strategy designed the orientation of the permanent magnet by designing a sinusoidally magnetized flexible film [32]. This provided an idea of the surface but relied on complex algorithms based on artificial neural networks without providing any contact resolution quantity.

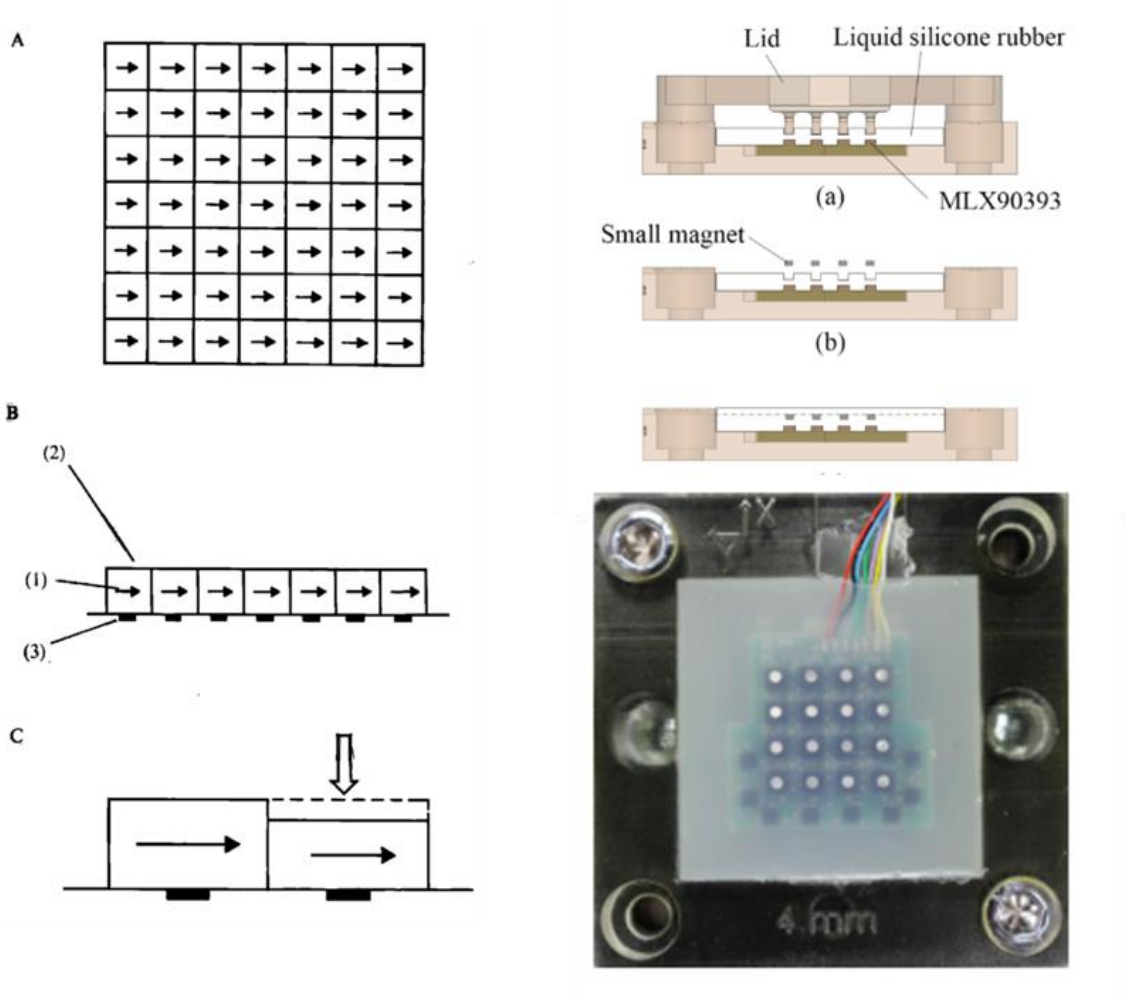

Figure 9 – (left) A) Tactile sensor array. A. Top view of a 7x7 array. Each element is 2x2 mm. B) Cross-section to show dipole (1), embedded in a compliant medium (2), in contact with the substrate, which contains a magnetoresistive element (3) on its surface. C) Schematic operation of the device for normal forces.[24] – (right) Tactile sensor array composed by16 MLX90393 chips and 16 permanent magnets. (right) Schematics of the manufacturing process and design of the tactile senor (a) Liquid silicone rubber is poured into the mould (b) 16 permanent magnets are placed in the hole (c) an encapsulation layer of silicone is used to finish the device.

Using the sensor-magnet cell strategy can be conformed a finger surface and geometry using flexible PCBs [23,24]. This device covered a fingertip with 24 sensors 3-Axis magnetometers with 6mm and 10 mm distance in between, and each sensor is a 3x3mm sensor (see Figure 5). In this case, they were able to identify different signal patterns depending on the object's shape and size. They position one magnet on top of each sensor and report minimal interference between magnets, most likely due to the distances between each cell. Since the purpose was not to reconstruct the surface and only focus on applied forces on the magnet. Nevertheless, one key parameter identified for detecting smaller shape objects was the density of the sensors.

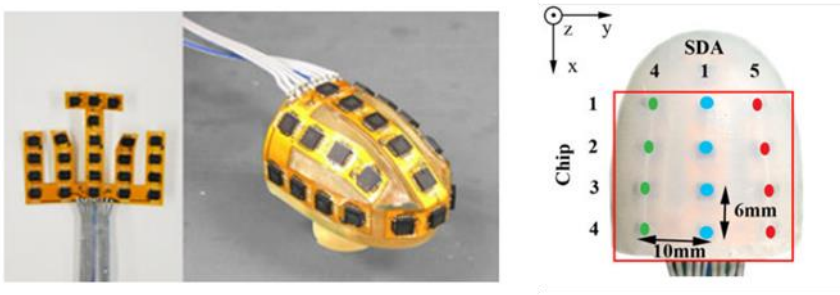

Figure 10 – a) A flex PCB with the 24 Hall sensors flat. b) The flex PCB conformed to the finger c) magnet displacement and distribution on the finger surface.[23]

Overall, these approaches support evidence that a magnet embedded on an elastomer can be used as a tactile sensor. In other words, that a force can be correlated to an electric signal using at least one magnetic sensor and a magnet embedded in an elastomer. There are enough examples to confidently state that it is possible to detect a force using a magnetic sensor and a permanent magnet embedded on an elastomer.

To further discuss these devices, we have to describe the sensor-magnet system to the best abilities. First, we must agree that this working principle bases its merits on assuming that the permanent magnet displacement is correlated with the applied force. So we use a magnetic sensor to detect the change in the magnetic field caused by the displacement of a magnet and expect to infer an applied force from it. In addition to the applied force magnitude, the permanent magnet displacement is also a function of the applied force direction, contact point, and the elastomeric part mechanical properties and geometry. Thus, the relationship between the change in the magnetic field and the applied force relationship we want to describe is not very straightforward. Machine learning algorithms can be very efficient tools to optimize for parameter fine-tuning for specific geometries but can be significantly less optimal for developing new magnetic tactile devices.

We propose a more fundamental approach to this problem, first to describe it as the relationship between three vectors: the change in the magnetic field ($\Delta\vec{H}$), the applied force ($\vec{F}$) and the permanent magnet displacement ($\vec{d}$). We define the act of designing a magnetic tactile sensor based on this principle is to be the tailoring of the relationship between these three vectors to most accurately and

easier providing the information required for grasping. So before committing to any design decision, describing and understanding these relationships is essential. In practice, this means that these relationships still hold regardless of the number of sensors, the elastomeric part's geometry, the permanent magnet's size and shape, or any other design-specific metrics one could further optimize.

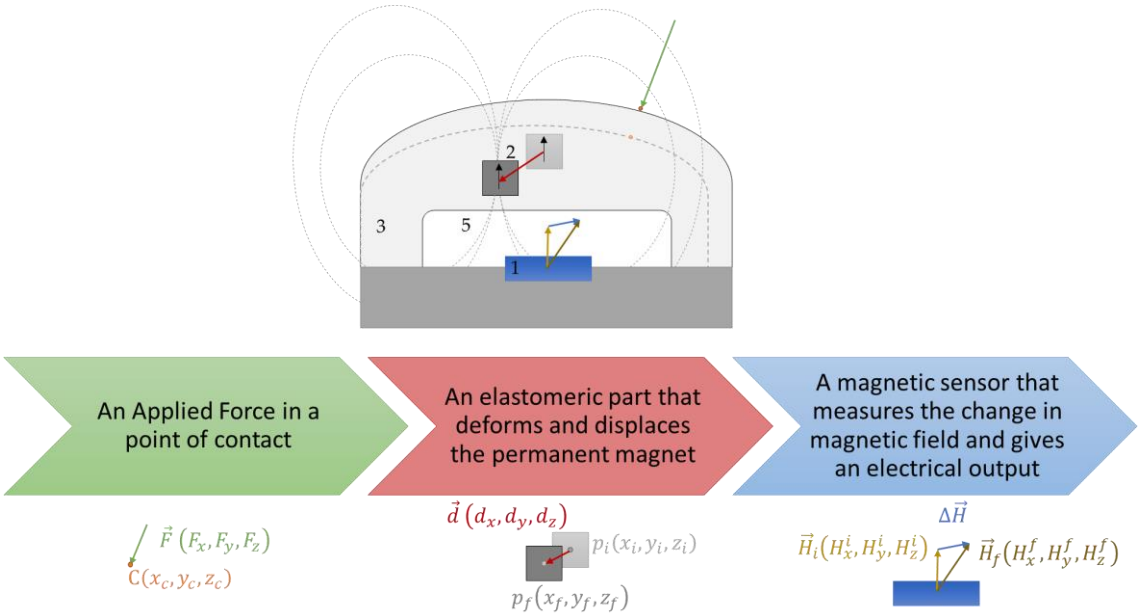

Figure 11 – Sensor-magnet system working principle description.

Using the vectorial representation in Figure 11 the relationship between the change in magnetic field ($\Delta\vec{H}$), the applied force ($\vec{F}$) and the permanent magnet displacement ($\vec{d}$) should be clearer. The chosen design parameters used will affect the relationship between the three vectors. The relationship we care about the most is the force and sensor electrical output, which we want to know and measure, respectively. To interpret the electrical output, we have to understand the magnetic sensor technology, which is not in the scope of this chapter, but it is discussed in detail in section 3.2. First, we must have an insight on whether the relationship between the permanent magnet displacement ($\vec{d}$) and the change in the magnetic field ($\Delta\vec{H}$) can be determined. Then, it should be clear which design parameters can take advantage of this relationship, and we have better chances to design more valuable sensors.

Because the displacement is just the difference between an initial point and a final point, the position of the magnet can infer it. So, the first goal is to assess our ability and limitations in determining the magnet in three-dimensional space.

2.2 Theoretical background

The four Maxwell Equations describe the relationship between the electric and magnetic fields and the behaviors of said fields[1].

(1) $\nabla . E = \frac{\rho}{\varepsilon_0}$

(2) $\nabla . B = 0$

(3) $\nabla \times E = -\frac{\partial B}{\partial t}$

(4) $\nabla \times B = \mu_0 \left(J + \varepsilon_0 \frac{\partial E}{\partial t} \right)$

A magnetostatic problem is defined by the magnetic field changing with time (i.e. static), thus we postulate that $\partial B/\partial t = 0$. As previously discussed, the only magnetic field sources are moving charges, electric currents, and ferromagnetic materials. Thus, to satisfy the $\partial B/\partial t = 0$ condition, there can be no addition of ferromagnets, no moving charges and thus $\partial E/\partial t = 0$ must be also zero.

The sensor-magnet approach, previously described, is a magnetostatic problem. In practice, an electrical circuit to measure the sensors but the fields induced by it are negligible when considering the magnitude of the fields produced by the permanent magnet are several orders of magnitude larger. The sensors also have ferromagnetic materials, and they change their position, but the magnetic moment and the frequency are negligible. So, the sensor-magnet system is magnetostatic, which simplifies the theory since only two of the four Maxwell equations are relevant: (2) and (4).

2.2.1 The Colombian approach for modeling scalar potential and magnetic field of a permanent magnet

For determining the magnetic field generated by the permanent magnetic we used the Coulombian approach because it is most accessible from a computational point of view. The density j in equation (4), in magnetostatic problems, can have two sources: from currents (j_c) and from permanent magnets (j_m). The concept of jm can be related to the magnetization using Ampere Law [25] in this way:

(5) $j_m = \nabla \times M = \nabla \times \left(\frac{B}{\mu_0} - M \right)$

The quantity in parentheses is H-field and because $\nabla . \mathrm{B} = 0$ (2) we can see that

(6) $\nabla . \mathrm{H} = -\nabla . M$

In the coulombian approach, an analogy between the electric charge and a fictitious magnetic

[1] The word field is used just to describe an action in space where there is no contact.

charge is assumed, and the field resulting from a single charge is

(7) $\mathrm{H} = q_m r/4\pi r^3$

To model a permanent magnet, we can consider the equivalent distributions of a magnetic charge in bulk and at the surface of the magnetized material:

(8) $\rho_m = -\nabla . M$ and $\sigma_m = M . e_n$

So, for the entire volume of the magnetic material

(9) $\partial H = \rho_m r/4\pi r^3 \, \partial V$

(10) $H = -\varphi_m$

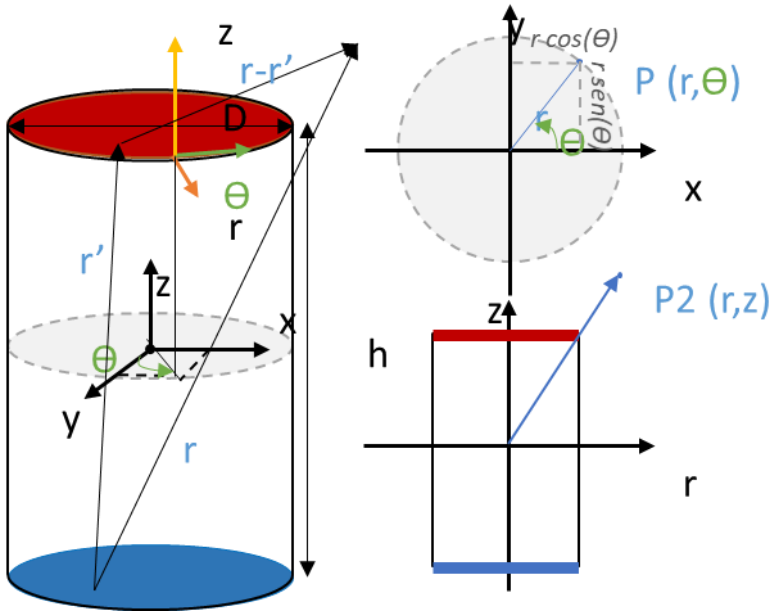

Figure 12 – Schematics of the coulombian approach used. The red and blue areas represent the two poles of the magnet.

Each area corresponds to a magnetic pole since we define the magnetization orientation (e_n) as (0 0 1) for red corresponds to the positive pole and (0 0 -1) for blue to the negative pole. Using the Bio-Savart law, we have equation (9) be:

(11) $H(r) = \frac{1}{4\pi}\left(\int_S \frac{(M.(0\ 0\ 1)(r-r')}{|r-r'|^3} d^2r' + \int_S \frac{(M.(0\ 0\ -1)(r-r')}{|r-r'|^3} d^2r'\right)$

From equation (11) we can calculate the $H(H_x, H_y, H_z)$ vector in any point in space a sensor should read when the distance between the sensor and the permanent magnet is $r(x, y, z)$.

2.3 The sensor-magnet system

A tactile sensor based on the sensor-magnet system would infer the applied force based on the accurate estimation of magnet displacement in space. The change in the magnet position over a certain period is the magnet displacement. Thus to have the magnet position $r(x, y, z)$ as a function of the sensed magnetic field $H(H_x, H_y, H_z)$ it would be beneficial to invert equation (11).

The main challenge with inverting equation (11) is the complexity of the mathematical operations [26]. In the academic literature, several approaches can provide reasonable estimations of the magnet position, based on algorithms from experimental data [27–29], artificial intelligence [30] as well as hybrid models [31,32], that use both. These approaches can estimate the location of a small magnet (under 1 cm^3 magnetic volume) with errors below 6% at distances between 5 mm to 10 cm. The main drawback of such models is that they are system-specific, specifically on the sensor and permanent magnet characteristics. While these models are an excellent tool for optimizing and characterizing said systems, they provide little to no insight into the performance of different or new systems.

We strive to find analytical solutions to describe the system because they can provide a more generalized approach and better insight into the development of new systems. Due to the already mentioned complexity, we overcame this by a) using equation (11) simplified and specific for the cylindrical magnets [33] and b) a visual approach giving insights on the relationship between the magnetic field and the position.

By calculating the magnetic field for all the points inside a volume and only showing the values that match the sensor readings, we can obtain a visual representation of the possible positions of the permanent magnet in space. We achieve this by simulation using a system represented in Figure 13 that shows a cube, the volume where we calculate the magnetic field for each point, a cylinder, the permanent magnet, and a parallelepiped representing the sensor.

The permanent magnet and the cube are centered in the origin of three-dimensional cartesian space (x, y, z), while the sensor can be in any position that matches the magnetic field. As opposed to the sensor-magnet system discussed in section 2.1.2, the permanent magnet and we try to find the sensor position instead. The vector connecting the sensor and the magnet only defines their relative position to each other, meaning all figures results can show the magnet position in $(0,0,0)$ and the sensor in $p(x_p, y_p, z_p)$ or vice-versa. For practical reasons, we placed the cylindrical permanent magnet on the center of the volume and retrieved the position of the sensor according to its readings.

For this example, we used a cube of 30 mm side and a spatial resolution of 0.05 mm, resulting in 216 million points. Next, we use the analytical model and calculate the magnetic field for each position, the system is in polar coordinates, and we convert it to cartesian. We defined the magnet according to the one Vizzy already had [13] on the finger, an N32 (B_r = 1.35T) of a radius of 0.5 mm and a height

of 1 mm.

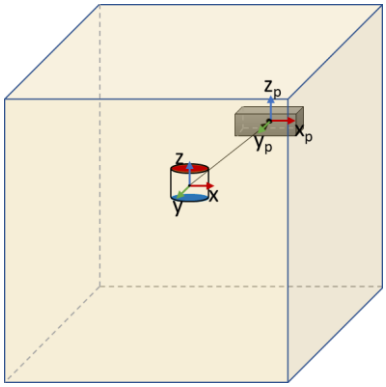

Figure 13 – A cylindrical permanent magnet and a cube, both centred in the origin of our three-dimensional space.

As an example, let us assume that in the sensor position, $p(x_p, y_p, z_p)$, the existing magnetic field is $(-0.743, 0.743, 1.849)mT$. Knowing the permanent magnet characteristics, we want to know the sensor relative position to the permanent magnet.

Several parameters affect our ability to determine the sensor position in space accurately. Any measurement error of the magnetic field affects the position prediction, meaning detectivity can be a critical factor for high position accuracy. Ultimately, the new designs for this working principle will depend on the positional accuracy of the system, but not necessarily just on detectivity.

The first variable is the number of sensitive directions. In general, we expect that more sensitive directions are helpful for higher position accuracy, which is also why three-dimensional hall sensor technology was identified as an opportunity to improve these sensor-magnet systems. The second variable is magnet tilting, defined as the angle between the sensor and the permanent magnet. Even though we know it can significantly impact position accuracy because the analytical equations are mathematically complex, there is not much quantification.

2.3.1 A sensor-magnet system with a 1D, 2D, and 3D sensors

For a one-dimensional sensor, we can only use one of the magnetic field components $H(H_x, H_y, H_z)$. A one-dimensional sensor sensitive in the x-direction would only measure for the H_x component. Figure 14 shows all the positions where a one-dimensional sensor that measures a $H_x = -0.743mT$ could be, thus the sum of all the points represents the spatial positional uncertainty for a one-dimensional sensor sensitive in the x-direction.

Due to the radial symmetry of the cylindrical permanent magnet, the sensors sensitive in x and y-directions show the same profile but rotated 90 degrees (Figure 15 a and b), while z-direction has a different geometry for its spatial positional uncertainty (Figure 15 c). The similarity between the sensors sensitive in x and y-directions is just a consequence of $|H_x| = |H_y| = 0.743mT$. A different magnitude value and the equation for spatial positional uncertainty would still be 90 degrees rotated but

not the same.

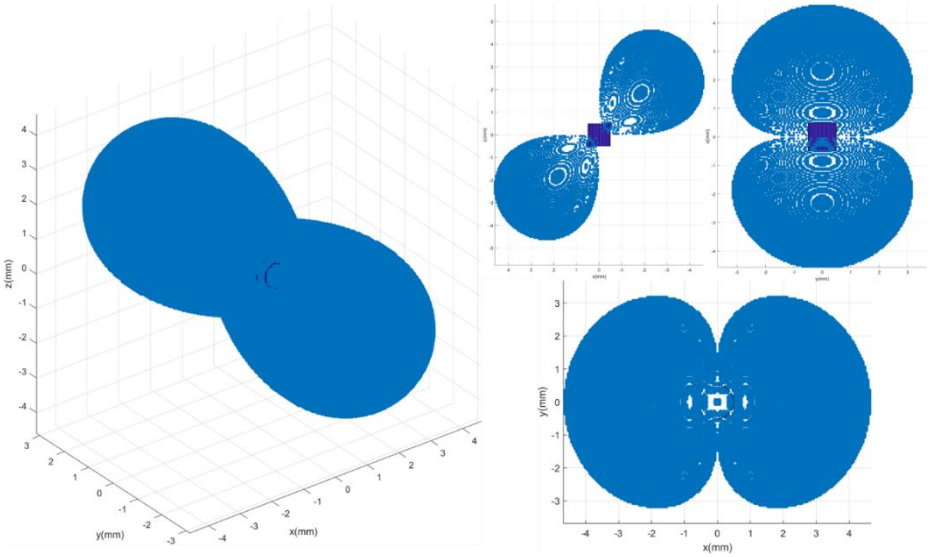

Figure 14 – Plots for the points in space where $H_x = -0.743mT$ using a cylindrical permanent magnet as a source and centred in the origin.

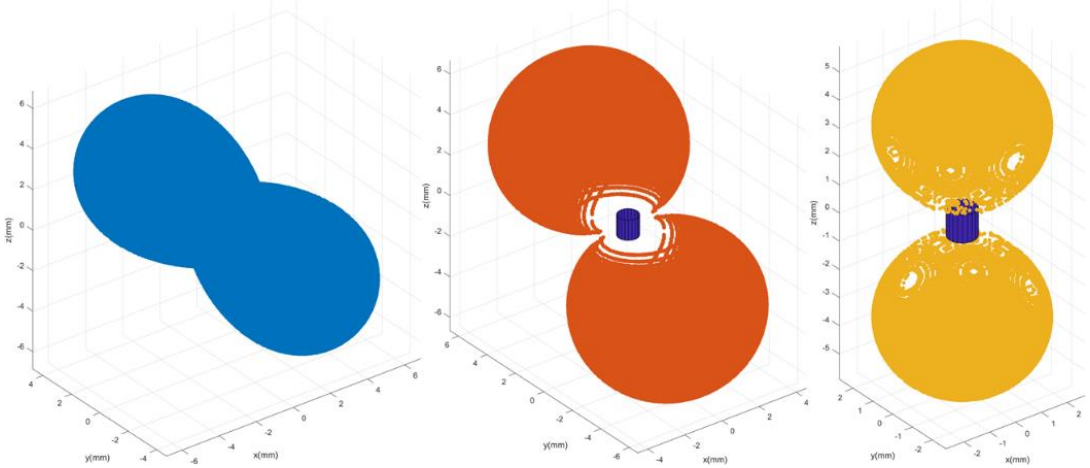

Figure 15 – Plots for the points in space where a) $H_x = -0.743mT$; b) $H_y = 0.743mT$; c) $H_z = 1.849mT$; using a cylindrical permanent magnet as a source and centred in the origin.

For a two-dimensional sensor, the position must comply with $H_x = -0.743mT$ and $H_y = 0.743mT$, meaning the resulting solution is the intersection of both blue and orange spatial positional uncertainty (see Figure 16 a and b). A two-dimensional sensor significantly decreases the number of position possibilities, transforming a spatial positional uncertainty into a curved line in space (Figure 17 c) instead of the elliptical surfaces for the one-dimensional sensors.

Visually it can be helpful to imagine the spatial positional uncertainty as *balloons*, where a weaker magnetic field detected in one direction causes the *balloon* to inflate, while an increase in magnetic field detected causes it to deflate. Applying such intuition would lead us to believe that 1) the spatial positional uncertainty increases with distance; 2) there will always be an overlap between the spatial positional uncertainty for each dimension no matter how large or small the *balloons* are.

.

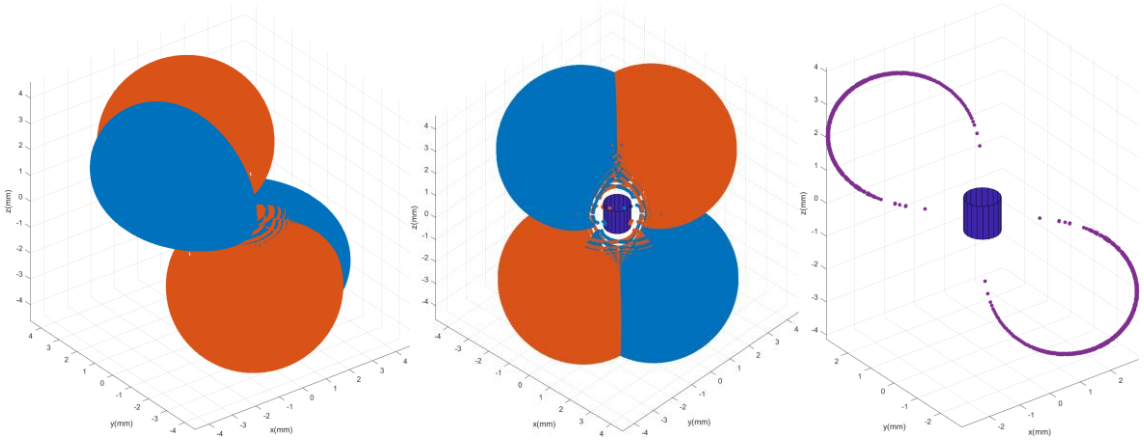

Figure 16 – Plots for the points in space where a) $H_x = -0.743mT$ (blue) and $H_y = 0.743mT$ (orange) and c) intersection (purple), where $H_x = -0.743mT$ (blue) and $H_y = 0.743mT$ (orange) simultaneously; using a cylindrical permanent magnet as a source and centered in origin.

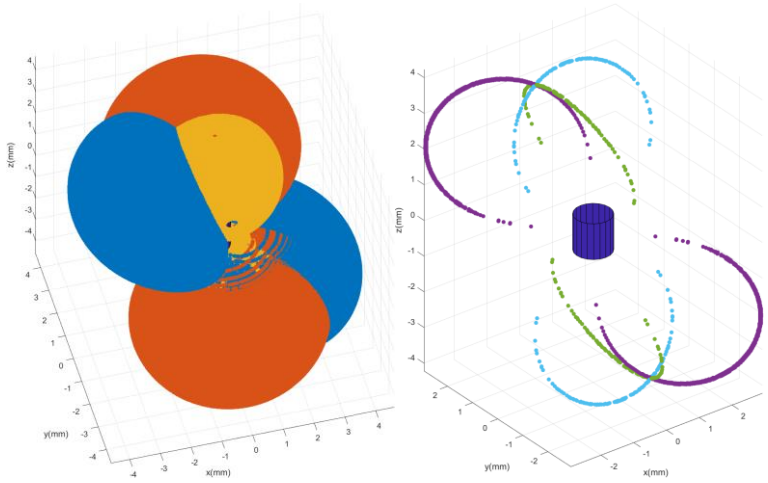

Figure 17 – Plots for the points in space where a) $H_x = -0.743mT$ (blue) and $H_y = 0.743mT$ (orange) and $H_z = 1.849mT$ (yellow) b) intersections of $H_x \wedge H_y$(purple) $H_x \wedge H_z$(green) $H_y \wedge H_z$ (light blue) simultaneously; using a cylindrical permanent magnet as a source and centred in the origin.

Using a three-dimensional sensor reduces our spatial positional uncertainty to two points represented by the intersection of the three spatial positional uncertainty in Figure 17 a). We can represent the intersection of each spatial positional uncertainty for each two-dimensional sensor intersection of $H_x \wedge H_y$(purple) $H_x \wedge H_z$(green) $H_y \wedge H_z$ (light blue) in Figure 17 b).

This way, we can easily identify the position of the sensor to be either $(1, -1, -4)mm$ or $(-1,1,4)mm$, but also intuitively understand how these functions can change in space and solve this problem. If the lines do not intersect, the sensor cannot measure said magnetic field at that point unless the angle between the sensor and the magnet has changed.

2.3.1.1 Magnetic tilting visualization

Considering the angular relationship between the sensor xyz-referential and the permanent magnet the xyz-referential is essential to validate the previous intuition further. The angle between referential is essential for position determinations because it allows the sensor to measure different magnetic field vectors by changing the angles while maintaining the coordinates. This occurrence is mentioned in the literature as magnet or sensor tilting and is usually identified as a source of error but not estimated.

Figure 15 shows a schematic relationship between the sensor and magnet referential. Based on the previously described calculation method, we define three angles, α, β, γ, each corresponding to a rotation over a specific axis, x, y, and z, respectively. The equation (12) and (13) describe the mathematical relationship between both referential.

$$\vec{H}_{sensor} = R_x(\alpha)\, R_y(\beta)\, R_z(\gamma)\, \vec{H} \tag{12}$$

$$\begin{bmatrix} H_a \\ H_b \\ H_c \end{bmatrix} = \begin{bmatrix} 1 & 0 & 0 \\ 0 & \cos\alpha & -\sin\alpha \\ 0 & \sin\alpha & \cos\alpha \end{bmatrix} \begin{bmatrix} \cos\beta & 0 & \sin\beta \\ 0 & 1 & 0 \\ -\sin\beta & 0 & \cos\beta \end{bmatrix} \begin{bmatrix} \cos\gamma & -\sin\gamma & 0 \\ \sin\gamma & \cos\gamma & 0 \\ 0 & 0 & 1 \end{bmatrix} \begin{bmatrix} H_x \\ H_y \\ H_z \end{bmatrix} \tag{13}$$

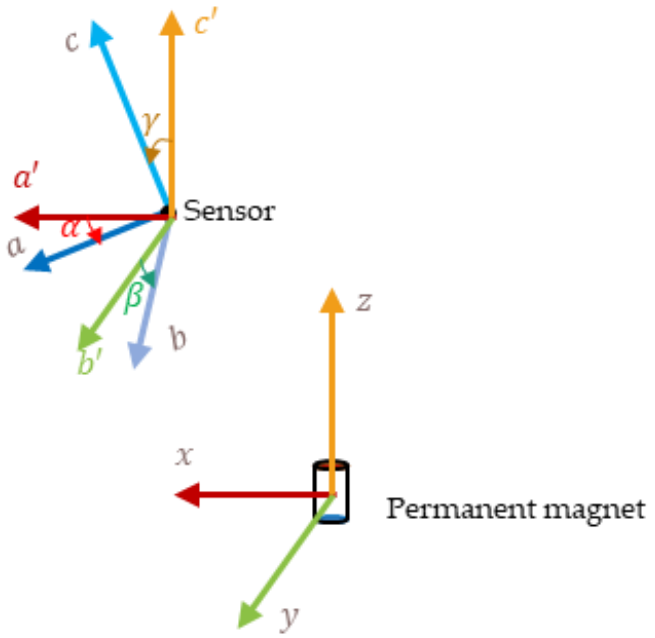

Figure 18 – Schematic highlights the sensor and magnet referential relationship using (α, β, γ).

To use the previous computational method, we need to compute the magnetic field vectors for each position inside the cube, rotate each magnetic field vector for the angle (α, β, γ), and then compute at which positions the value of $H_x = -0.743mT$ are still valid given that rotation. So, if 216 million points were already significant, the number of angles we plot for will increase the proportionality of the computational requirement. The same follows for the two-dimensional and three-dimensional sensor

computations. The calculations are for changes in angles of 30 degrees and only for one angle at a time while keeping the others null, leaving any linear combination out in the representation due to the computational intensity it would involve.

In

Figure 19, the tilting angle direction that is changed (α, β, γ) is different for each column, while the sensor sensitive direction (x,y,z) changes per row. For a one-directional sensor sensitive in the x-direction and detecting a magnetic field of -0.743mT, we observe no influence for any change in angle α, while maintaining $\beta = 0$ and $\gamma = 0$ (Figure 20 a)). This result is because we rotate the sensor over itself in the same position and measure the magnetic field direction is perpendicular to the rotation plane, which does not affect the field measured nor the position thus no difference from Figure 14.

However, an angle $(0, \beta \neq 0, 0)$ or $(0, 0, \gamma \neq 0)$ significantly influences the spatial positional uncertainty, reducing our ability to infer the position of the sensor sensitive in the x-direction as shown in Figure 20 b) and c), respectively. We can observe similar behaviors for any one-directional sensor, where the rotation in said directions transforms spatial positional uncertainty into a sphere where all the points inside can be a solution, given the correct linear combination angles α, β, γ. This shows how significant the tilting can be for position prediction.

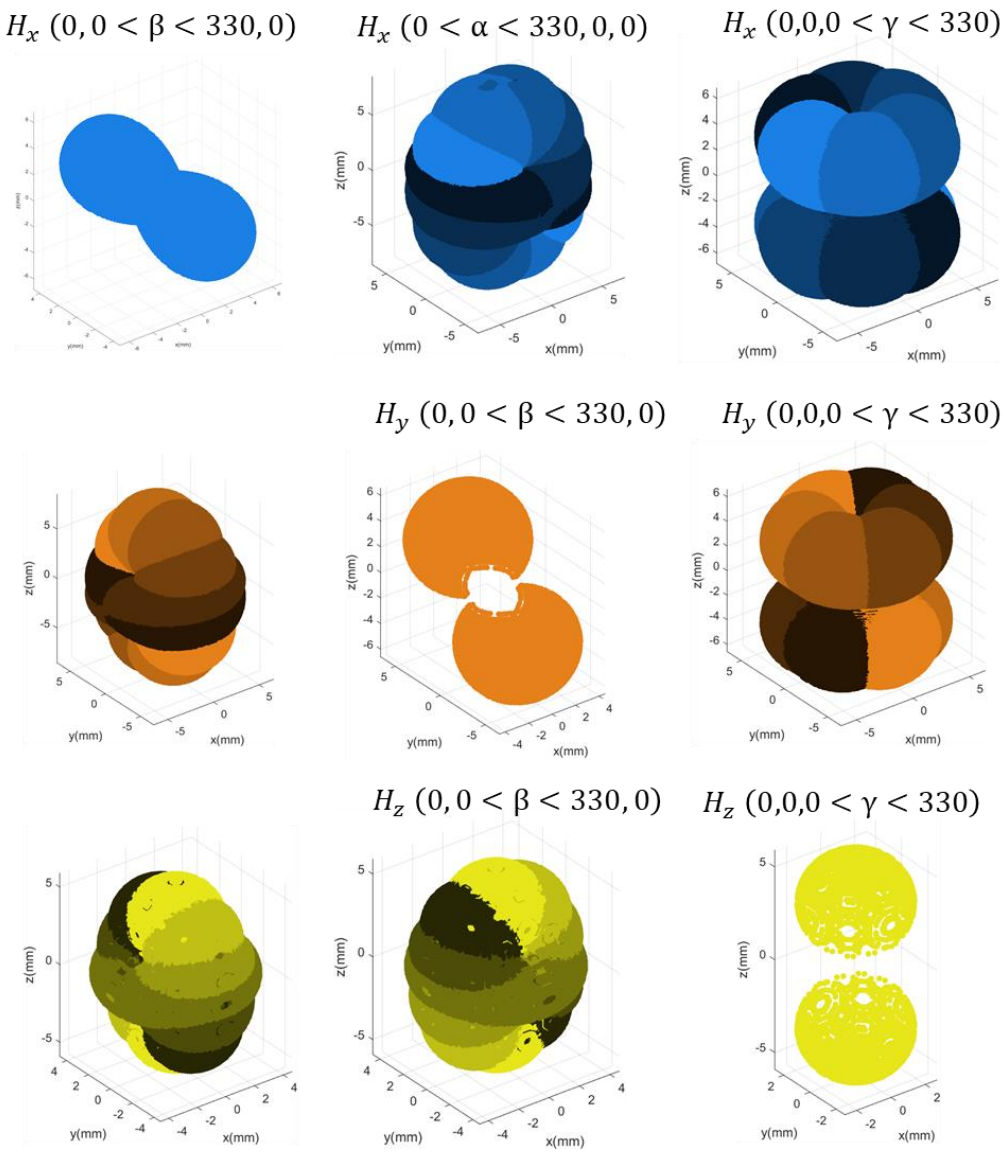

Figure 19 – Plots for the points in space where $H(H_x, H_y, H_z) = (-0.743, 0.743, 1.849)mT$.

For two-dimensional sensors, the spatial positional uncertainty reduces to a surface again. Instead of any position inside of a sphere, we get surfaces as solutions. The results on two-dimensional tilting sensors show us different spatial positional uncertainty depending on the chosen pair of sensitive directions. Figure 20 is an exciting finding because comparing the output in each direction could eliminate some angles, so a matrix could also gather information on the angle with two-dimensional sensors.

The three-dimensional sensor follows the trend to reduce the spatial positional uncertainty, improving further positional accuracy prediction. The computational requirements are very demanding, so it was not possible to represent it visually. However, if all linear combination angles α, β, γ were considered the results could reveal interesting patterns.

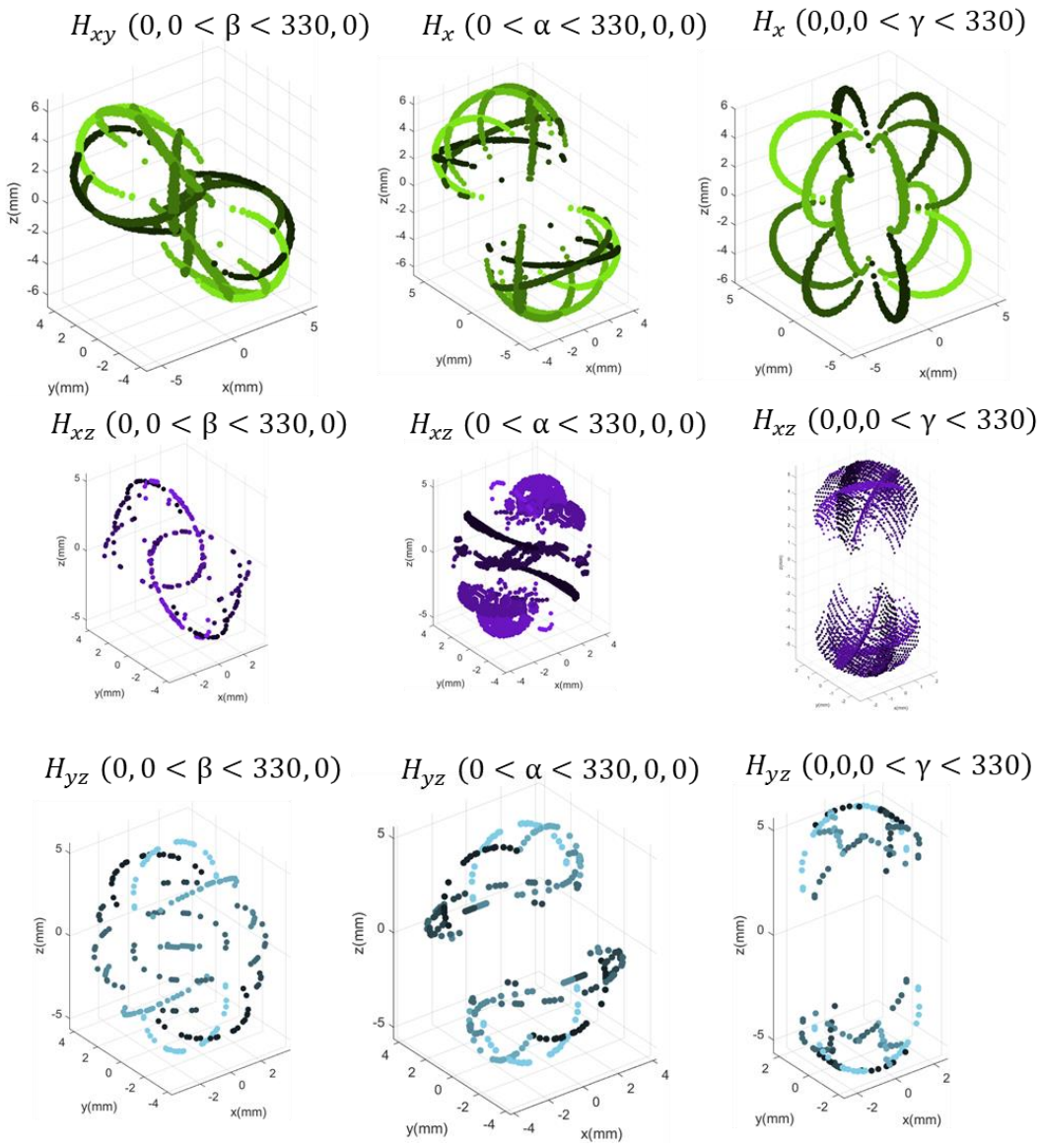

Figure 20 – Plots for the points in space where $H(H_x, H_y, H_z) = (-0.743, 0.743, 1.849)mT$

Increasing the number of sensor dimensions has proven to be an effective strategy to improve spatial position accuracy. Divergence and curl of the H field could help us add further dimensions and improve accuracy. A possible solution for acquiring said dimensions sensor matrices. Significant potential for these systems with precisions in the order of the 200µm [30], only with the one-dimensional sensor. Another strategy to mitigate the particular positional uncertainty would be to use probabilistic algorithms by considering the last position and field measured and inferring how likely the change in the magnetic field would correspond to an angle or a coordinate change or both given a certain deformation. The development of such algorithms is outside this thesis scope, but we understand that algorithms based on the three dimensions of the field vector, taking advantage of the matrices ability to measure curl and divergence of the magnetic field vector and knowing the previous position of the sensor all together could significantly improve the special positional accuracy.

2.3.2 A flexible sensor matrix solution

In Figure 11 we describe the working principle of a sensor-magnet system, assuming we can accurately determine the magnet position in space. Being able to measure the initial and final position of the magnet gives us the distance and direction the magnet moved in space. If the magnet is a point, we can say we measure the deformation of the elastomer on the point the permanent magnet is. Thus, saying the sensor-magnet system is, in essence, point-deformation sensors.

This thesis proposes to study the possibility of changing the sensor-magnet system from a single-point deformation system to a multi-point deformation system. We propose to cover the whole surface of the finger with a matrix of sensors and to have a magnet fixed at the bottom (see Figure 22). Assuming the proper algorithms and technology could accurately determine the position of the sensor in space, using methodologies discussed in the previous section, we could measure the surface's deformation. Our argument stands on the concept that the accurate deformation of the elastomer is the best possible measurement to infer the system of forces applied. The more accurately we can determine the deformation of the elastomer in real-time, the best estimation of the system of forces, and all the mechanical tactile information we can gather.

Finally, and as a bonus feature, such a design also enables the sensors to be on the surface of the finger, opening possibilities for temperature, humidity, and other contact sensing possibilities, which can be very attractive for tactile applications.

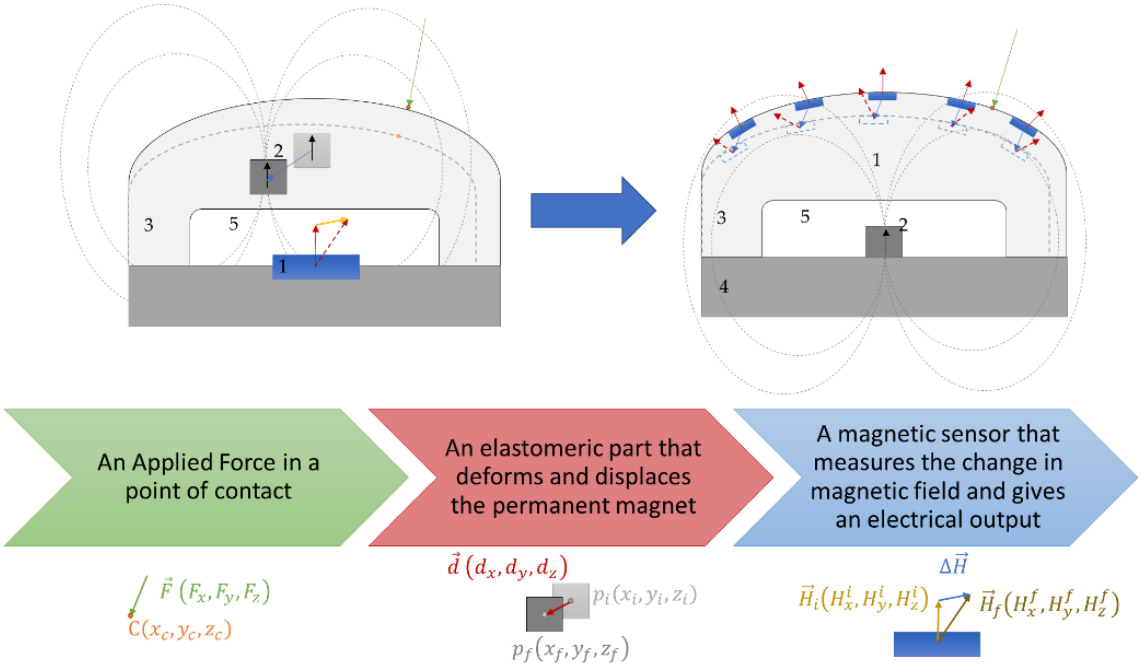

Figure 21 – From a single point deformation sensor to a multi-point deformation sensor.

1. Moreno, P.; Nunes, R.; Figueiredo, R.; Ferreira, R.; Bernardino, A.; Santos-Victor, J.; Beira, R.; Vargas, L.; Aragão, D.; Aragão, M. Robot 2015: Second Iberian Robotics Conference: Advances in Robotics, Volume 1. *Advances in Intelligent Systems and Computing* **2016**, *417*, 17–28, doi:10.1007/978-3-319-27146-0.

2. Feix, T.; Pawlik, R.; Schmiedmayer, H.-B.; Romero, J.; Kragi, D. A Comprehensive Grasp Taxonomy. *Robotics, Science and Systems Conference: Workshop on Understanding the Human Hand for Advancing Robotic Manipulation* **2009**, 2–3.

3. Parmiggiani, A.; Maggiali, M.; Natale, L.; Nori, F.; Schmitz, A.; Tsagarakis, N.; Victor, J.S.; Becchi, F.; Sandini, G.; Metta, G. The Design of the ICub Humanoid Robot. *International Journal of Humanoid Robotics* **2012**, *9*, 1–24, doi:10.1142/S0219843612500272.

4. Youssefian, S.; Rahbar, N.; Torres-Jara, E. Contact Behavior of Soft Spherical Tactile Sensors. *IEEE Sensors Journal* **2014**, *14*, 1435–1442, doi:10.1109/JSEN.2013.2296208.

5. Bicchi, A. Hands for Dexterous Manipulation and Robust Grasping: A Difficult Road toward Simplicity. *IEEE Transactions on Robotics and Automation* **2000**, *16*, 652–662, doi:10.1109/70.897777.

6. Yousef, H.; Boukallel, M.; Althoefer, K. Tactile Sensing for Dexterous In-Hand Manipulation in Robotics - A Review. *Sensors and Actuators, A: Physical* **2011**, *167*, 171–187, doi:10.1016/j.sna.2011.02.038.

7. Mason, M.T. Toward Robotic Manipulation. *Annual Review of Control, Robotics, and Autonomous Systems* **2018**, *1*, 1–28, doi:10.1146/annurev-control-060117-104848.

8. Li, Q.; Kroemer, O.; Su, Z.; Veiga, F.F.; Kaboli, M.; Ritter, H.J. A Review of Tactile Information: Perception and Action through Touch. *IEEE Transactions on Robotics* **2020**, *36*, 1619–1634, doi:10.1109/TRO.2020.3003230.

9. Dahiya, R.S.; Valle, M.; Metta, G. System Approach: A Paradigm for Robotic Tactile Sensing. *International Workshop on Advanced Motion Control, AMC* **2008**, *1*, 110–115, doi:10.1109/AMC.2008.4516050.

10. Dahiya, R.S.; Mittendorfer, P.; Valle, M.; Cheng, G.; Lumelsky, V.J. Directions toward Effective Utilization of Tactile Skin: A Review. *IEEE Sensors Journal* **2013**, *13*, 4121–4138, doi:10.1109/JSEN.2013.2279056.

11. Kappassov, Z.; Corrales, J.A.; Perdereau, V. Tactile Sensing in Dexterous Robot Hands - Review. *Robotics and Autonomous Systems* **2015**, *74*, 195–220, doi:10.1016/j.robot.2015.07.015.

12. Paulino, T.; Ribeiro, P.; Neto, M.; Cardoso, S.; Schmitz, A.; Santos-Victor, J.; Bernardino, A.; Jamone, L. Low-Cost 3-Axis Soft Tactile Sensors for the Human-Friendly Robot Vizzy. In Proceedings of the Proceedings - IEEE International Conference on Robotics and Automation; 2017; pp. 966–971.

13. Tekskan FlexiForce Load/Force Sensors and Systems Available online: http://www.tekscan.com/flexiforce.html.

14. Uart, W.; Voltage, D. OptoForce Analog Signal Converter. **2015**.

15. Peratech Touch Development Kit Available online: http://www.peratech.com/qtc-touch-processing-unit.html.

16. SynTouch Sensor Technology Available online: https://www.syntouchinc.com/sensor-technology/.

17. Whitesides, G.M. Soft Robotics. *Angewandte Chemie - International Edition* **2018**, *57*, 4258–4273, doi:10.1002/anie.201800907.

18. Lu, N.; Kim, D.H. Flexible and Stretchable Electronics Paving the Way for Soft Robotics. *Soft Robotics* **2014**, *1*, 53–62, doi:10.1089/soro.2013.0005.

19. Wattanasarn, S.; Noda, K.; Matsumoto, K.; Shimoyama, I. 3D Flexible Tactile Sensor Using Electromagnetic Induction Coils. *Proceedings of the IEEE International Conference on Micro Electro Mechanical Systems (MEMS)* **2012**, 488–491, doi:10.1109/MEMSYS.2012.6170230.

20. Ribeiro, P.; Alfhadel, A.; Franco, F.; Freitas, S.; Bernardino, A.; Schmitz, A.; Jamone, L. Bio-Inspired Ciliary Force Sensor for Robotic Platforms. **2016**.

21. Alfadhel, A.; Khan, M.A.; Freitas, S.C. de; Kosel, J.; Member, S. Magnetic Tactile Sensor for Braille Reading. **2016**, 1–6, doi:10.1109/JSEN.2016.2558599.

22. Hellebrekers, T.; Zhang, K.; Veloso, M.; Kroemer, O.; Majidi, C. Localization and Force-Feedback with Soft Magnetic Stickers for Precise Robot Manipulation. *IEEE International Conference on Intelligent Robots and Systems* **2020**, 8867–8874, doi:10.1109/IROS45743.2020.9341281.

23. Clark, J.J. A Magnetic Field Based Compliance Matching Sensor for High Resolution, High Compliance Tactile Sensing. *Robotics and Automation, 1988. Proceedings., 1988 IEEE International Conference on* **1988**, 772–777 vol.2, doi:10.1109/ROBOT.1988.12152.

24. Takenawa, S. A Magnetic Type Tactile Sensor Using a Two-Dimensional Array of Inductors. *Proceedings - IEEE International Conference on Robotics and Automation* **2009**, 3295–3300, doi:10.1109/ROBOT.2009.5152420.

25. Goka, M.; Nakamoto, H.; Takenawa, S. A Magnetic Type Tactile Sensor by GMR Elements and

Inductors. *IEEE/RSJ 2010 International Conference on Intelligent Robots and Systems, IROS 2010 - Conference Proceedings* **2010**, 885–890, doi:10.1109/IROS.2010.5650283.

26. Ledermann, C.; Wirges, S.; Oertel, D.; Mende, M.; Woern, H. Tactile Sensor on a Magnetic Basis Using Novel 3D Hall Sensor - First Prototypes and Results. *INES 2013 - IEEE 17th International Conference on Intelligent Engineering Systems, Proceedings* **2013**, 55–60, doi:10.1109/INES.2013.6632782.

27. Wang, H.; de Boer, G.; Kow, J.; Ghajari, M.; Alazmani, A.; Hewson, R.; Culmer, P. A Low-Cost Soft Tactile Sensing Array Using 3D Hall Sensors. *Procedia Engineering* **2016**, *168*, 650–653, doi:10.1016/j.proeng.2016.11.237.

28. Hackwood, S.; Beni, G. Shear-Sensitive Magnetoresistive Robotic Tactile Sensor. *IEEE Transactions on Magnetics* **1986**, *22*, 394–396, doi:10.1109/TMAG.1986.1064386.

29. Hackwood, S.; Beni, G.; Hornak, L. a.; Wolfe, R.; Nelson, T.J.J. A Torque-Sensitive Tactile Array for Robotics. *The International Journal of Robotics Research* **1983**, *2*, 46–50, doi:10.1177/027836498300200204.

30. Tomo, T.P.; Wong, W.K.; Schmitz, A.; Kristanto, H.; Sarazin, A.; Jamone, L.; Somlor, S.; Sugano, S. A Modular, Distributed, Soft, 3-Axis Sensor System for Robot Hands. *IEEE-RAS International Conference on Humanoid Robots* **2016**, 454–460, doi:10.1109/HUMANOIDS.2016.7803315.

31. Tomo, T.P.; Somlor, S.; Schmitz, A.; Jamone, L.; Huang, W.; Kristanto, H.; Sugano, S. Design and Characterization of a Three-Axis Hall Effect-Based Soft Skin Sensor. *Sensors (Switzerland)* **2016**, *16*, doi:10.3390/s16040491.

32. Yan, Y.; Hu, Z.; Yang, Z.; Yuan, W.; Song, C.; Pan, J.; Shen, Y. Soft Magnetic Skin for Super-Resolution Tactile Sensing with Force Self-Decoupling. *Science Robotics* **2021**, *6*, eabc8801, doi:10.1126/scirobotics.abc8801.

33. Tomo, T.P.; Schmitz, A.; Wong, W.K.; Kristanto, H.; Somlor, S.; Hwang, J.; Jamone, L.; Sugano, S. Covering a Robot Fingertip With USkin: A Soft Electronic Skin With Distributed 3-Axis Force Sensitive Elements for Robot Hands. *IEEE Robotics and Automation Letters* **2018**, *3*, 124–131, doi:10.1109/LRA.2017.2734965.

34. Tomo, T.P.; Regoli, M.; Schmitz, A.; Natale, L.; Kristanto, H.; Somlor, S.; Jamone, L.; Metta, G.; Sugano, S. A New Silicone Structure for USkin - A Soft, Distributed, Digital 3-Axis Skin Sensor and Its Integration on the Humanoid Robot ICub. *IEEE Robotics and Automation Letters* **2018**, *3*, 2584–2591, doi:10.1109/LRA.2018.2812915.

35. COEY, J.M.D. *Magnetism and Magnetic Materials*; Cambridge University Press: Dublin, 2009;

ISBN 9780521816144.

36. Model, R.; Trahms, L. An Inverse Problem of Magnetic Source Localization. *Numer Algor* **1993**, *5*, 603–610, doi:10.1007/bf02221587.

37. Wang, X.; Meng, M.Q.H.; Hu, C. A Localization Method Using 3-Axis Magnetoresistive Sensors for Tracking of Capsule Endoscope. *Annual International Conference of the IEEE Engineering in Medicine and Biology - Proceedings* **2006**, *1*, 2522–2525, doi:10.1109/IEMBS.2006.260711.

38. Sun, Z.; Foong, S.; Marechal, L.; Teo, T.H.; Tan, U.X.; Shabbir, A. Using Heterogeneous Sensory Measurements in a Compliant Magnetic Localization System for Medical Intervention. *IEEE/ASME International Conference on Advanced Intelligent Mechatronics, AIM* **2015**, *2015-Augus*, 133–138, doi:10.1109/AIM.2015.7222521.

39. Marechal, L.; Foong, S.; Sun, Z.; Wood, K.L. Design Optimization of the Sensor Spatial Arrangement in a Direct Magnetic Field-Based Localization System for Medical Applications. *Proceedings of the Annual International Conference of the IEEE Engineering in Medicine and Biology Society, EMBS* **2015**, *2015-Novem*, 897–900, doi:10.1109/EMBC.2015.7318507.

40. Ribeiro, P.; Neto, M.; Cardoso, S. Strategy for Determining a Magnet Position in a 2-D Space Using 1-D Sensors. *IEEE Transactions on Magnetics* **2018**, *54*, doi:10.1109/TMAG.2018.2851928.

41. Wu, F.Y.; Foong, S.; Sun, Z. A Hybrid Field Model for Enhanced Magnetic Localization and Position Control. *IEEE/ASME Transactions on Mechatronics* **2015**, *20*, 1278–1287, doi:10.1109/TMECH.2014.2341644.

42. Wu, F.; Robert, N.M.; Frey, D.D.; Foong, S. Enhanced Magnetic Localization with Artificial Neural Network Field Models. *Robotics and Automation (ICRA), 2013 IEEE International Conference on* **2013**, 1560–1565, doi:10.1109/ICRA.2013.6630778.

43. Derby, N.; Olbert, S. Cylindrical Magnets and Ideal Solenoids. *American Journal of Physics* **2010**, *78*, 229–235, doi:10.1119/1.3256157.

44. Silva, A. v.; Leitao, D.C.; Valadeiro, J.; Amaral, J.; Freitas, P.P.; Cardoso, S. Linearization Strategies for High Sensitivity Magnetoresistive Sensors. *The European Physical Journal Applied Physics* **2015**, *72*, 10601, doi:10.1051/epjap/2015150214.

45. Parkin, S.S.P. Flexible Giant Magnetoresistance Sensors. *Applied Physics Letters* **1996**, *69*, 3092–3094, doi:10.1063/1.117315.

46. Gaspar, J.; Fonseca, H.; Paz, E.; Costa, M.; Martins, M.; Ferreira, R.; Cardoso, S.; Freitas, P.P. Fabrication and Mechanical Characterization of Flexible Devices with Sensors with

Magnetoresistance Responses above 150 %. 10–12.

47. Valadeiro, J.; Amaral, J.; Leitao, D.C.; Silva, A. v.; Gaspar, J.; Silva, M.; Costa, M.; Martins, M.; Franco, F.; Fonseca, H.; et al. Bending Effect on Magnetoresistive Silicon Probes. *IEEE Transactions on Magnetics* **2015**, *51*, 3–6, doi:10.1109/TMAG.2015.2441956.

48. Makarov, D.; Melzer, M.; Karnaushenko, D.; Schmidt, O.G.; Makarov, D.; Melzer, M.; Karnaushenko, D.; Schmidt, O.G. Shapeable Magnetoelectronics. *Applied Physics Review* **2016**, *3*, 011101, doi:10.1063/1.4938497.

49. Uhrmann, T.; Bär, L.; Dimopoulos, T.; Wiese, N.; Rührig, M.; Lechner, a. Magnetostrictive GMR Sensor on Flexible Polyimide Substrates. *Journal of Magnetism and Magnetic Materials* **2006**, *307*, 209–211, doi:10.1016/j.jmmm.2006.03.070.

50. Karnaushenko, D.; Makarov, D.; St??ber, M.; Karnaushenko, D.D.; Baunack, S.; Schmidt, O.G. High-Performance Magnetic Sensorics for Printable and Flexible Electronics. *Advanced Materials* **2015**, *27*, 880–885, doi:10.1002/adma.201403907.

51. Singh, M.; Haverinen, H.M.; Dhagat, P.; Jabbour, G.E. Inkjet Printing-Process and Its Applications. *Advanced Materials* **2010**, *22*, 673–685, doi:10.1002/adma.200901141.

52. Singh, W.S.; Rao, B.P.C.; Thirunavukkarasu, S.; Jayakumar, T. Flexible GMR Sensor Array for Magnetic Flux Leakage Testing of Steel Track Ropes. *Journal of Sensors* **2012**, *2012*, doi:10.1155/2012/129074.

53. Gaspar, J.; Fonseca, H.; Paz, E.; Martins, M.; Valadeiro, J.; Cardoso, S.; Ferreira, R.; Freitas, P.P. Flexible Magnetoresistive Sensors Designed for Conformal Integration. *IEEE Transactions on Magnetics* **2017**, *53*, 5–8, doi:10.1109/TMAG.2016.2623669.

54. Melzer, M.; Makarov, D.; Calvimontes, A.; Karnaushenko, D.; Baunack, S.; Kaltofen, R.; Mei, Y.; Schmidt, O.G. Stretchable Magnetoelectronics. *Nano Letters* **2011**, *11*, 2522–2526, doi:10.1021/nl201108b.

55. Melzer, M.; Lin, G.; Makarov, D.; Schmidt, O.G. Stretchable Spin Valves on Elastomer Membranes by Predetermined Periodic Fracture and Random Wrinkling. *Advanced Materials* **2012**, *24*, 6468–6472, doi:10.1002/adma.201201898.

56. Mimoun, B.; Pham, H.T.M.; Henneken, V.; Dekker, R. Residue-Free Plasma Etching of Polyimide Coatings for Small Pitch Vias with Improved Step Coverage. *Journal of Vacuum Science & Technology B: Microelectronics and Nanometer Structures* **2013**, *31*, 021201, doi:10.1116/1.4788795.

57. Dick, A.R.; Bell, W.K.; Luke, B.; Maines, E.; Mueller, B.; Rawlings, B.; Kohl, P.A.; Grant Willson, C. High Aspect Ratio Patterning of Photosensitive Polyimide with Low Thermal

Expansion Coefficient and Low Dielectric Constant. *Journal of Micro/Nanolithography, MEMS, and MOEMS* **2016**, *15*, 033503, doi:10.1117/1.JMM.15.3.033503.

58. Gehanno, V.; Freitas, P.P.; Veloso, A.; Ferreira, J.; Almeida, B.; Sousa, J.B.; Kling, A.; Soares, J.C.; da Silva, M.F. Ion Beam Deposition of Mn-Ir Spin Valves. *IEEE Transactions on Magnetics* **1999**, *35*, 4361–4367, doi:10.1109/20.799086.

59. Alfadhel, A.; Khan, M.A.; Cardoso, S.; Leitao, D.; Kosel, J. A Magnetoresistive Tactile Sensor for Harsh Environment Applications. *Sensors (Switzerland)* **2016**, *16*, doi:10.3390/s16050650.

60. Fu, Y.B.; Ogden, R.W. *Nonlinear Elasticity: Theory and Applications*; Cambridge University Press: Cambrigde, 2001; ISBN 9780511526466.

Chapter 3

The making of a magnetic tactile sensor

3.1 Introduction

The tactile sensor proposed covers the whole surface of the finger with a matrix of sensors that retrieves the necessary magnetic field information to reconstruct the fingertip deformation (see Figure 22). To fabricate such a system, we need to achieve two main milestones: 1) to find a suitable way to measure the magnetic field; 2) to communicate the electrical information from the sensors to the robot.

3.2 Magnetic sensors

There are several commercially available technologies to measure magnetic fields at room temperature: Anisotropic magnetoresistance (AMR), Hall effect, Gian Magnetoresistance (GMR), and Tunnel Magnetoresistance (TMR). At INESC-MN facilities, we have the opportunity to choose from the three technologies detailed in Table 4.

Table 4 – Technologies available at INESC-MN and how they compare[44].

	Anisotropic Magnetoresistance	**Giant Magnetoresistance**	**Tunnel Magnetoresistance**
Magnetoresistance ratio	2-5%	6-20%	70-300%
Field linear range	Down to 1mT	Down to 1mT	Down to +- 2mT
Thermal stability	250 ºC	320 ºC	360 ºC
Thermal treatment	No need	250 ºC	350 ºC
Electrical robustness vs. electrostatic discharge	Very good	Very good	Fair
Microfabrication Process complexity and materials cost	Low complexity and accessible materials	Medium complexity and expensive materials	High complexity and expensive materials

All are mature technologies that could be used to measure the magnetic field for the tactile sensor. As previously stated, detectivity is a crucial aspect to minimize spatial positional uncertainty. We have opted to use GMR sensors because of their acceptable trade-off between fabrication complexity to magnetoresistance ratio, higher thermal stability, and excellent electrical robustness.

3.3 The case for the flexible hybrid process approach

The communication of the electrical signal from the sensor on the finger surface to the robot is a challenge because it requires flexible interconnections that can sustain the mechanical stresses imposed by tactile applications. The fabrication of magnetic sensors with high performance is a significant challenge, where reducing detectivity, increase the operational range are all valid and current topics. The goal to implement the sensors on a flexible matrix adds on top of the extremely high challenge of electronic performance, additional challenges regarding mechanical robustness and flexibility. Depending on the application the trade-off between the mechanical performance and electrical performance can change, and for some applications maybe lowering the performance can be acceptable. However, for tactile sensing, both the time response and detectivity are drivers for electronic performance. Regarding mechanical requirements the robustness is key.

To date we can divide flexible magnetic sensors into four main categories by considering how they are made. The deposition using standard directly onto a flexible substrate, which has been tested from 1996 [35] to 2021. The deposition using magnetron sputtering on to a spin coated wafer and further release of the flexible film with the sensors [36]. Depositing in a Si wafer and thinning it to enhance flexibility [37]. Fabrication of spin valve devices directly on a Si substrate, followed by the fabrication of aluminium contacts embedded on polyimide films, then removing the silicon by DRIE to make the contacts flexible.

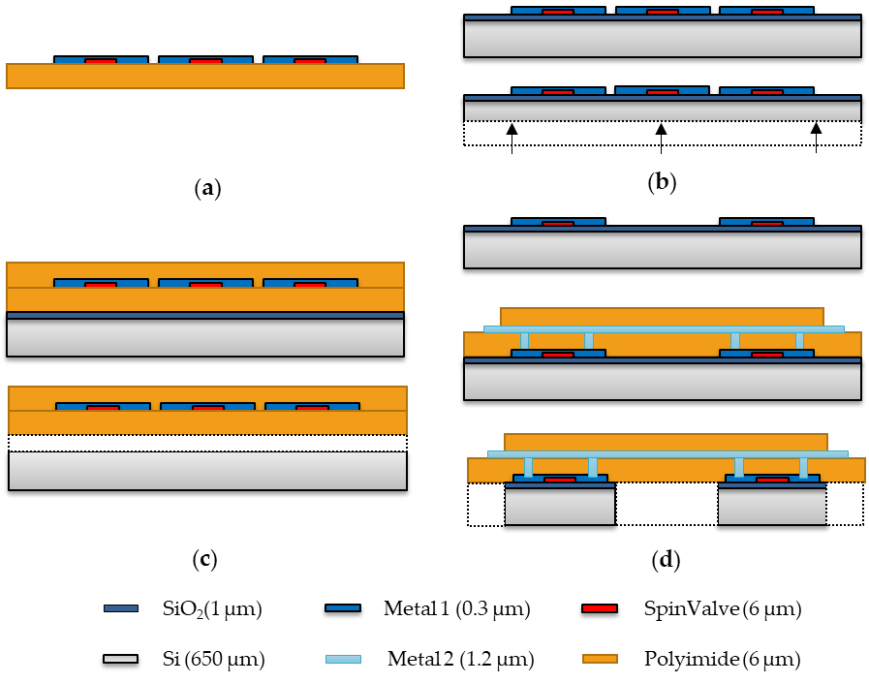

Figure 22. (a) Fabrication of spin valve devices directly onto a flexible substrate; (b) Fabrication of spin valve devices directly on a Si substrate and thinning it after; (c) Fabrication of spin valve devices directly on a polyimide thin film and then removing a intermediate layer of SiO2 to release from the Si substrate; (d) Fabrication of spin valve devices directly on a Si substrate, followed by the fabrication of aluminium contacts embedded on polyimide films, then removing the silicon by DRIE to make the contacts flexible. (DRAWINGS NOT TO SCALE)

Academic literature has several examples demonstrating the ability to fabricate spin-valve devices directly on flexible substrates [35,38,39], even using printable electronics [40,41] instead of standard sputtering techniques. Those examples highlight the challenges and disadvantages of such an approach, on the one hand, the performance of spintronic devices in rigid substrates is not matched, and on the other, the small dimension devices are very hard to replicate[42].

Magnetoresistive sensors consist of a layer sequence with typical film thicknesses ranging from 0.5-2 nm, showing a magnetic response highly dependent on the film texture. The impact of film strain, bending and thermal stress on the sensor transport curves has also been reported to be relevant factors to consider, for films deposited on Si [37] (as Figure 22 (b)), polyimide [38,43] (as Figure 22 (a) and (c)), or stretchable PDMS substrates [44,45] (as Figure 22 (a)). To reduce the complexity introduced by mechanical stresses on these devices we propose a hybrid process, where the sensors are processed in Silicon wafers and then interconnected using flexible contacts, as Figure 22 (d).

In addition, sensor applications usually have multiplexing requirements, therefore flexible elements should be compatible with other large-scale production, compact size technologies, e.g., CMOS nanoelectronics chips (fabricated on silicon, rigid substrates), allowing the production of high-density matrixes of sensors and other microcircuit components.

3.4 Facilities

The development and fabrication of the process proposed Figure 22 (d), requires access to microfabrication facilities. The fabrication of the devices detailed in this thesis take advantage of the cleanroom facilities available in INESC-MN and INL. All the sensor deposition presented on this work was deposited by a Nordiko 3600 machine, in an ISO 5 Class Clean Room at INESC-MN. The polyimide and flexible contacts definition process described was done at INL in the initial prototype. The following 3 prototypes lead to the develop a similar process at INESC-MN cleanroom, but because the available resources are not the same a different approach had to be developed. The steps that required DRIE was always done at INL.

3.4.1 Fabrication

3.4.1.1 Sensor Deposition and Definition (IBD Nordiko 3600)

Ion Beam deposition (IBD) is a process that uses an ion beam to sputter a material onto a substrate. In Nordiko 3600 a Xe plasma is created, accelerated against the target, and consequently deflected to the substrate. This is commonly identified as a secondary ion beam deposition or ion sputter deposition.

In Nordiko 3600 system the wafers are loaded one by one. For it to pick different wafers, the

Cassette (3.1) is equipped with a lift under it so that depending on its height the arm picks the wafer for the desired process parameters.

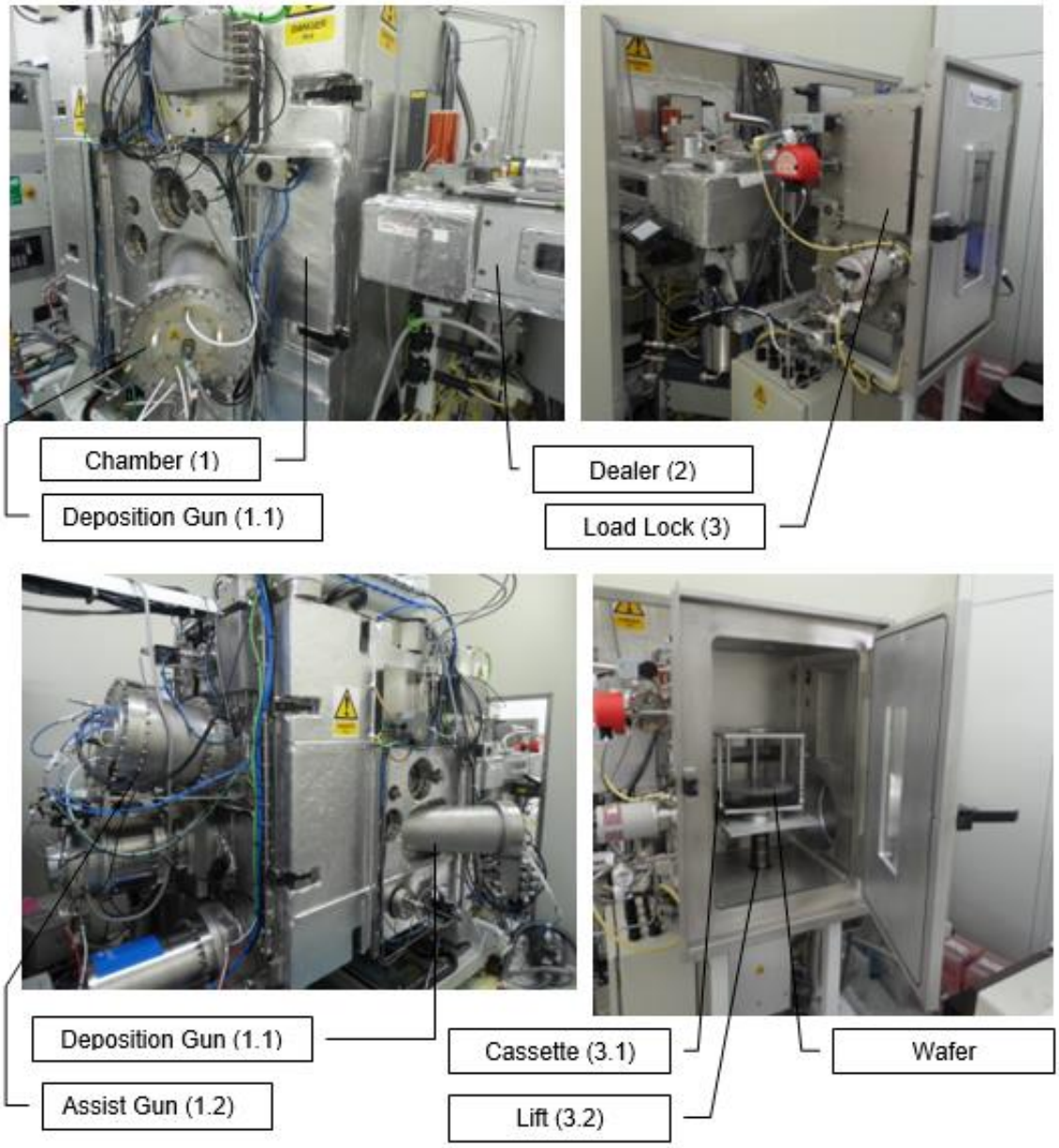

Figure 23 - Photographs of the N3600 at INESC-MN (taken at 19 of August 2014). a) Chamber, Dealer and Deposition Gun. b) Chamber showing the Assist Gun and the Cryogenic Pump. c) Load Lock and Dealer. d) Open Load Lock showing the placement of wafer on the Cassette.

A photograph was taken of the inside of the chamber when it was opened to change the targets and is presented Figure 24. The system incorporates two ion beam guns (Deposition Gun (1.1) and Assist Gun (1.2)), a Substrate Table (1.6) and a Target Assembly (1.5). The Target Assembly (1.5), comprising 6 targets, can rotate around its axis to align each target with the direction of the beam. The Target Shutter (1.4) covers the target to minimize the target contamination during process, either deposition of other materials or Ion Milling processes.

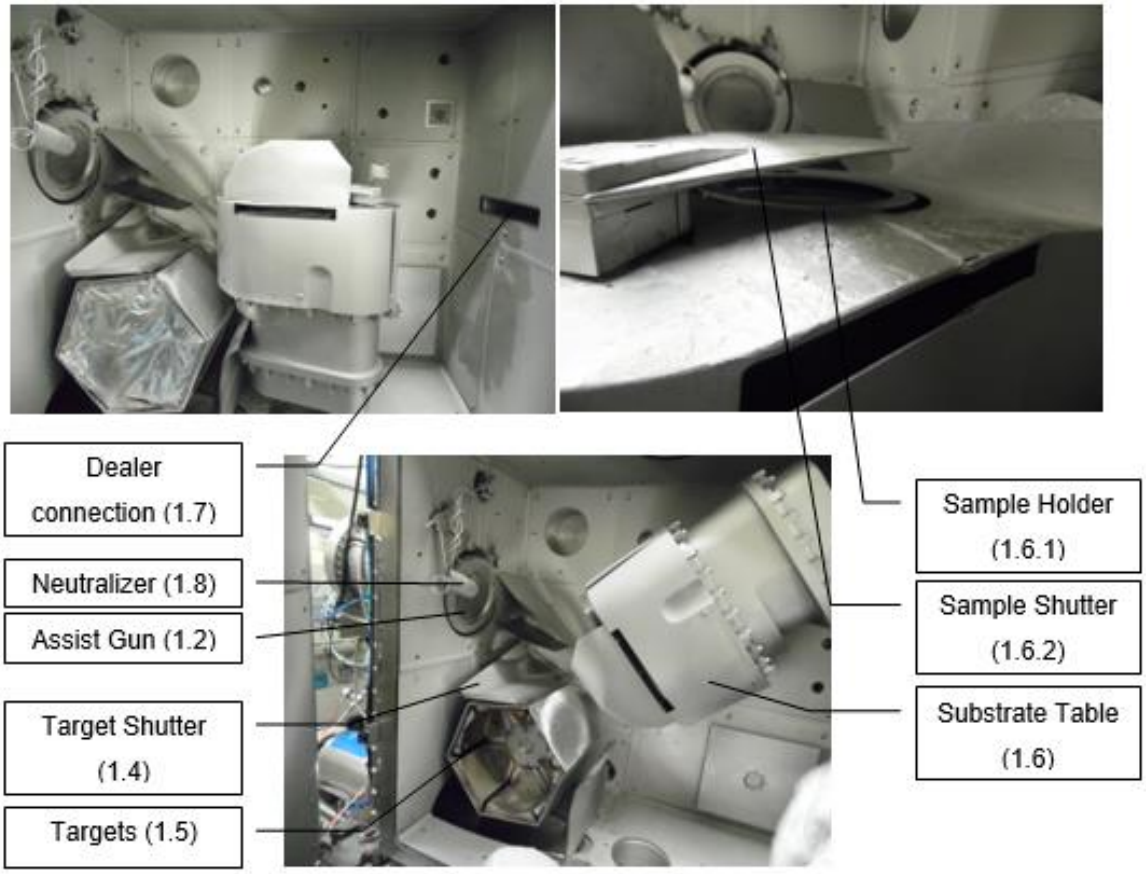

Figure 24 - Photograph of the inside of the N3600 Chamber at INESC-MN. a) Substrate table at 0 deg.b) Substrate table and shutter. c) Substrate table at 130 deg.

The samples are loaded from the Cassette (3.1) through the Dealer gate (1.7) and placed on the Substrate Holder (1.6.1). On the Substrate Table (1.6) an electromagnet is used to produce a uniform and constant 50 Oe magnetic field over the wafer. The purpose of this field is to break the anisotropy, defining easy axis and exchange field directions during the deposition of magnetic materials. The Sample Shutter (1.6.2) covers the Substrate Table (1.6) protecting the samples during the gun's preparation steps. In timed processes, the opening of the Sample Shutter (1.6.2) coincides with the beginning of the countdown. The Substrate Holder (1.6.2) rotation can be controlled and is set to 30 rpm, improving the substrate uniformity not only on the Deposition but also in the Ion Milling processes. Furthermore, the Substrate Table (1.6) can be tilted to change the angle between the substrate and the Ion Beams and perform the loading and unloading steps. At 0 deg angle means that the table is horizontal, which corresponds to the loading/unloading of the wafer (Figure 24 a), while a 130 or 180 pan angle are common angles used to perform assisted and non-assisted deposition (Figure 24 c), respectively. For Ion Milling, where only the assisted gun (1.3) is used, 30 and 60 deg are commonly used.

3.4.1.2 Passivation (UHV II)

UHV II is a machine used for oxide deposition by sputtering from a 6 inch diameter 99.995% Al_2O_3 target. The UHV II is in a class 10000 clean room. This system was used for the depositing a 1000 Å insulating layer.

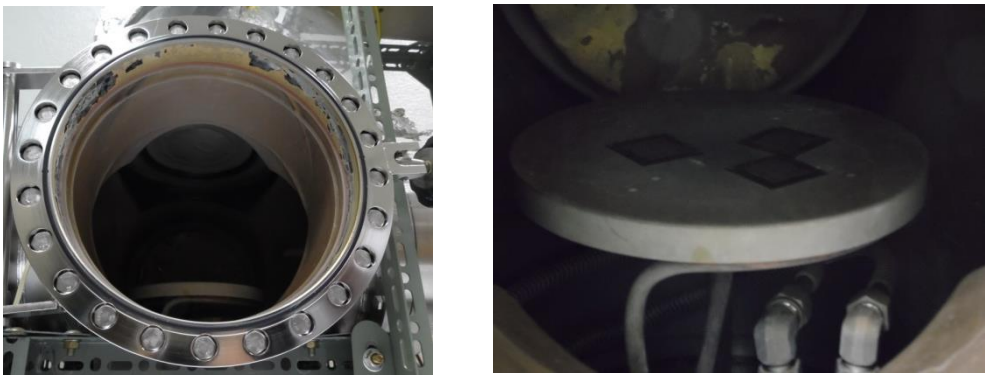

Figure 25 – Photographs from the inside chamber of UHV II machine.

This machine has inside the chamber only one target facing down and allows deposition of samples of 6 inch in diameter. Pressures of $3x10^{-7}$ Torr are needed to obtain the optimum deposition conditions.

3.4.1.3 Metallic Contacts (Nordiko 7000)

Nordiko 7000, installed in an ISO 4 clean room, is an automated cluster system, composed by a Load Lock connected to four chambers through a distribution chamber (dealer).

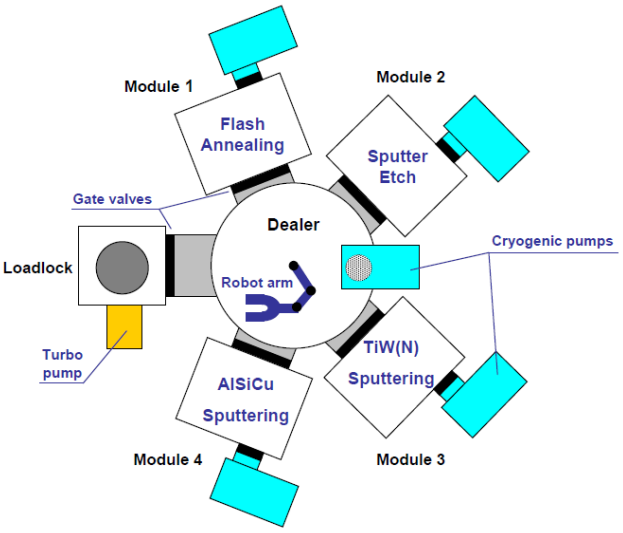

Figure 26 – N7000 schematic drawing (Ferreira, 2008)

This system was used for deposition of Al 3000 Å/TiW(N) 150 Å layers in the Top Contact Deposition Step. The films are deposited by sputtering (using Ar ions) from a sintered $Ti_{10}W_{90}$ target.

During the deposition, a flow of N_2 is used so that the deposited films incorporate ~50% of nitrogen which improves the passivation properties of the TiW layer.

3.4.1.4 Paterning (SVG track and DWL)

Microfabrication is the process by which individual devices with dimensions in the μm range are manufactured. To microfabricate fabricate spin valve devices the ability to selectively deposit or selectively remove material from a substrate is a requirement, thus etching, lift-off techniques and optical lithography were used.

Etching is a technique used to selectively remove material from a substrate. This can be achieved with three major techniques: Reactive Ion Etching, Chemical Etching and Physical Etching. The technique used was Physical Etching, particularly Ion Milling. The process starts with a substrate covered with a mask that selectively protects interest areas. The material that is not covered by the mask is removed. After that, the mask is removed leaving a substrate with a patterned material covering the area previously occupied by the mask, as shown in Figure 27.

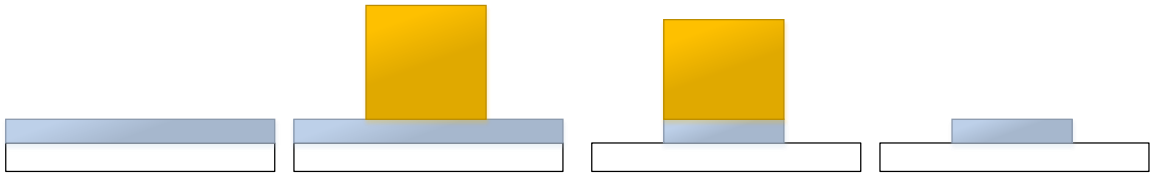

Figure 27 – Schematic of the etching microfabrication process.

On the other hand, in a ***lift-off*** technique, the aim is to selectively deposit material. It also starts with a substrate covered with a mask that selectively covers some portion of it. The material that is to be patterned is then deposited over the mask. Finally, the mask is removed taking with it the material covering the area previously un-occupied by the mask, as shown in Figure 28.

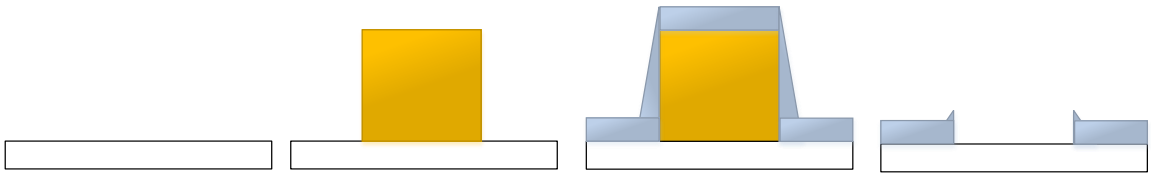

Figure 28 – Schematic of the Lift-off Microfabrication process.

The major advantage of the etching technique is that it allows the definition of very sharp features. However high control of the thickness is needed, and higher thicknesses need a high process time. Thus, it is used to etch small thicknesses and define sharp features.

The lift-off process is very good when used to pattern over existing material but is not suitable to pattern multilayer. Besides that, the features are often rough looking and thus not suitable to define sharp profiles.

Optical Lithography is a process used to create the micrometric patterns over the substrate using a photo sensitive polymer called photoresist.

Step 1 - Vapor Priming

The aim of this step is to improve the adhesion between the substrate and the photoresist film. This achieves by coating our substrate with a monolayer of HDMS (hexamethyldisilazane). Vapor priming has a total duration of 30 minutes and is constituted by several steps to remove water residues from the surface and depositing the HDMS.

Step 2 - Coating

The aim is to create a uniform photoresist coating with 1.45 μm thickness over the glass substrate. The process is performed in the SVG coater track, and it starts by dispensing a determined photoresist volume. Next the substrate is spun at 2500 rpm for 30 seconds to uniformly distribute the photoresist over the wafer. Next takes part a baking step at 90 °C for 60 seconds to evaporate the solvent and relive stresses accumulated during the spinning step.

Step 3 - Laser exposure

The substrate table has xzy freedom. The first step is to focus the laser fixing the z axis, then the origin point is determined. The next step is to load the mask and expose the areas that are meant to be developed. The parameters used were Energy 60 and Focus 80.

Step 4 - Resist Development

The last step of the lithography process is development. The substrate is baked at 110 ºC for 60 s, followed by a cooldown step of 30 s. Finally, a developer is used for 60 s to remove the exposed photoresist.

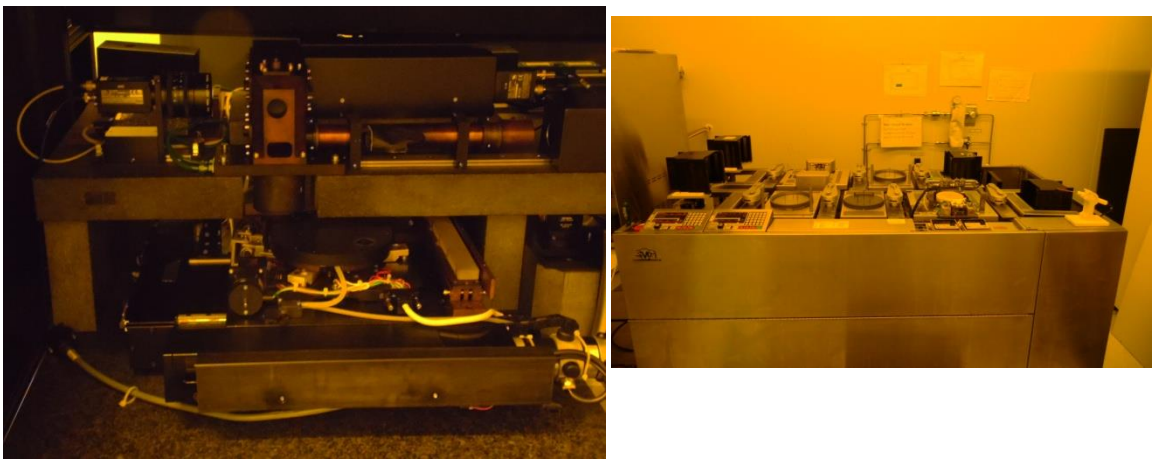

Figure 29 – Photographs taken in the yellow room: a) DWL stage and laser system; b) coating and development tracks on the SVG track system.

3.5 Flexible Sensing Matrix #01 (FHD_01)

3.5.1 Design

The main goal was to assess the feasibility of the flexible hybrid process, so we did not consider the electronic interface or the shape of the part. We kept the initial design simple and rather conceptual.

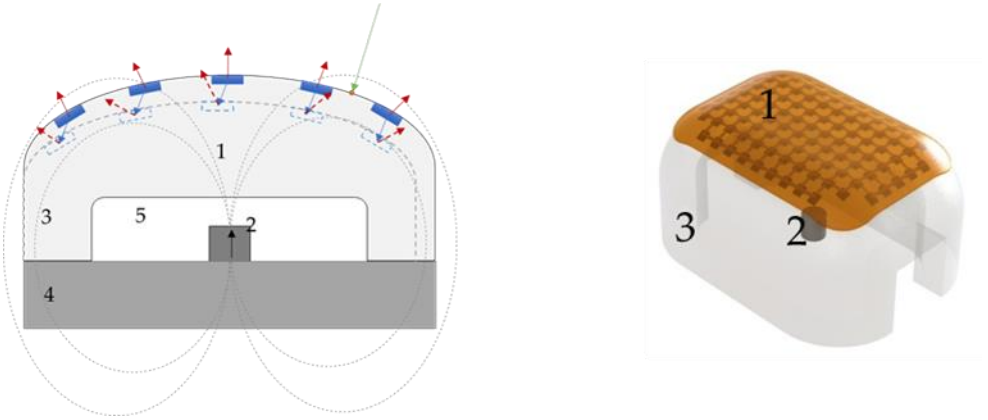

Figure 30. (a) Schematic view of the devices working principle (b) A CAD to illustrating the concept in 3D based on the middle phalange of the finger; The numbers in the Figure stand for: 1 – Sensors (blue); 2 – Cylindrical Nd Permanent Magnet; 3 – Polymeric silicone part; 4 – Robotic finger; 5 – Air gap; (- - -) Magnetic field lines for the permanent magnet. **(c)** 3D view of the FPC with the Si Chips embedded in the Elastomer part.

3.5.2 Process

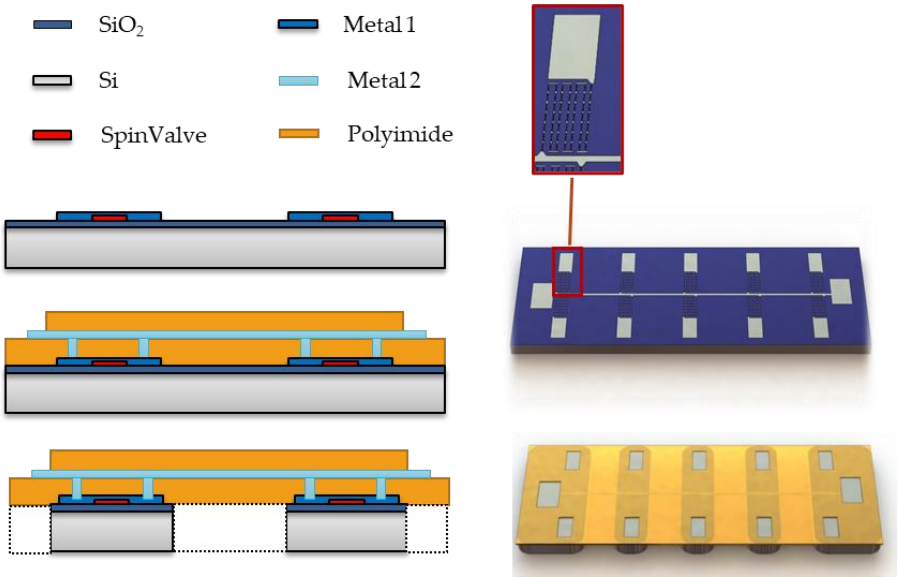

Figure 31. (a) Schematic view of the devices working principle (b) A CAD to illustrating the concept in 3D based on the middle phalange of the finger; The numbers in the Figure stand for: 1 – Sensors (blue); 2 – Cylindrical Nd Permanent Magnet; 3 – Polymeric silicone part; 4 – Robotic finger; 5 – Air gap; (- - -) Magnetic field lines for the permanent magnet. **(c)** 3D view of the FPC with the Si Chips embedded in the Elastomer part.

3.5.3 Results and next steps

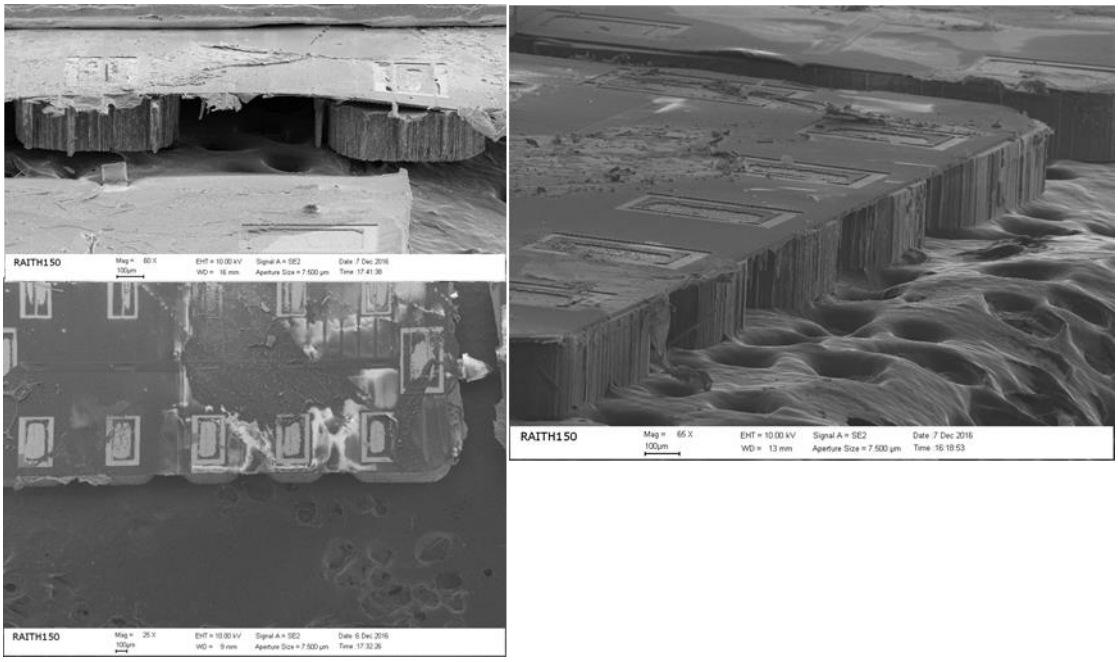

Figure 32. SEM images from a 5-island device seen from a) top showing the Si islands underneath the polyimide films and the contact pads. b) Orthogonal view of the device where one can observe the Si patterned side by Bosch Process. c) Lateral view of the device with the Polyimide film on top of two silicon islands.

During the fabrication of this device, several issues became obvious and can be observed in the SEM images in Figure 3. First, several residues on the surface of both the contact pads and the encapsulation layer of polyimide are observed, which were detrimental to the characterization of the post-processed devices. Secondly, the adhesion between the polyimide layer and the Si islands was apparent. Nevertheless, it showed the possibility of manufacturing this type of structure successfully. From an integration standpoint, the contacts were not accessible to interface an electronic interface

3.6 Flexible Sensing Matrix #02 (FHD_02)

3.6.1 Design

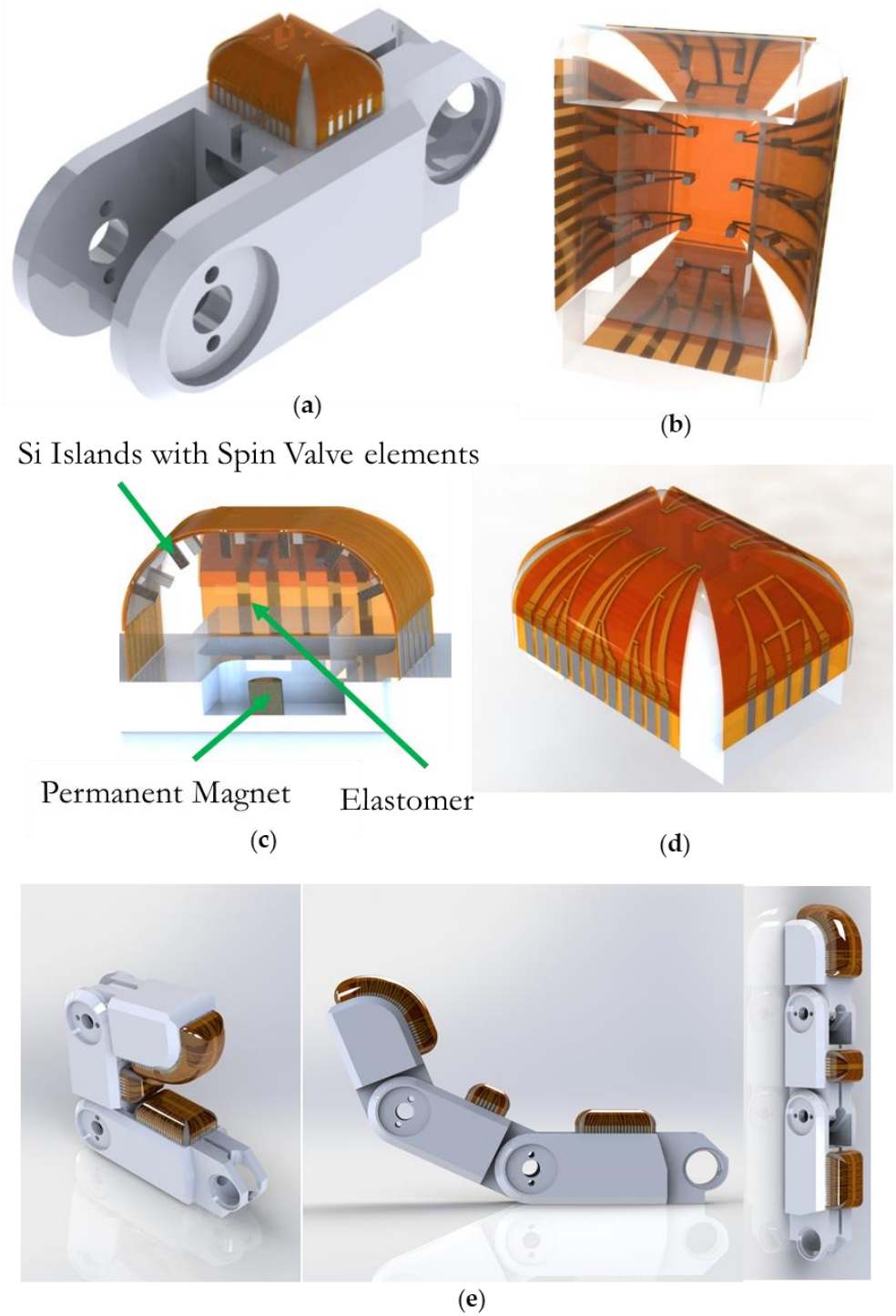

Figure 33. Images of the Flexible Hybrid Device and Electronic Interface Integration on the mid phalange of the Finger: a) Flexible Hybrid Device in perspective showing the flex connection pads and the 16 Si islands on top b) CAD Bottom View of the Flexible Hybrid Device c) CAD Cross section of the device in a, showing the island distribution (d) detailed on the Flexible hybrid device (e) shown design for the all the phalanges using the flexibly hybrid device concept.

3.6.2 Process

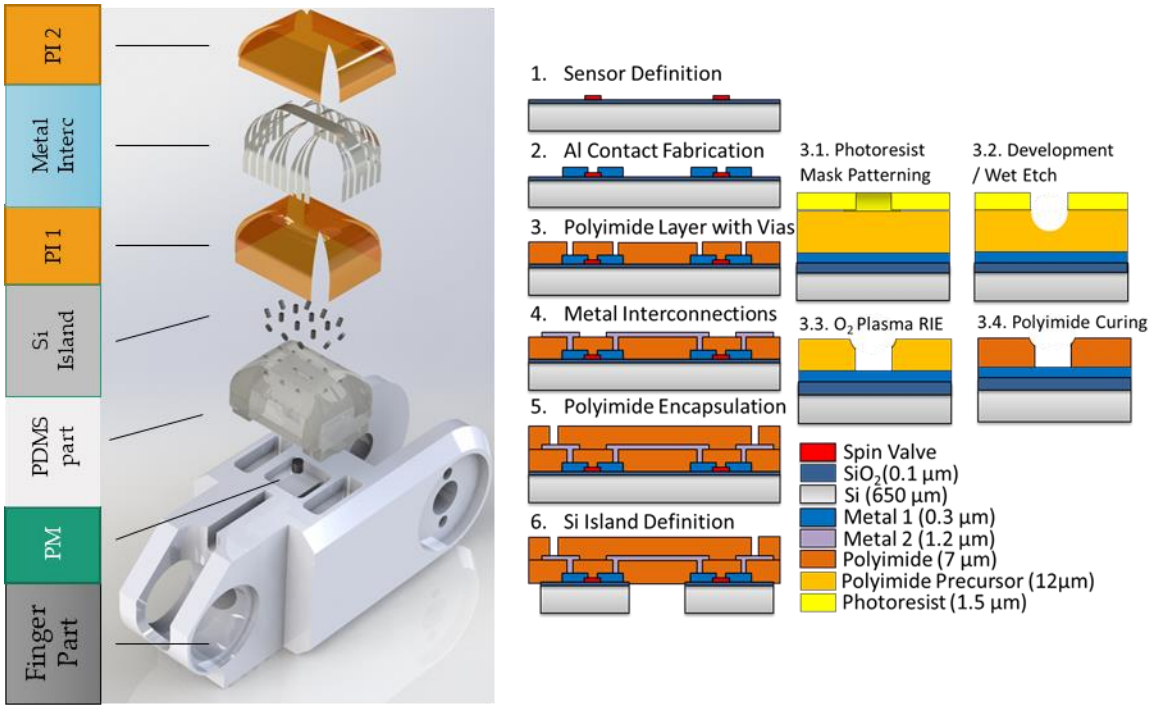

Figure 34. (a) Exploded view of the device identifying each layer and component. (b) fabrication process overview of the flexible hybrid devices, detailing the polyimide via definition.

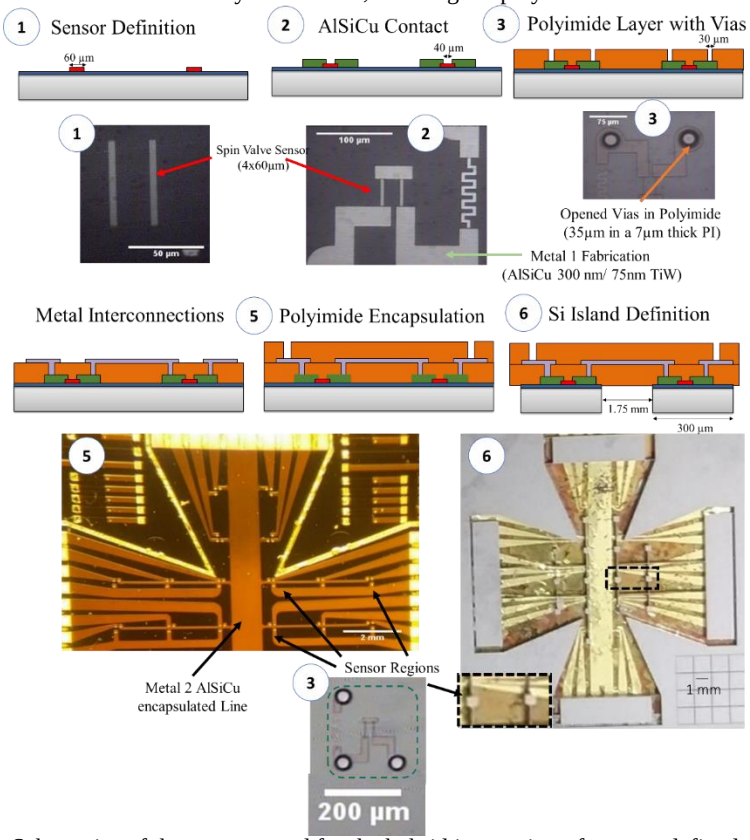

Figure 35. Schematics of the process used for the hybrid integration of sensors defined on silicon substrates (1-2) with metal interconnections embedded in flexible polyimide (4-5) including wet etch process for polyimide via opening (3) and finally defining individual islands on the silicon rigid substrate (6).

The spin valve elements are deposited by Ion beam sputtering in a Nordiko 3000 tool [23]. To obtain a linear response from the sensor, the rectangular spin-valve elements were defined by direct-write laser lithography (DWL2.0 Heidelberg, 405 nm wavelength diode laser) followed by ion milling (Nordiko 3600 tool, using a 0.16 A/cm2Ar+ beam).

The metal contacts consist of 300 nm thick $Al_{98.6}$ $Si_{1.0}$ $Cu_{0.4}$ film deposited by sputtering in a Nordiko 7000 tool (2 kW, 50 sccm Argon and 3.0 mTorr), capped by 15 nm TiW film to prevent oxidation and patterned by laser lithography and defined by lift-off.

The polyimide process is deposited by spin coating and the via definition and curing is process further detailed in section 3.6.2.2. The metal interconnections consist of 1.2µm thick $Al_{98.6}$ $Si_{1.0}$ $Cu_{0.4}$ film deposited by sputtering in a Nordiko 7000 tool (0.5 kW, 50 sccm Argon and 3.0 mTorr), capped by 15 nm TiW film to prevent oxidation. This film was patterned by laser lithography and defined by an initial Ion Milling step to remove the TiW layer and then a wet etch using TechniEtch Al 80 UN3265 to define 1.2µm thick $Al_{98.6}$ $Si_{1.0}$ $Cu_{0.4}$.

To define the Si Island, first a layer of SiO_2 1000 nm was deposited to serve as a hard mask for Si islands. The definition was performed at INL using a Deep Reactive Ion Etch (LPX Pegasus ASE) to etch the Si on the backside of the sample.

3.6.2.1 Sensor definition

The sensors used are deposited at INESC-MN using a stack that had to have thermal stability to sustain a 325 ^{o}C for 1h for the polyimide curing process and still have a linear range of -1 to 1mT. We used the coulomb approach to estimate a linear range of -1 to 1mT to be sufficient for these distances and expected displacements. The tactile system needs to have analog-digital interface to communicate the sensor analog signal to the digital processor in the robot. A description of this board comprising an ADC, a Voltage regulator, and Amp-OP is further detailed in section 3.6.3. The electrical characteristics for this device require a resistance of 300 Ohm to balance the resistor divisor.

We used the setup available at INESC-MN to measure the magnetoresistive transfer curves. The sensor consists of a top-pinned spin-valve sensor microfabricated on top of a Si wafer, with the following stack (thickness in nm): Si/SiO2 150 / NiFeCr5 /NiFe2.8 /CoFe2.2 /Cu2.2 /CoFe3 /Ru8 /CoFe2.6 /NiFe0.7 /MnNi30 /NiFeCr3 and fabricated as described in the process section. The rectangular geometry allows us to tailor the electrical and magnetic responses by changing the h x w µm2. The linearization strategies are well understood and explained [34], however each stack has its own performance so in **Figure 36** we show the electrical magnetic characteristics of the patterned devices in Si/SiO2 substrates. The larger the h the more sensitive it is and the larger the Rmin the larger the µV/mT output. To maximize the output we chose the 4x40µm structure.

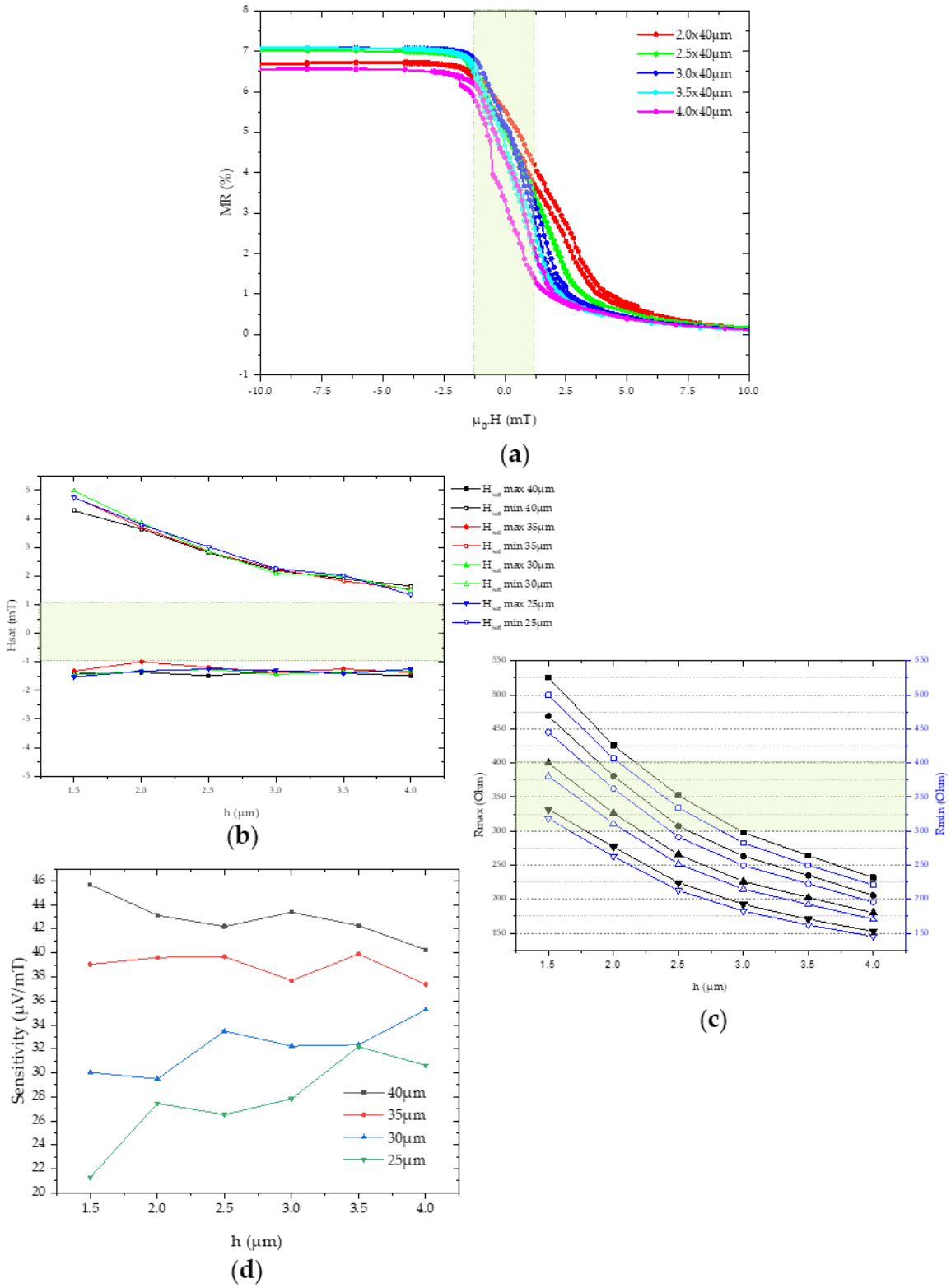

Figure 36. Information regarding the magnetotransport curve MR(H) with dimensions of h from 1.5 to 4µm and length of 25 to 40µm (a) transfer-curve only for the length 40µm (b) resistance of spin-valve elements (c) Maximum and minimum saturation field (d) sensitivity in µT/mV

3.6.2.2 Polyimide Vias definition

A polyimide layer covers the sensor contacts (**Figure 37** (3)) with vias to connect the metal interconnection to the Si island. Usually, polyimide microfabrication requires masks defined by photolithography and then transferred with wet or dry plasma etch. Figure 2 summarizes the methodology reported via definition in polyimide films. The most common polyimide pattern transfer processes described in the literature are the wet, dry and photosensitive polyimide (PS PI).

The wet etch process of polyimide films is chosen for its low cost and simplicity and in processes where aspect ratio (thickness/width) is not critical. Polyimide films can be wet etched in the same step as the photoresist development because the polyimide precursor is soluble in the photoresist developer, a TMAOH solution. The wet etch is an isotropic process that results in a round profile (**Figure 37** (6)). The aspect ratio is highly dependent on the baking condition, thickness, feature shape, and used chemicals. Nevertheless, when compared to Dry etch, its low aspect ratio prevents the high density of structures. Also, the residues left after etching can lead to incomplete via opening (Step 6), which results in higher resistance of the metallic contact.

Dry etching processes, such as plasma etching, most used are Reactive Ion Etch processes with CF_4, SF_6, CHF_3, or O_2 obtaining steeper and higher aspect ratio profiles than wet etch (**Figure 37** (8)). These gases have a 1:1 selectivity between Polyimide and Photoresist, thus it is common to have a hard mask (usually Al) deposited (**Figure 37** (3)), which has a low etching material enabling the fabrication of high aspect ratio features [46]. However, it requires the deposition (**Figure 37** (3)), definition (**Figure 37** (7)), and removal (**Figure 37** (9)) of the hard mask as additional steps.

The PS PI is the most expensive, and light absorbance brings an additional challenge when patterning film over 10 µm, thus high energy density lasers (over 1 J/cm^2) and characteristic wavelength over 400 nm are required [47].

Here we propose a process that uses both dry and wet processes. The wet etch process uses a photoresist mask to transfer the pattern, and the etch is stopped before the polyimide layer is completely etched (**Figure 37** 6)). Next, a dry etch step is used to open the via and remove the photoresist mask simultaneously. The proposed process has the same number of steps as the wet etch and comparable costs while being expected to improve the aspect ratio by finishing the via opening with dry etch.

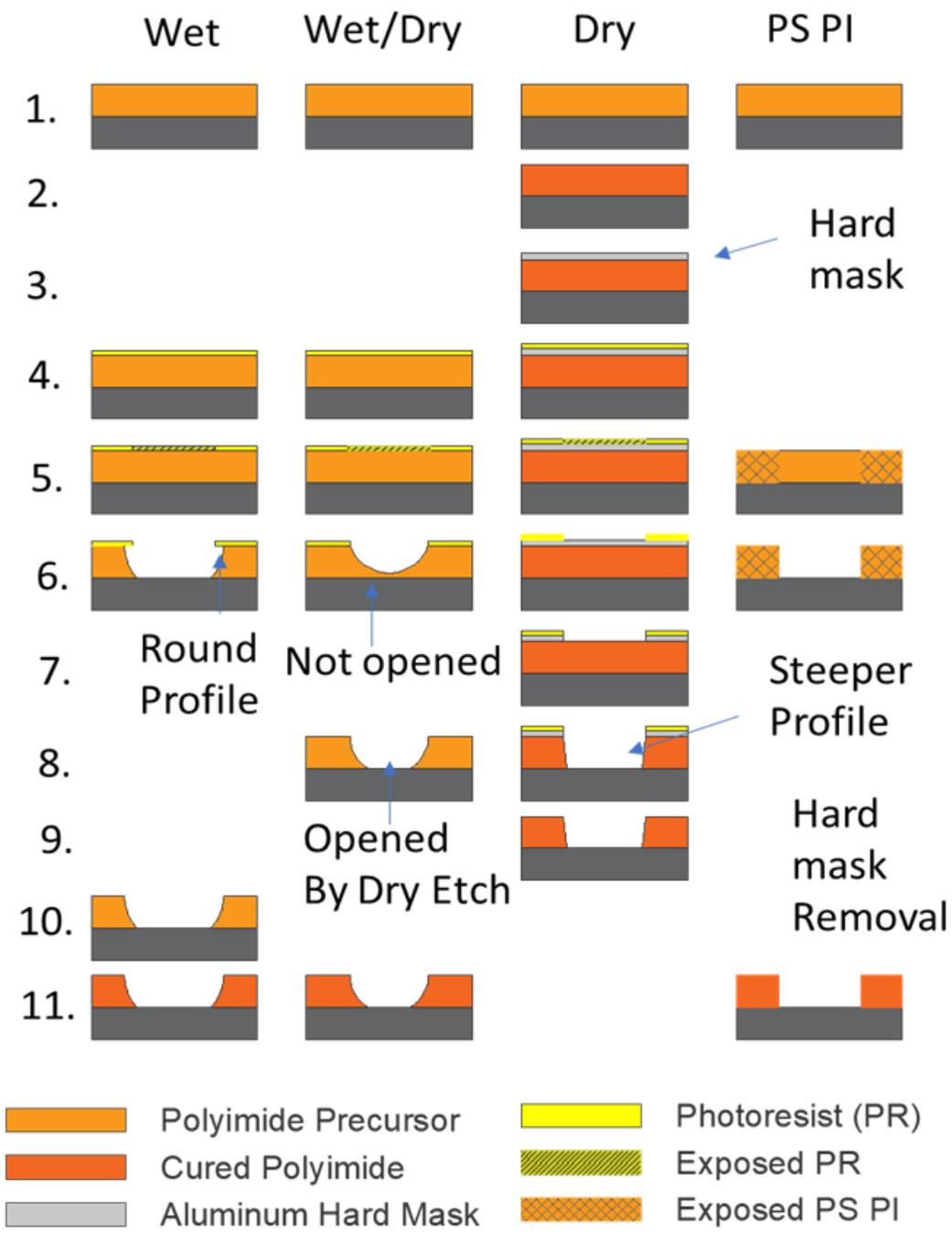

Figure 37. Process schematics for approaches usually used for via definition through a polyimide layer: Wet etching, combination Wet/dry etching, dry etching or photosensitive polyimide, combining several process steps listed from 1 to 11: 1. Polyimide spin coating; 2. Curing; 3. Deposition of the mask layer; 4. Photoresist coating; 5. Exposure; 6. Development; 7. Etch Mask; 8. Etch polyimide; 9. Remove mask; 10. Remove photoresist; 11. Curing.

3.6.2.2.1 Wet/Dry Process

A 10 µm thick Polyimide precursor layer is obtained by spin coating on a standard 6-inch silicon wafer-(SVG track equipment) at 3000 rpm for 30 s, followed by consecutive soft baking for 60 seconds at 87 ºC and then 120 seconds at 150 ºC to remove the solvents (**Figure 37** (1)). A layer of HDMS (YES VaporPriming system) is needed to improve the adhesion of the Polyimide. This yields a 5 µm layer thickness and the process is repeated to achieve a 10µm layer thickness. The high viscosity of Polyimide creates and edge of non-uniform thickness (edge exclusion) of around 5 mm on a 150mm diameter wafer.

Direct laser lithography (DWL Lasarray 2.0, wavelength = 417 nm) was used to define vias with 20 to 50 µm, using a 1.45µm thick photoresist mask (PFR7790 obtained by spin coating for 30s at 2500 rpm and baked at 87 ºC) (Steps 4 and 5 **Figure 37**).

After exposure, the developer used is TMAOH based (TMA238WA) and is used to perform both the photoresist development and the polyimide wet etch. Water is used to rinse the wafer at the end of the process (Step 6 **Figure 37**). The wet etch etching rate of the polyimide was found to be 0.4 ± 0.1 µm/s and is highly dependent on the soft bake conditions.

A LAM equipment was used to make the Dry etch step. The dry etch was perform using a pure O_2. plasma made with 20sccm O_2 with 200W and 275mT where the wafer is 1.3cm from the plasma source (Step 8 **Figure 37**).

The values found for the etch rates for the PhotoResist and polyimide precursor were 6.4 ±0.7 nm/s and 5.7 ± 0.8 nm/s, which equals to a selectivity of 1 to 1.

In **Figure 38** b) the evolution of the via diameter and width is plotted against the process time to understand the evolution of each parameter within the process phase. In the wet etch phase an increase in the via diameter is observed, while on the dry etch this value is constant. However, the via depth increases until a stable value during the wet etch phase while it decreases during the dry etch.

As the layer selectivity between the etching layer and the mask is 1:1 the ideal situation is when one has the same thickness of the via to be opened as the same thickness of the mask, thus both the via and the masking layer removal steps will be done at the same time. The photoresist mask used has a 1.45 µm thickness which is completely removed using a 400s dry etch step. In **Figure 38** the graph where the via depth is plotted against the processed time one can observe that during the wet etch the depth increases until 30s of wet etch and is then stable after this point (polyimide layer/photoresist layer increase during the wet etch step up to 11 µm), indicating the layer has been fully etch.

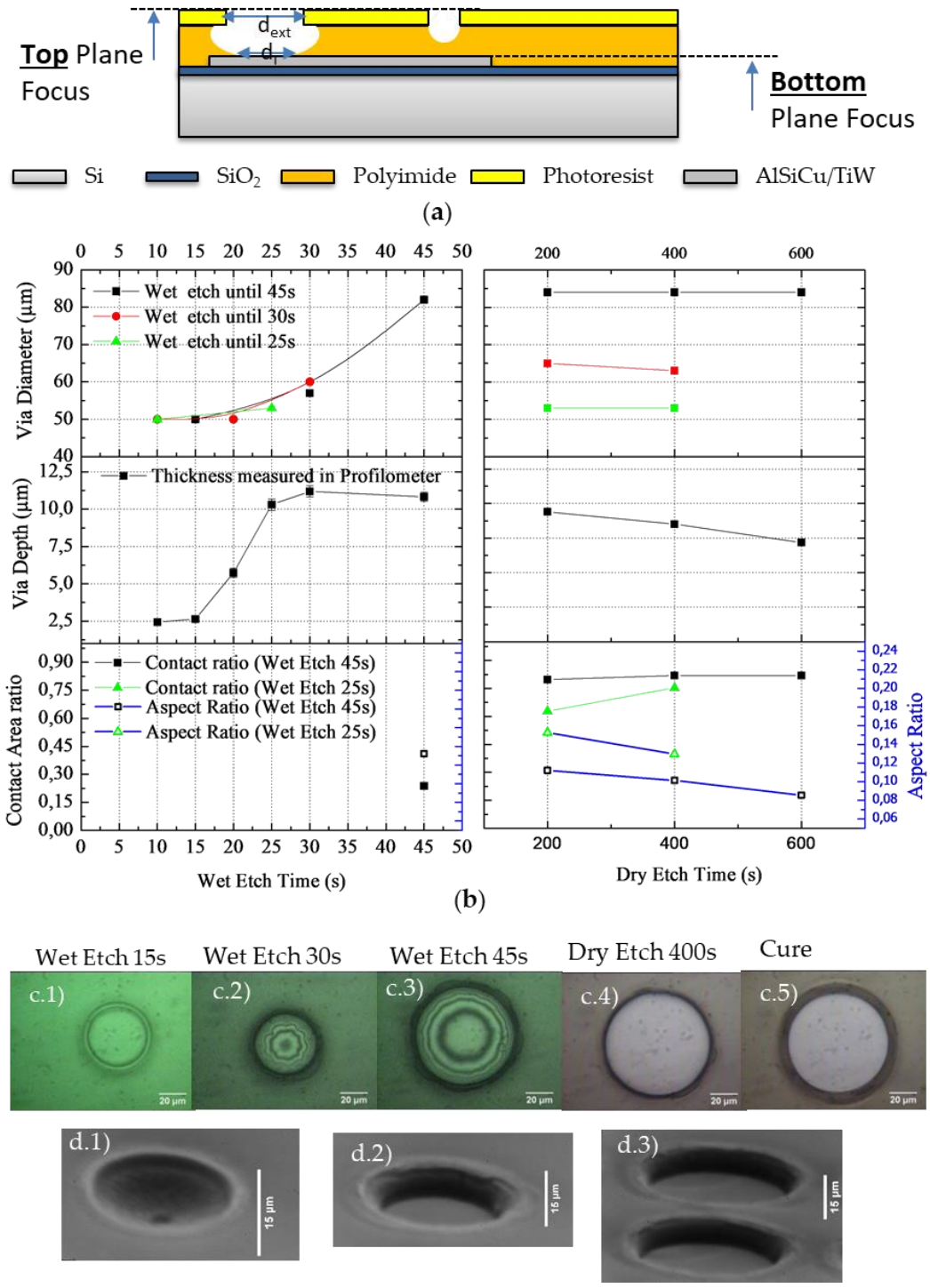

Figure 38. a) Schematic of the process step and measuring methodology b) Evolution of the Vias diameter, depth contact area and aspect ratio both for the Wet Etch and Dry Etch steps. (Right) c) Pictures from top view using an Optical Microscope that document the evolution of the via size and contact area for the wet etch and dry etch steps and d) SEM pictures of the vias after Dry Etch with d.1) 10, d.2) 20 and d.3) 30 µm.

Figure 38 c.1) to c.5), a top view of the via with an optical microscope shows the via formation during the wet and dry process. In **Figure 38**c.1) and c.2) after 15s and 30s, respectively, the wet etch process did not fully opened the via as some residues can be observed in centre of the via. Comparing **Figure 38** c.4) to c.5) one observes that the residues from the via have been removed and the via diameter has remained constant. The curing process had no effect on the via diameter but did decrease the layer thickness by 30%.

Reducing the Wet Etch time before the via was opened was key to avoid the increase of the via diameter. In the sample that was subjected to a 45 second Wet Etch the via increased its diameter up to 84 µm while the opened area was only a 40 µm circle. Using Dry Etch on this sample increased not only the contact area without increasing the via diameter any further. The via depth stabilizes in 11 µm after 30s for the 50µm vias. For smaller vias the via depth is lower. This process obtained a via with a 0.125 aspect ratio and a contact area of 82%.

Samples where the Wet Etch was stopped at 25 and 30 seconds had a better diameter control while still opening the via. For the 25 seconds sample a 53 µm via was obtained with an aspect ratio of 0.2 (1.6 times higher) and a contact area of 75%. The decrease in contact area is due to the side wall profile which is steeper for a higher time of wet etch due to the undercut.

In **Figure 38** d) vias with 10, 20 and 30 µm are observed in SEM and the slope of the via wall is found to be decreasing which is favourable deposition of the Metal 2.

3.6.2.3 Aluminium deposition on the Polyimide

The resistivity of the Al film deposited on the SiO_2 and on the Polyimide was found to be 2 to 4 times lower. The thicknesses deposited were 0.3 µm on SiO2 for connection between the Si Islands, while the AlSiCu contact deposited on the PI was 1.2 µm. The higher resistivity on the Polyimide could is most likely related to a higher roughness of the layer and/or film strains. The change in roughness is observable in the microscope, just due to different Dry Etch times. For 200s of Dry etch a large roughness is optically visible, mainly due to photoresist residues that are burned after the 30min at 200 ºC for polyimide curing. For 600s we can also see a significant roughness, this time caused by the plasma.

Table 5 – AlSiCu magnetron sputtered films resistivity on different substrates.

Substrate	Thin Film	Resistivity (µΩ.cm)
Glass	0.3 µm Al	5.36
Glass	1.2 µm Al	5.45
SiO2	0.3 µm Al	3.46
Polyimide	1.2 µm Al	14.65

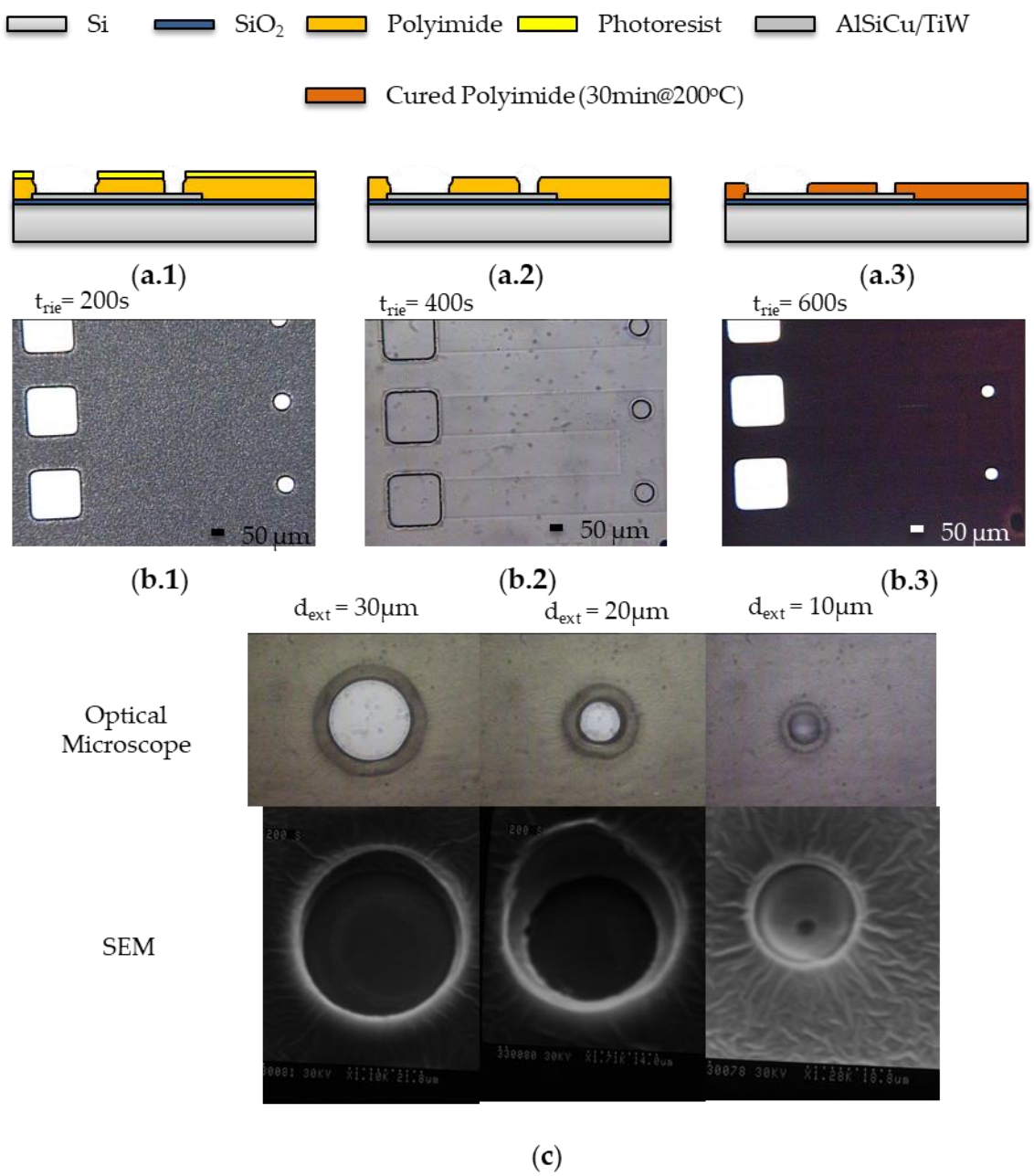

Figure 39. a) Schematic of the process step for a.1) wet etch a.2) dry etch a.3) curing process.b) oprtical microscope showing the roughness of the aluminum layer for a dry etch time of b.1) 200s; b.2) 400s and b.3) 600s. c) Pictures from top view using an Optical Microscope and SEM for vias with 10, 20, 30 µm.

The via resistance values was determined with 4-probe measurement using the test structures represented in Figure 4. The model assumed for the via resistance determination was a series of 3 resistors, corresponding to the via (R_{via}) bottom (R_{bot}) and top contact (R_{top}) resistance. The resistance determined for the vias was 0.3 Ω, which is 1000 times smaller than the Resistance of the Spin Valve element (R_{sv}). As expected, the resistance is increasing linearly with the decrease of the via diameter. The value dispersion is most likely related to the diameter dispersion of the vias.

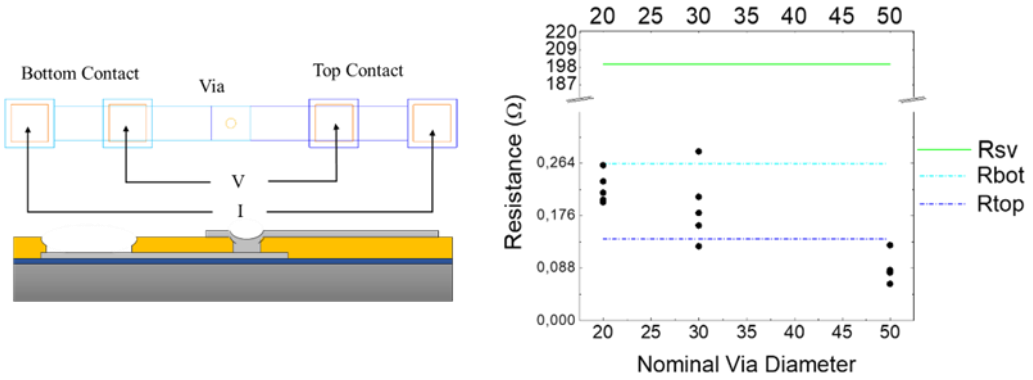

Figure 40. (Left) Measurement and electrical model schematics. (Right) Via Resistance plotted against the Nominal Via Diameter.

3.6.2.4 Sensor Output

The magnetoresistive sensors patterned with this hybrid process are shown in **Figure 40**. The hybrid process aims to define sensor regions, shown in **Figure 35**, and connect them with flexible interconnections. The region as a unit is replicated in a matrix-like display. As only the sensor regions are supposed to be in Silicon in the final device, all the required interconnections are done in Polyimide, such as the Sensor Output, Voltage Input and Ground.

The total channel resistance of a spin valve can be divided into a geometrical sensor resistance and a contact resistance, composed of the lead resistance and the interfacial resistance between the lead and the spin valve element.

The spin valve sensors were patterned in a 4 x 60 μm^2 (see **Figure 35**). The contacts overlap 10µm on each side of the spin valve leaving the sensor with an active area of 4x40μm^2. The contact area between the spin valve and the contact lead is 90μm^2, which is considerably large. This outputs a negligible resistance due to the contact.

The only resistance that could affect the sensor output is the R_{lead}, which depends on the geometry of the contact lead. To understand whether their resistance affect the signal, the sensor output with polyimide vias (**Figure 40** Black) and without polyimide vias (**Figure 40** Red) were measured and compared.

A higher Magnetoresistance is observed for the Sensors Output deposited in SiO_2, due to lower substrate roughness. The linearization and lower offset field (Hf) are a consequence of the Demagnetizing Field produced by the patterning of the Spin Valve Sensor. No MR losses were observed in the spin valve measured with the PI vias in series. However, the voltage output shows a higher resistance is observed in the curve with the PI vias in series a rough 5 Ω offset.

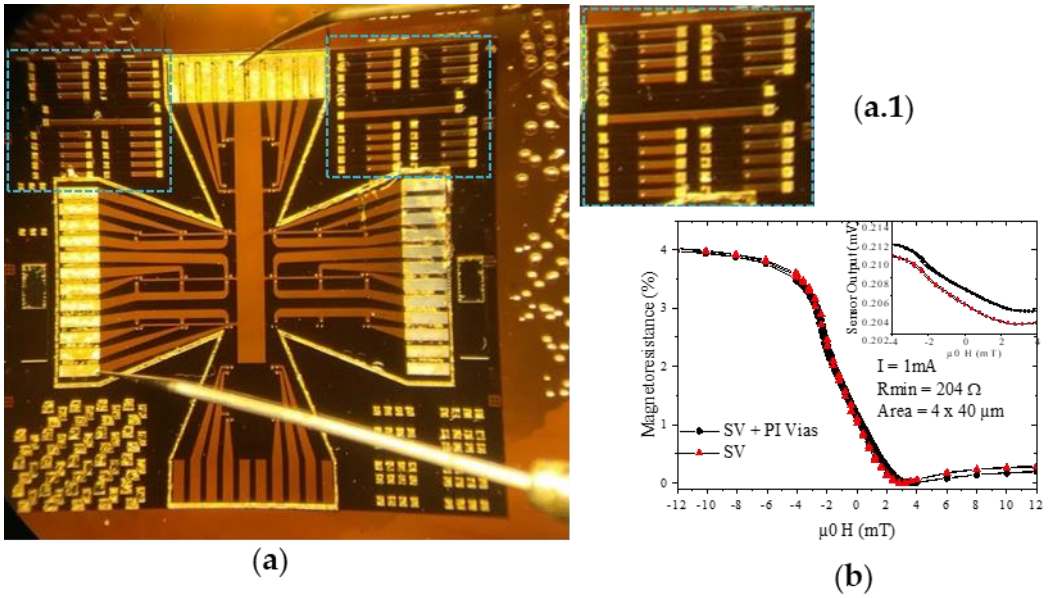

Figure 41. (a) Final annealed device showing the probes measuring a sensor (a.1) detail on the testing structures for vias characterization (b) Magneto transport curve of the same stack in SiO2 (Black and Red) annealed for 1 hour at 325 ºC (inset) Both SV + PI vias and only SV are plotted against their voltage output.

After the polyimide encapsulation, we show that the polyimide vias and the aluminium contacts are not affecting the sensor's performance, considering the necessary curing process. Combining Wet and Dry etching to opens vias in polyimide increased both the area of contact and aspect ratio of the vias, thereby supporting that this polyimide via process is suitable for INESC/MN Cleanroom and compatible with the existing GMR fabrication process.

3.6.2.5 Si Island Definition

A layer of SiO2 1000 nm was deposited on the backside to serve as a hard mask to define the Si Island. On the front side **Figure 42** (a), the polyimide layer viscosity created an uneven pattern on the edge of the sample. This increased difficulty to align the backside with the front side as the sample was uneven when it had the backside up. To align the corner was used (**Figure 42** (b)), but this approach can be prone to significant misalignments. The Si Island hard mask was defined using the Direct Write Laser system (Heidelberg DWL 2000) available at INL, and then by defining SiO2 hard mask using Reactive Ion Etching **Figure 42** (d). Finally, a total of 78 min of Deep Reactive Ion Etch (LPX Pegasus ASE) used for the Si Island definition **Figure 42** (c).

The main challenges for this last step were the temperature increase due to the 78 min of Deep Reactive Ion Etch, which generated not only significant thermal stresses as well as mechanical. To mitigate the thermal stresses and improve the sample cooling rate a highly thermally conductive wax was placed between the sample and the support wafer. While to mitigate the mechanical stresses due to the high flows of the DRIE plasma the Si Island mask was design to have small connections between the Si islands to prevent them from being removed. The thermal issues required us to remove the sample manually as **Figure 42** (e) shows. The solution of bridges between Si Islands proved to be sufficient

even though some of the bridges themselves were not completely removed (see detail in .

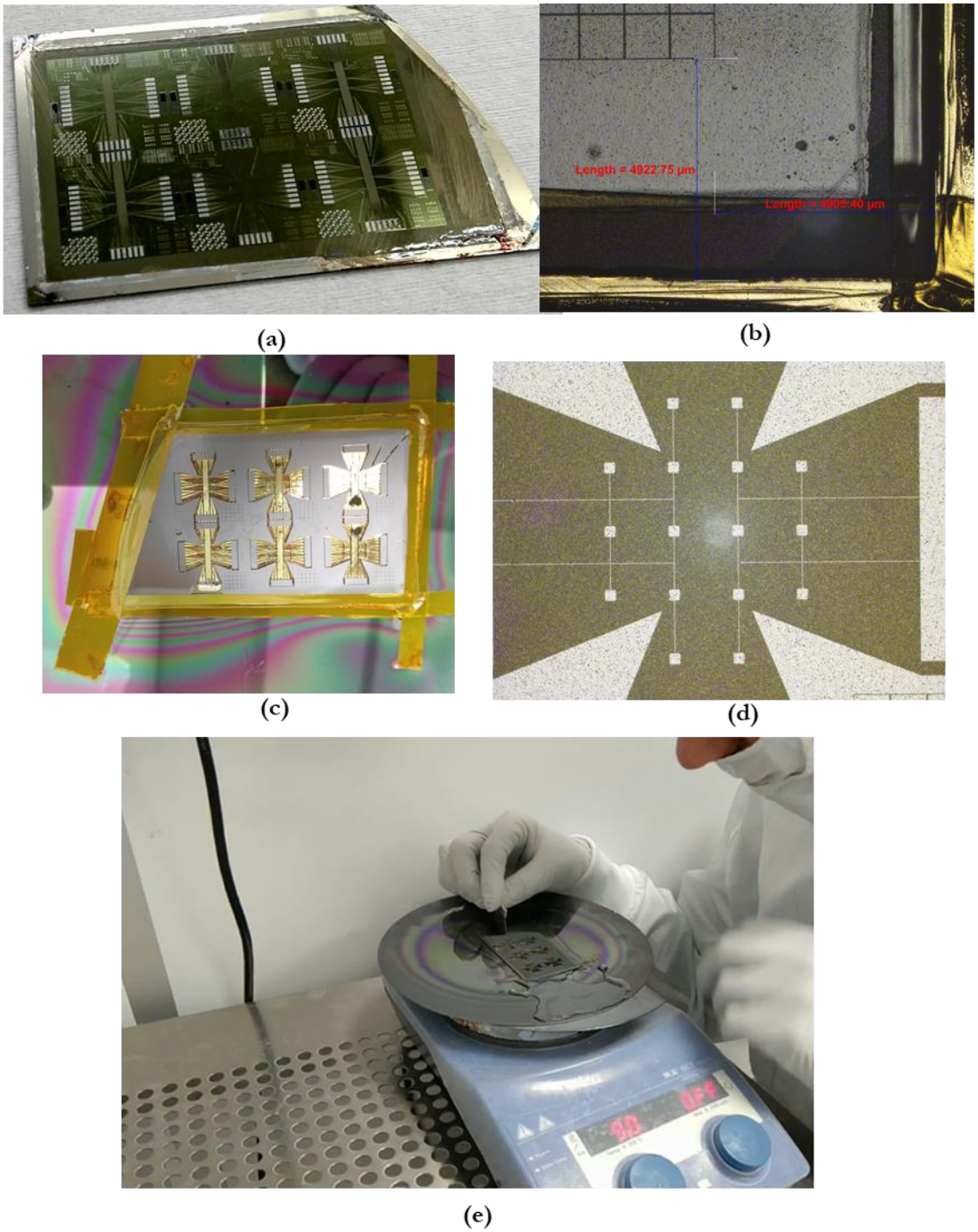

Figure 42. (a) Front side, showing the six dies of the FHD_02 design. (b) backside alignment measurements. (c) Backside after etching (d) Backside definition after SiO2 hard mask definition (e) manual removal of the Si support wafer.

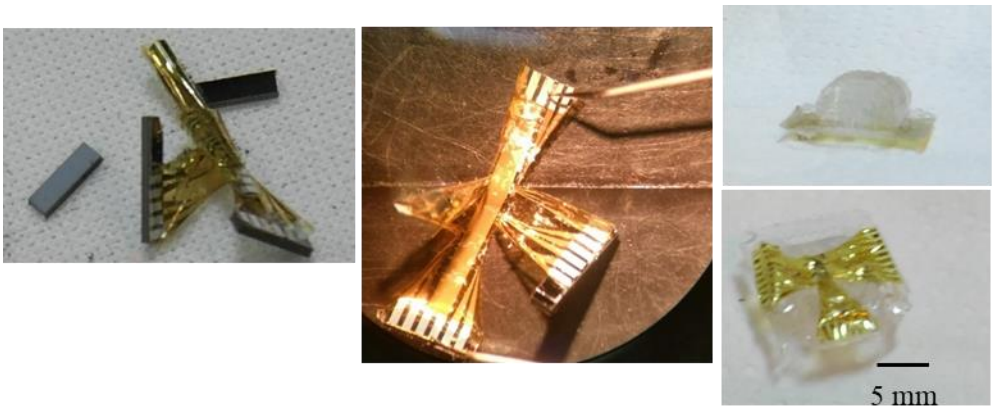

Figure 43 – (left) Final device after Si island definition showing the Polyimide rolled on itself detaching from the Si. (centre) electrical measurements; (right) Bottom view of the device after injection and side view of the sensor.

After defining the Si Islands and releasing it from the wafer the goal was to conform it to the shape, we required to fit the finger. The main issue with this approach were the film stresses tensions both from the AlSiCu layer and Polyimide. Despite this, we measured similar resistivity in the aluminum. Unfortunately, the complex shape of the device was neither helpful for handling nor conforming it to the expected shape as in the end, and it was not possible to have the desired design.

3.6.3 Electronic Interface

This electronic interface works by providing a low-noise voltage to two resistive elements in series, the spin valve (R2), and a resistor (R1). The electronic schematic is shown in **Figure 44** (d). The resistor division strategy relies on a pair of resistors to control the current bias that is applied to the sensor. This approach works because the spin valve resistance changes with the applied field, and so does the voltage bias in between the two resistors. The middle point and connect it to the amp-op and amplify it to the ADC. However, the ADC has a saturation voltage, and this measuring point cannot exceed that value. For applications where the DC value is relevant, as this one, it significantly limits the amplification range. To obtain the values, we simulated in SPICE and calculated that the resistor had to have a 2.5k Ohm (R1) and the sensor a 300 Ohm resistance (R2), this would allow us to amplify about 10x the sensor signal and have a voltage change in the ADC 3.5 to 3.7 V. To minimize the noise, low noise amplification and a voltage regulator were chosen to be used in the board.

A flexible printed circuit board (FPC) process was developed for another project and was used to fabricate these electronic boards. The steps used for mounting this electronics board (see **Figure 44**) are, its fabrication (see **Figure 44** (a)), the placement of a silicon chip with the silicon chip (see **Figure 44** (b)) with the resistor-spinvalve pair and wire bonding it to the FPC and finally placing the electronics (see **Figure 44** (c)).

An improved version of this system was also pursued, where a 24-bit ADC, four low noise

amplifiers read 16 sensors, and a low pass filter to minimize the high-frequency noise.

Both designs had similar challenges as they both relied on similar principles. They both required the sensors to be wire bonded, which was a significant problem for integration due to wire bonding fragile connections. The other was the resistance-divisor strategy, which made it challenging to optimize for. It was also not obvious how to integrate this solution with FHD_02 in a modular way.

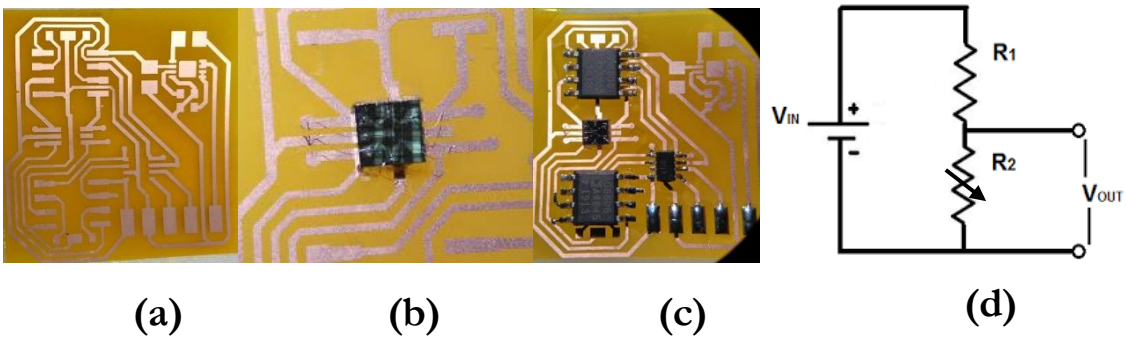

Figure 44. (a) FPC design after fabrication (b) Silicon Chip wire bonded to the electronic board (c) Soldering the main components of the board. (d) electrical schematic.

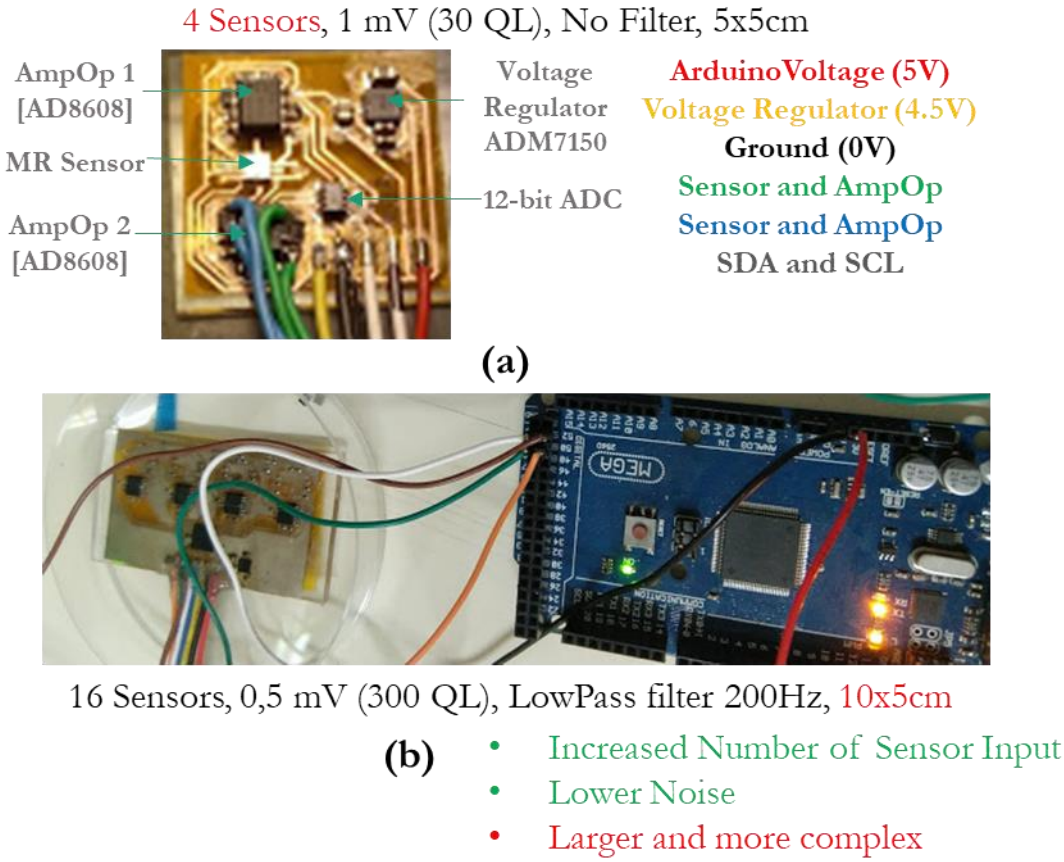

Figure 45. (a) Electronic interface 1st design (b) Electronic interface 2nd design.

3.7 Flexible Sensing Matrix #03

3.7.1 Design

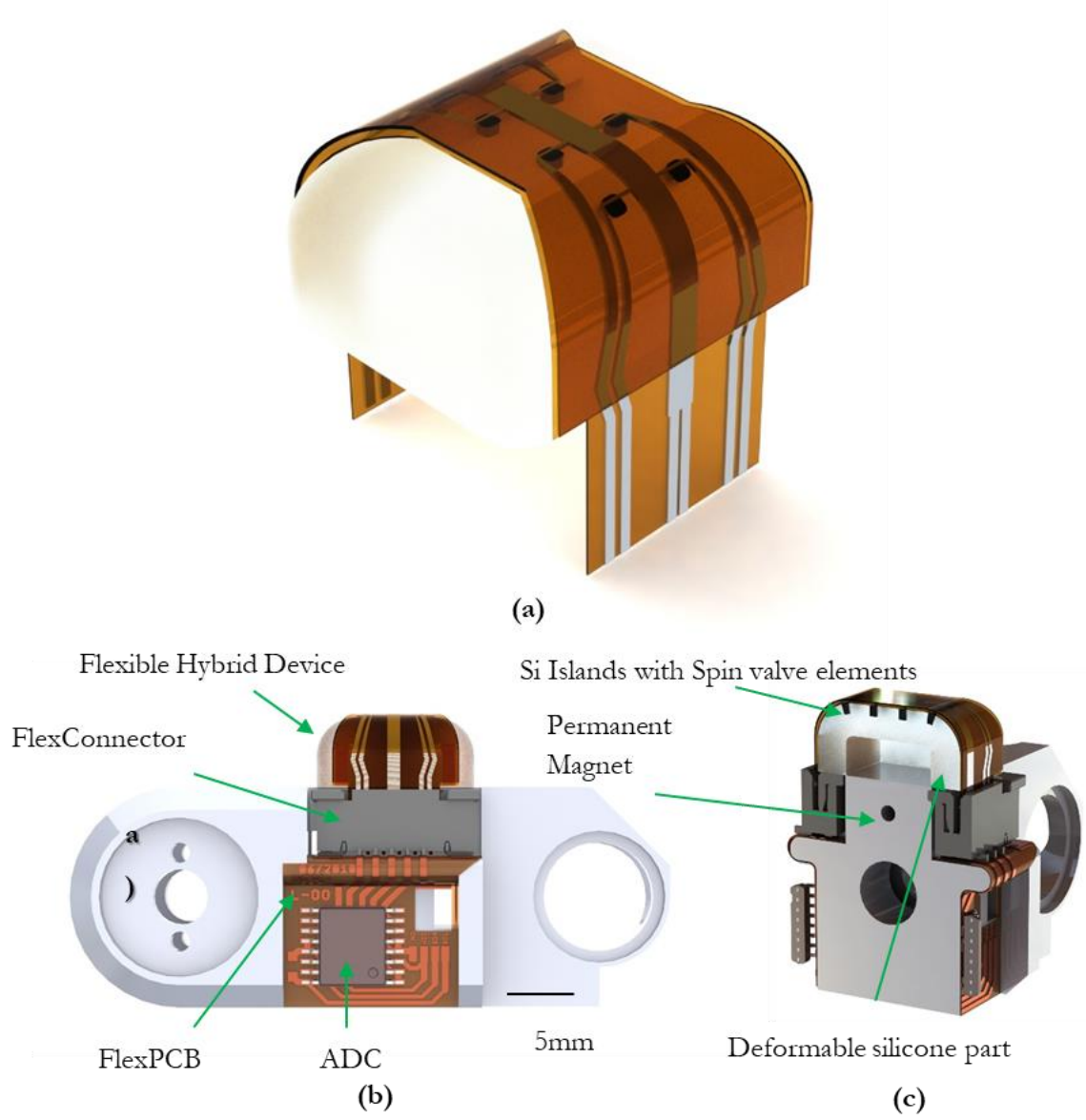

Figure 46. Images of the Flexible Hybrid Device and Electronic Interface Integration on the mid phalange of the Finger: a) Flexible Hybrid Device in perspective showing the flex connection pads and the 8 Si islands on top b) CAD Side View of the Flexible Hybrid Device and the Electronic Interface integration on the Finger CAD; c) CAD Cross section of the device in a, showing the island distribution and the electrical connections between the Flexible Hybrid Device and the Electronic interface.

3.7.2 Process

The main changes for this process were for the Si Island step with a lower degree of complexity in the design, lower number of islands, larger island sizes (500x500µm^2). Everything else was kept the same as **Figure 34** (b) and as described for FHD_02. In addition, a new electronic interface was developed to fit the robot finger geometry.

The change in electronics no longer required the fabrication of the resistor in series with the spin valve elements so they were removed, and the electronic components in the Si Island became easier to fabricate and less prone to error. It also helped to have less metallic interconnections to worry about as, per Si Island, only two connections are required as opposed to the three in FHD_02.

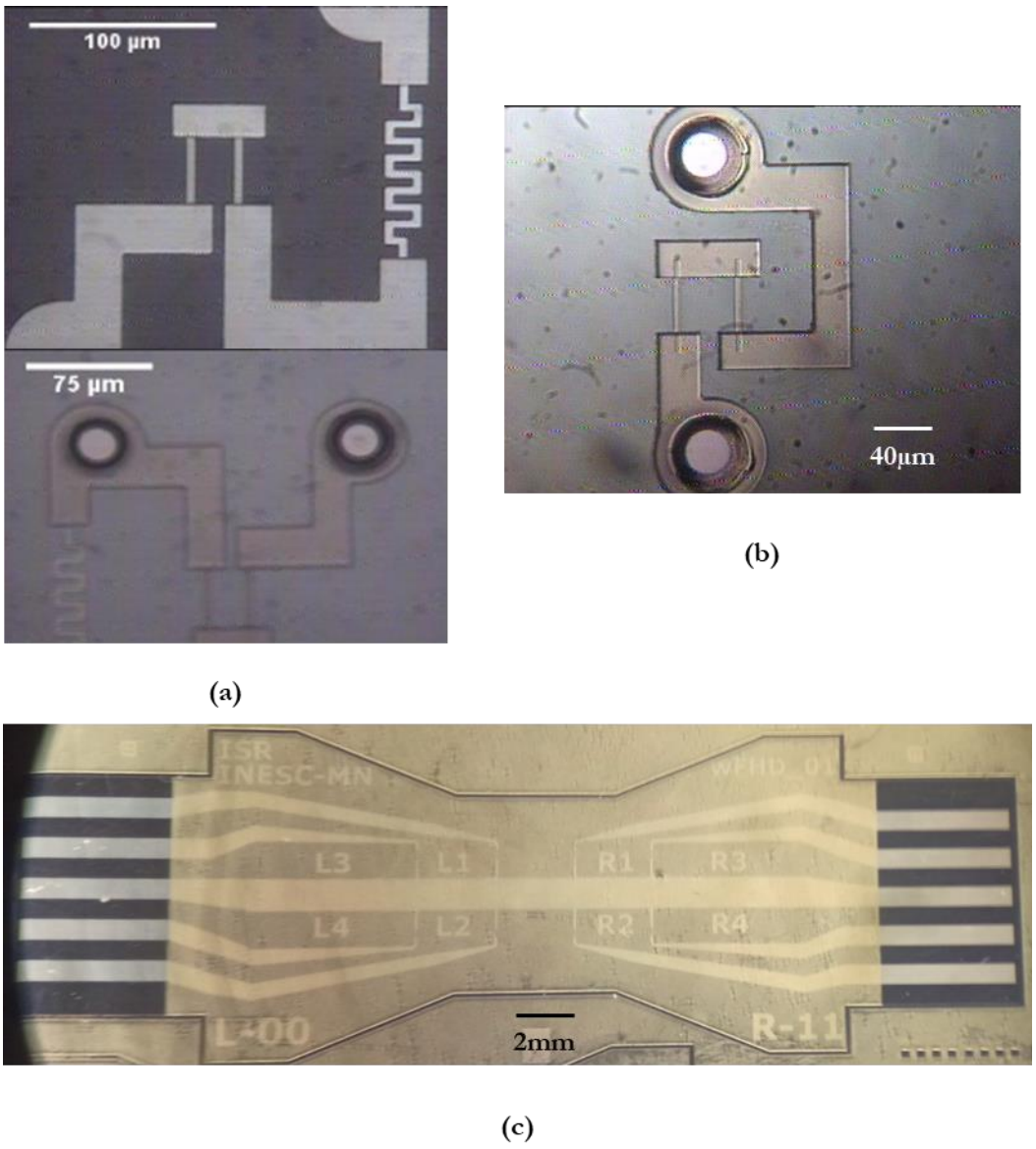

Figure 47. (a) FHD_02 electrical components: spin valve and resistor (b) FHD_03 electrical component spin valve and the two required polyimide vias.

With each iteration, we were able to reproduce the polyimide process consistently. By reducing the complexity of the design shape and increasing the Si island, we expect an easier integration. However, we did not follow through with the Si Island definition, mainly due to the long iteration times. To optimize the Si island definition and integration of these devices at the fingertip, we would require fast iteration cycles to improve our ability to conform these devices into the desired final shape.

3.8 Flexible Sensing Matrix #04

3.8.1 Design

At the same time, we developed a new process to integrate the Si Chips with GMR sensors on a flexible printed circuit board. This design has the exact dimensions as the previously described FHD_03, but enables much faster iteration cycles. We decided to test this process to push the devices to the testing phase as fast as possible. After some optimization, we were able to have a working prototype that we could test.

Besides developing a new electronic interface, we fabricate the Si Chips in parallel with the flexible interconnections. We design, fabricate and optimize the chips in iterations of 1 to 2 weeks, while in the previous case, we needed about six months to complete the process from start to finish. This achievement enabled us to test the molding and shaping process with much more frequency, finally obtaining a working prototype.

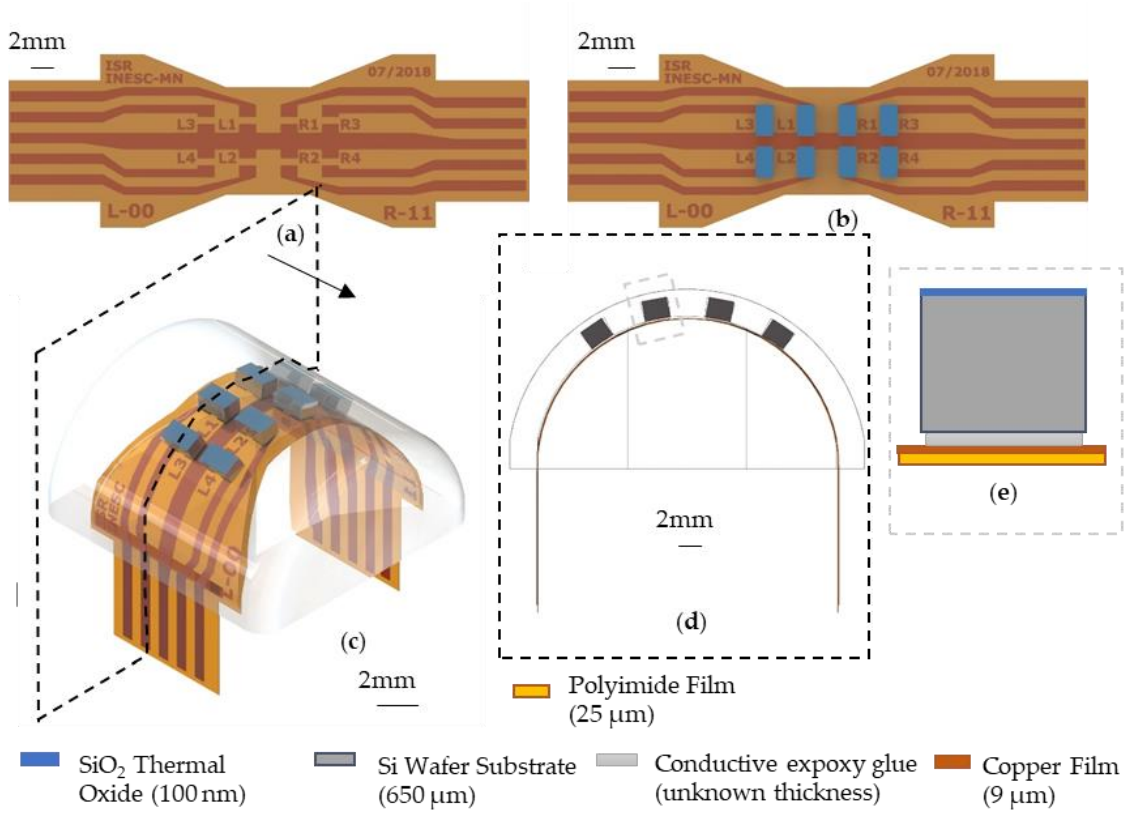

Figure 48. (a) Top view of the FPC, showing the Pads to connect the Si Chips; (b) Si Chip in the FPC using the epoxy glue; (c) 3D view of the FPC with the Si Chips embedded in the PDMS part. (d) Cross section of the device showing the curvature for the Flexible Sensing Matrix. (e) a zoom in on a Si Chip glued to the FPC.

3.8.2 Process

3.8.2.1 Rigid Si Chip

The magnetic sensor elements are fabricated in large wafers using industrial processing tools at INESC-MN, individualized using a DAD 321 dicing system to their final dimensions of 0.8x1.5 mm^2. After the dicing, the sensors are characterized individually and selected, as quality control measure, to secure the device performance across the eight chips in the sensing matrix. This process versatility is not available in printing or many other flexible technologies, which must rely on all the sensors to be viable in a matrix. The geometry for the sensors produced is shown in **Figure 49**.

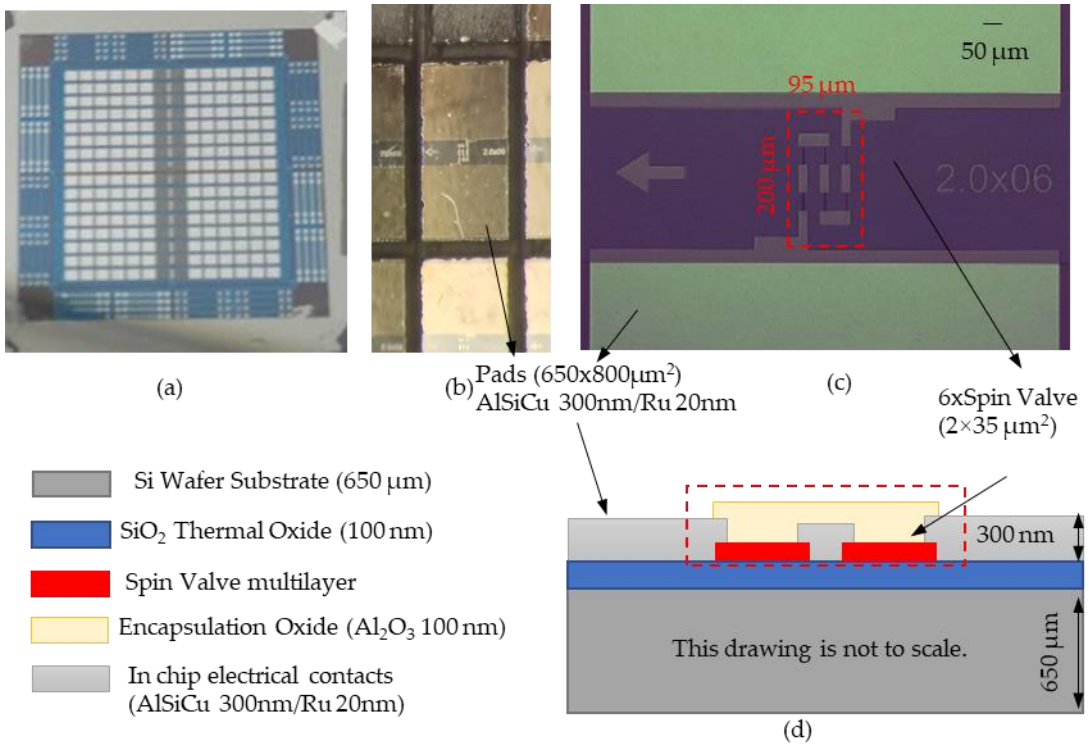

Figure 49. (a) 1x1 inch2 sample used for the Si chips fabrication (b) Si Chip after dicing process with 0.8x1.5 mm2 (b) Top view of the microfabricated 6 spin valve sensor in series, where each is a 2x35 µm2. The arrow to the left of the sensor series side indicates the sensitive direction of these. (c) cross-section schematic of the rigid Si chip

The sensing element consists of a top-pinned spin-valve sensor microfabricated on top of a Si wafer, with the following stack (thickness in nm): Si/SiO2 150/Ta 1/NiFe 2.8/CoFe 2.5/Cu 2.6/CoFe 2.3/MnIr 18/Ta 3 deposited by Ion beam sputtering in a Nordiko 3000 tool [48]. Notice that both sides of the wafer are coated with the same SiO2 thermal oxide to minimize leakage currents through the final device's substrate.

To obtain a linear response from the sensor, the rectangular 2 x 35 µm2 spin-valve elements were defined by direct-write laser lithography (DWL2.0 Heidelberg, 405 nm wavelength diode laser)

followed by ion milling (Nordiko 3600 tool, using a 0.16 A/cm2Ar+ beam). The metallic leads were patterned to connect 6 elements in series and therefore defining the sensor array. The metal contacts consists of 300 nm thick Al98.6 Si1.0 Cu0.4 film deposited by sputtering in a Nordiko 7000 tool (2 kW, 50 sccm Argon and 3.0 mTorr), capped by 20 nm Ru film in Nordiko 3600 to improve electrical contact, patterned by laser lithography and defined by lift-off. Finally, the sensor chip surface was passivated with 150 nm Al2O3 layer deposited by magnetron sputtering, except over the contact pads, for further protecting the sensing elements of encapsulation.

3.8.2.2 Flexible Circuit Board

A flexible printed circuit cable (FPC) was fabricated using a laminated foil with 25µm thick Polyimide and 9 µm of copper, patterned by laser lithography and wet etch.

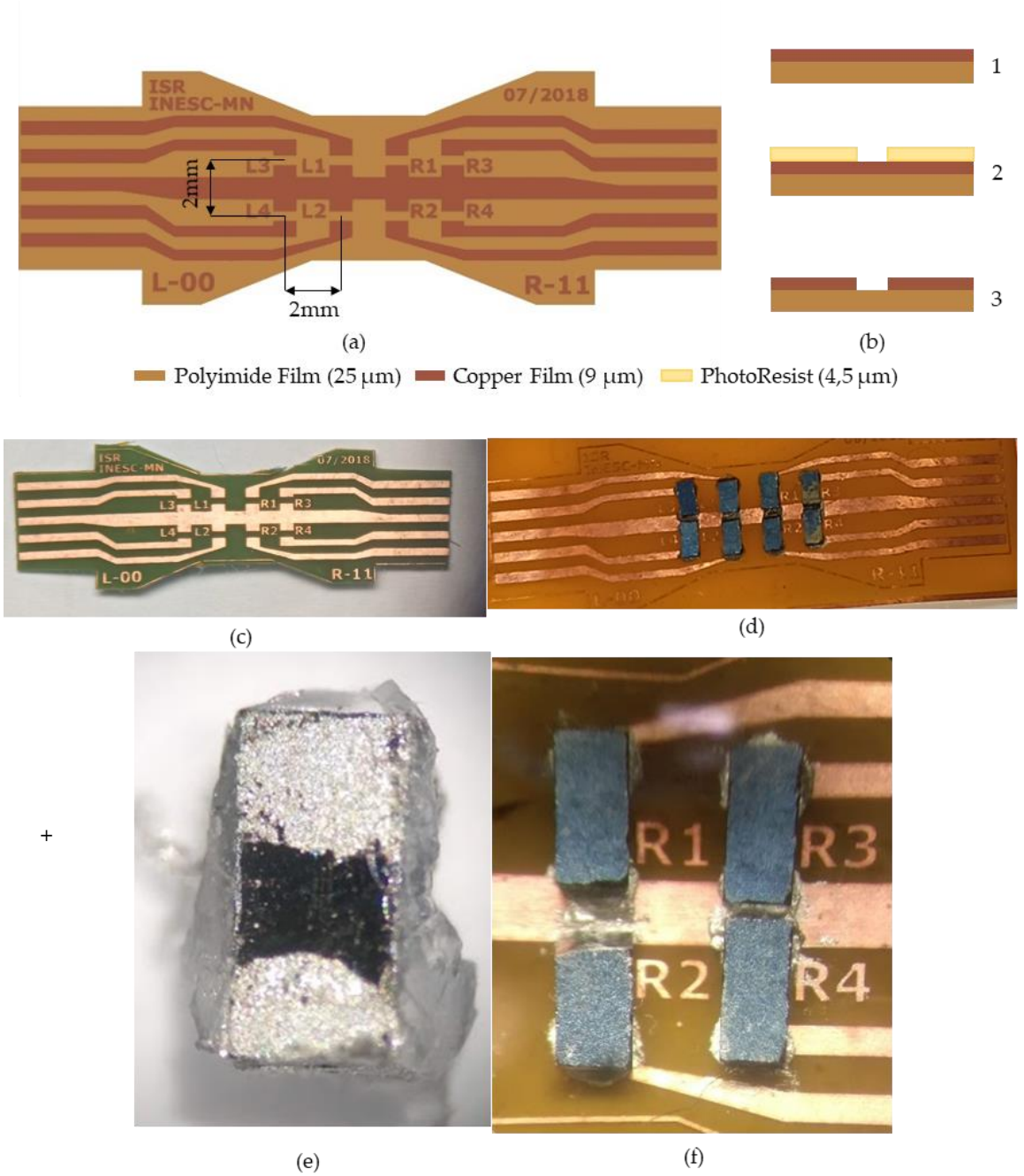

Figure 50. (a) Top view of the FPC, after defining the copper layer (b) microfabrication steps: 1. Bare copper/polyimide film cleaning; 2. Coating and definition of photoresist using lithography system; 3. Wet etch and resist stripping. (c) Fabricated FPC (d) FPC with Si Chips (e) Epoxy glue spreading pattern on a Si Chip from the bottom (f) Epoxy glue spreading pattern on a Si Chip from the top.

The FPC was designed fully cover the finger surface, the most straightforward way to achieve this is to connect the left and to the right side of the finger part with a "strip". The result is a FPC that

distributes 8 sensors in a 4x2 matrix with 2 mm in between. The distance is much lower than previously reported designs because we could fabricate them without packaging. Moreover, the mechanical flexibility allows us to conform the FPC to the finger surface shape resulting in mounting architecture shown in **Figure 48**.

The sensor chips were flipped and glued to the FPC using a silver conductive epoxy adhesive (MG Chemicals 8331). The main challenges of this step are the manual manipulation of the relatively small Si Chips as well as in the lack of an accurate epoxy volume control. The manual manipulation can lead to two main assembly errors: the distance between the sensor to be smaller or larger than the 2mm they were dimensioned to be; and a relative angle between them. The tested devices were assembled with a precision of ~200 μm, and angle errors under 10 degrees. A better epoxy volume could allow us to better understand the influence of thickness and mechanical and electrical quality of the contact.

3.8.2.3 Polymeric part

Finally, the FPC and the sensors are embedded in an elastomer cap, shaped with similar curvature as the FPC, and to protect it from the environment and provide the robot with better grasping. A Witbox 3D printer fabricated the mold using a PLA filament and a layer height of 0.2 mm. The FSM was attached to the molds, holding it in place while also serving as a casting mold for shaping the silicone cap. The curing of the polymer coincided with the FPC and polymer bonding. The elastomer used was PDMS (Polydimethylsiloxane) in a 1:15 proportion and cured at 70 ºC for 1 hour. This temperature does not affect the magnetoresistive sensor, demonstrating thermal stability up to 120ºC [49].

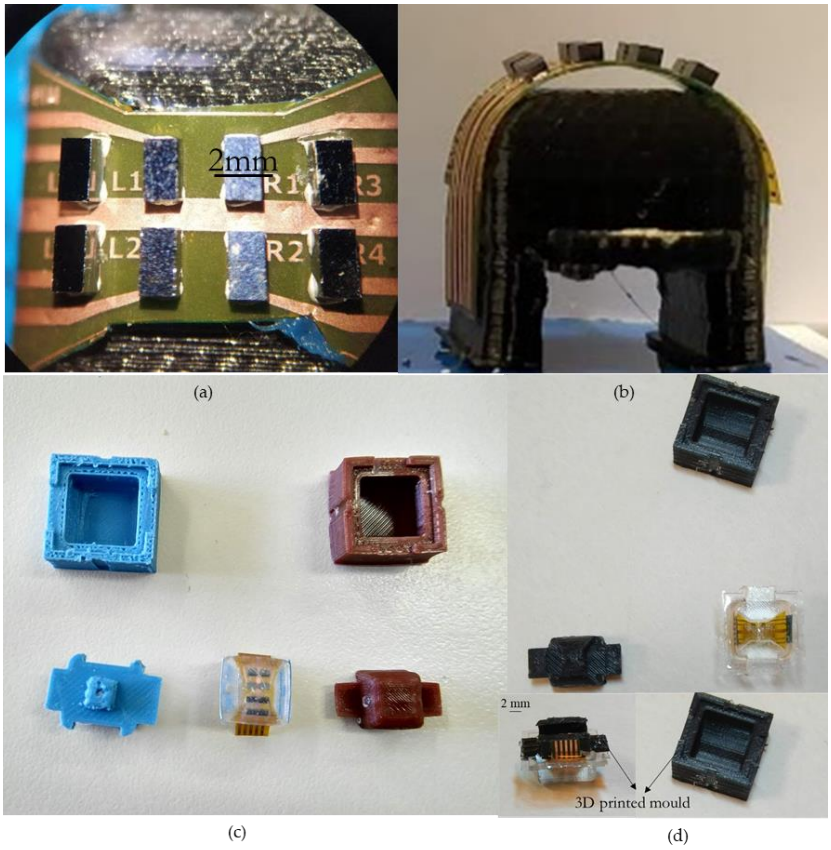

Figure 51. (a) The FPC is fixed to the part of the mold that defines the desired geometry for the flexible sensing matrix. (b) side view of the Si Chips and the FCP fixed to the mold part. (c) Old iterations of the mold, showing a design evolution on the process of fixing the FPC to the mold. (d) Final two-part 3D printed mold used to shape the elastomeric part and conform the FPC with the Si Chips.

3.8.2.4 Electronic Interface

The finger part chosen to test this approach was the middle phalange of Vizzy finger (see **Figure 5** a). This phalange has the lowest active area, among all phalanges, resulting in the lowest number of sensors to cover the surface and thus simpler electronics. The design and development of a custom-made solution benefits from the flexibility in design but raises some challenges regarding integration, specifically the electronic interface.

First, we had to make sure the electronics could fit the finger part without restraining any finger, hand, or arm movements. We redesigned the aluminium part in a 1:1 scale using a PLA filament and a Witbox 3D printer (**Figure 52** b)) to fit two extra FPCs one for each side. The left FPC (L-00) is shown in **Figure 52** c.1) and the right FPC (R-11) is shown in **Figure 52** c.3). These two extra FPCs are used to covert the analog signals from the flexible sensor matrix with the 8 Si chips (described in the previous section) and output into the standard I2C communication interface (GND, VCC, SDA and SCL).

To connect the three board with each other, we used vertical flex connectors one for each board on the side of the finger. To capture the data from sensor each lateral FPC the main component of interest is the ADC, an ADS122C04 24-bit ADC, which requires two 1k 0402 resistors and two 1k 0402 100nF capacitors, to enable the readout of 4 individual sensors with a noise peak to peak ($Noise_{P-P}$) level of 25μV, at 10 samples per second per sensor with 500 μA current.

The digital signal output is interpreted by an Arduino MRK1000, which is responsible for communicating with the device and connecting to a Computer via USB, where the data is analysed.

There are three major differences from the previous electronic interface design. First, there is only one major component required, the ADS122C04 24-bit ADC which significantly simplifies the integration and design process. Second, it is connected to flex connectors allowing for easy fingertip replaceability as it was design to be modular. And last it can fit in the finger, which is a considerable advantage from an integration perspective. This is a significant milestone since using this integration process with the FPC there is no evidence that it contributes to the noise as it performed close to the levels provided in the technical data sheet for the currents and data rates tested.

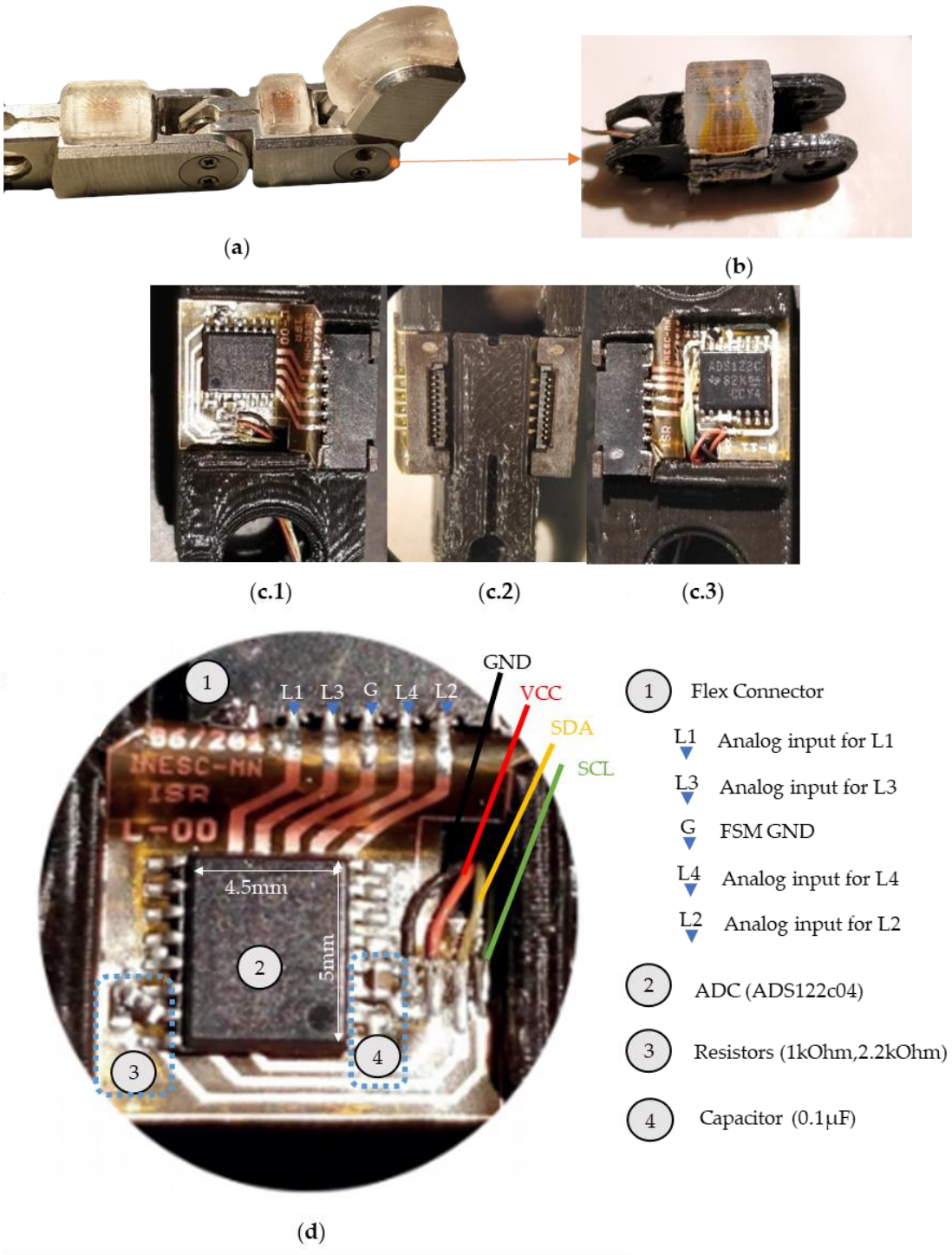

Figure 52. (a) Vizzy's finger is made of aluminum and is compatible with Figure 1 a) and is described in detail by a previews work [2]. (b) Redesigned 3D printed prototype for the middle phalange, the electronic interface, and the tactile sensor. (c) The prototyped finger part without the tactile sensor, detailing the flex connectors (c.2); the FPC (L-00) on the left side (c.1) and the FPC (R-11) on the right side (c.3); (d) Detail of the L-00 FPC, identifying the flex connector and the analog inputs, the ADC, resistors, capacitor and the I2C output.

3.8.3 Results and next steps

3.8.3.1 Si Chip

The transfer curve of MR(H) of all eight sensors, L1 through R4, displays a clear excellent uniformity, with an average sensitivity of 0.72 %/mT (14.1 mV/mT) and the moderate magnetoresistance values MR ~5 % consistent with excessive contact resistance in these series connection architectures (**Figure 53**). The spin valve sensors were characterized at wafer level. The sensor bias current (1 mA) was supplied by a Keithley 220 programable current source and the voltage measured by a Keithley 182 sensitive digital voltmeter, while a KEPCO bipolar power supply was used to set the current to the Helmholtz coils during the transfer curve MR(H) characterization. The chips used in this work show resistance in the saturation state R_{min} ~ 2 kΩ, coercivity H_c < 0.1 mT, and the transfer curves are centered around H=0 (small shift < 0.4 mT, caused by the Neel coupling and demagnetizing fields [34]) and a linear range of +/- 3 mT.

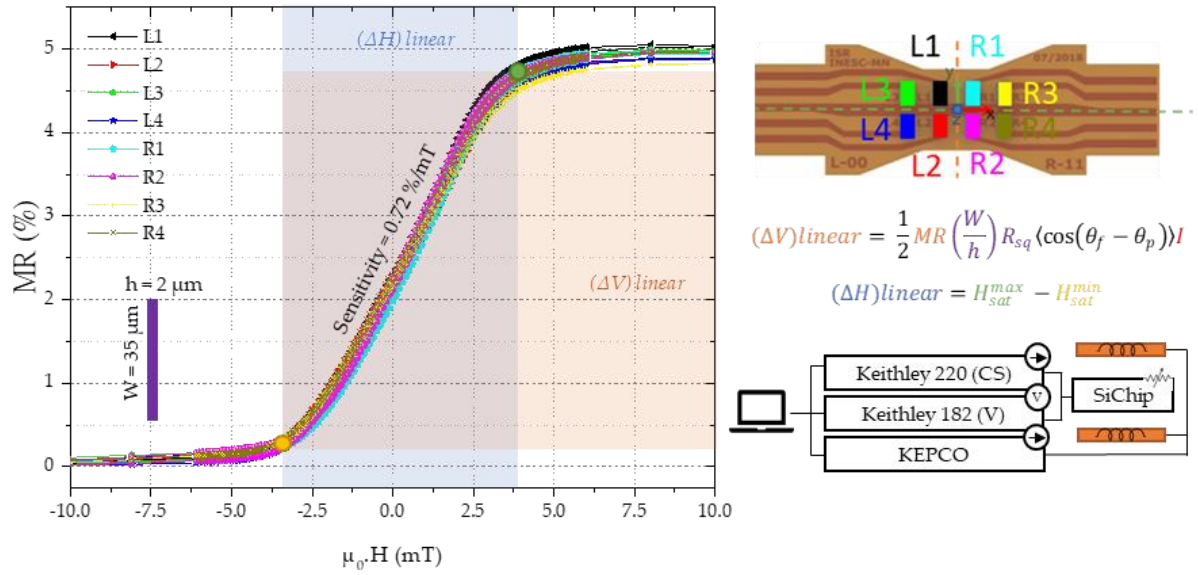

Figure 53. Transfer curve MR(H) curve of the used Si Chips within a field range of ±14 mT with a 1mA current. The current to the sensor was supplied by a Keithley 220 programable current source and the voltage measured by a Keithley 182 sensitive digital voltmeter, while the current provided to the Helmholtz coils responsible for controlling the applied field (µ0.H) is a KEPCO bipolar operational power supply.

3.8.3.2 Si Chip bonding to the FPC

The use of conductive epoxy to bonding the Si Chips to the FPC brought challenges such as controlling the volume of glue used per pad, the chip alignment, and the quality of the electrical contact. The pot life of this epoxy is about 10 minutes, which added an extra layer of difficulty during the Si chips manual placement on the FPC.

The silver conductive epoxy adhesive recommended curing instructions are: 24-hours at room temperature, 15 minutes at 65 °C or 7 minutes at 125 °C. To maximize the throughput, the 24 h curing at room temperature procedure was not considered. For the lower temperature, the curing was performed up to 60 minutes without significant improvement of the quality of the electric contact. However, only 10 minutes at 150 °C (B4) provided an electrical contact quality as good as when measuring directly on the contact pads of the chip. Lower $Noise_{P2P}$ was achieved by increasing the temperature to 250 °C and time to 30 minutes (B5), resulting in a better contact quality than provided by the probes placed on the contact pads of the Si Chip. Higher temperatures and time make the magnetoresistive sensor prone to inter layer diffusion and consequent loss of signal, so these are suitable process parameters for bonding.

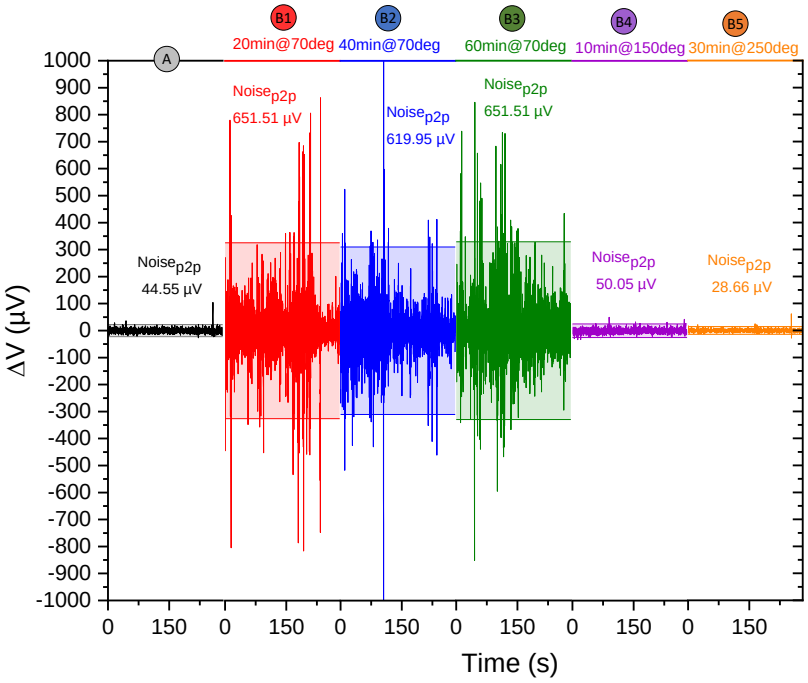

Figure 54. Comparison of different curing procedures. We show the voltage variation (µV) of the sensor used in L1 during a 300s measurement at H = 0T using a Keithley 220 as a current source, Keithley 182 voltmeter and micrometric probes to make contact with: the contact pads of the Si Chip(A), the FPC with the Si Chip bonded with the epoxy cured at 70 °C for 20 min(B1), 40min(B2) and 60 min(B3), cured at 150°C for 10min(B4) and 250 °C for 30min(B5).

3.8.3.3 Electronic Interface

The Si Chips bonded to the FPC characterized in **Figure 54** , were then embedded in the PDMS as described in section 3.8.2.3 and connected to the Electronic Interface detailed in 3.8.2.4.

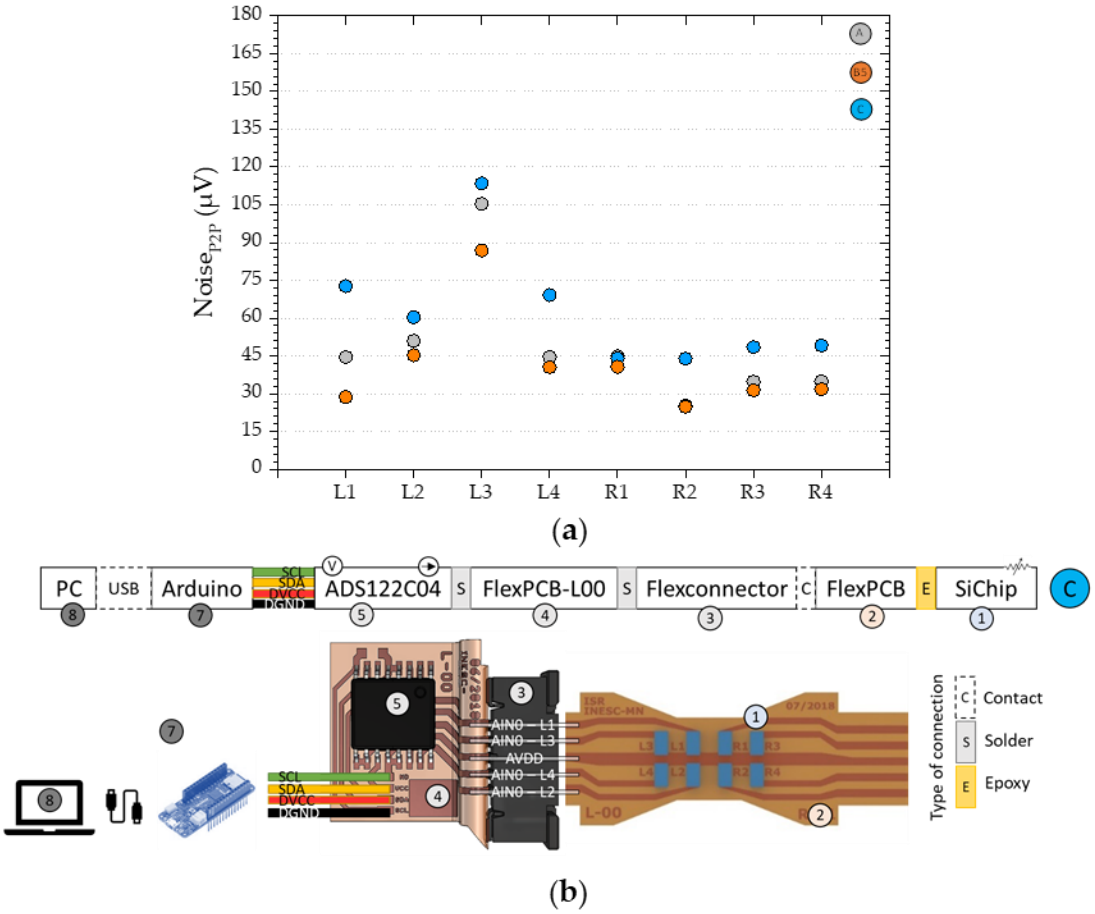

Figure 55. (a) Comparison between the Noise$_{P2P}$ (µV), for all eight sensors (L1 – R4), at H = 0T using a Keithley 220 as a current source, Keithley 182 voltmeter and micrometric probes directly on to the contact pads of the Si Chip(Ⓐ), the FPC with the Si Chip bonded with the epoxy cured at 250 °C for 30min (Ⓑ5) and the same but using the electronic interface(Ⓒ). (b) Schematic of the Electronic interface sources of noise and connections.

When comparing the Noise$_{P2P}$ before bonding process (Ⓐ) and the final device (Ⓒ) an average increase of 25% is observed, which considering the benefits of integration is considered an acceptable trade off.

The data rate (Samples Per Second) at which one can retrieve the data from the sensor is also an important parameter. The reaction time is defined by the sum of the acquisition time, the processing time and actuation time. Reducing the acquisition time requires higher samples per second (SPS). An increase in the Noise$_{P2P}$ is expected due to the sigma-delta ADC working principle and is characterized Figure 56.

The noise evolution with data rate is also consistent with initial testing with a 2.2 kΩ resistor

previously presented in **Erro! A origem da referência não foi encontrada.**.

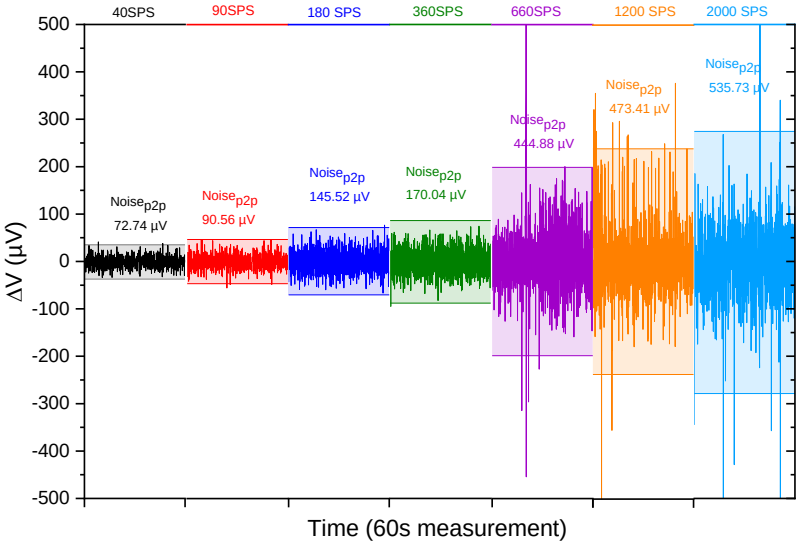

Figure 56. Noise$_{P2P}$ (µV) for sensor L1 at H = 0T in the final device (C) for different data rates.

1. Moreno, P.; Nunes, R.; Figueiredo, R.; Ferreira, R.; Bernardino, A.; Santos-Victor, J.; Beira, R.; Vargas, L.; Aragão, D.; Aragão, M. Robot 2015: Second Iberian Robotics Conference: Advances in Robotics, Volume 1. *Advances in Intelligent Systems and Computing* **2016**, *417*, 17–28, doi:10.1007/978-3-319-27146-0.

2. Feix, T.; Pawlik, R.; Schmiedmayer, H.-B.; Romero, J.; Kragi, D. A Comprehensive Grasp Taxonomy. *Robotics, Science and Systems Conference: Workshop on Understanding the Human Hand for Advancing Robotic Manipulation* **2009**, 2–3.

3. Parmiggiani, A.; Maggiali, M.; Natale, L.; Nori, F.; Schmitz, A.; Tsagarakis, N.; Victor, J.S.; Becchi, F.; Sandini, G.; Metta, G. The Design of the ICub Humanoid Robot. *International Journal of Humanoid Robotics* **2012**, *9*, 1–24, doi:10.1142/S0219843612500272.

4. Youssefian, S.; Rahbar, N.; Torres-Jara, E. Contact Behavior of Soft Spherical Tactile Sensors. *IEEE Sensors Journal* **2014**, *14*, 1435–1442, doi:10.1109/JSEN.2013.2296208.

5. Bicchi, A. Hands for Dexterous Manipulation and Robust Grasping: A Difficult Road toward Simplicity. *IEEE Transactions on Robotics and Automation* **2000**, *16*, 652–662, doi:10.1109/70.897777.

6. Yousef, H.; Boukallel, M.; Althoefer, K. Tactile Sensing for Dexterous In-Hand Manipulation in Robotics - A Review. *Sensors and Actuators, A: Physical* **2011**, *167*, 171–187, doi:10.1016/j.sna.2011.02.038.

7. Mason, M.T. Toward Robotic Manipulation. *Annual Review of Control, Robotics, and Autonomous Systems* **2018**, *1*, 1–28, doi:10.1146/annurev-control-060117-104848.

8. Li, Q.; Kroemer, O.; Su, Z.; Veiga, F.F.; Kaboli, M.; Ritter, H.J. A Review of Tactile Information: Perception and Action through Touch. *IEEE Transactions on Robotics* **2020**, *36*, 1619–1634, doi:10.1109/TRO.2020.3003230.

9. Dahiya, R.S.; Valle, M.; Metta, G. System Approach: A Paradigm for Robotic Tactile Sensing. *International Workshop on Advanced Motion Control, AMC* **2008**, *1*, 110–115, doi:10.1109/AMC.2008.4516050.

10. Dahiya, R.S.; Mittendorfer, P.; Valle, M.; Cheng, G.; Lumelsky, V.J. Directions toward Effective Utilization of Tactile Skin: A Review. *IEEE Sensors Journal* **2013**, *13*, 4121–4138, doi:10.1109/JSEN.2013.2279056.

11. Kappassov, Z.; Corrales, J.A.; Perdereau, V. Tactile Sensing in Dexterous Robot Hands - Review. *Robotics and Autonomous Systems* **2015**, *74*, 195–220, doi:10.1016/j.robot.2015.07.015.

12. Paulino, T.; Ribeiro, P.; Neto, M.; Cardoso, S.; Schmitz, A.; Santos-Victor, J.; Bernardino, A.; Jamone, L. Low-Cost 3-Axis Soft Tactile Sensors for the Human-Friendly Robot Vizzy. In Proceedings of the Proceedings - IEEE International Conference on Robotics and Automation; 2017; pp. 966–971.

13. Tekskan FlexiForce Load/Force Sensors and Systems Available online: http://www.tekscan.com/flexiforce.html.

14. Uart, W.; Voltage, D. OptoForce Analog Signal Converter. **2015**.

15. Peratech Touch Development Kit Available online: http://www.peratech.com/qtc-touch-processing-unit.html.

16. SynTouch Sensor Technology Available online: https://www.syntouchinc.com/sensor-technology/.

17. Whitesides, G.M. Soft Robotics. *Angewandte Chemie - International Edition* **2018**, *57*, 4258–4273, doi:10.1002/anie.201800907.

18. Lu, N.; Kim, D.H. Flexible and Stretchable Electronics Paving the Way for Soft Robotics. *Soft Robotics* **2014**, *1*, 53–62, doi:10.1089/soro.2013.0005.

19. Wattanasarn, S.; Noda, K.; Matsumoto, K.; Shimoyama, I. 3D Flexible Tactile Sensor Using Electromagnetic Induction Coils. *Proceedings of the IEEE International Conference on Micro Electro Mechanical Systems (MEMS)* **2012**, 488–491, doi:10.1109/MEMSYS.2012.6170230.

20. Ribeiro, P.; Alfhadel, A.; Franco, F.; Freitas, S.; Bernardino, A.; Schmitz, A.; Jamone, L. Bio-Inspired Ciliary Force Sensor for Robotic Platforms. **2016**.

21. Alfadhel, A.; Khan, M.A.; Freitas, S.C. de; Kosel, J.; Member, S. Magnetic Tactile Sensor for Braille Reading. **2016**, 1–6, doi:10.1109/JSEN.2016.2558599.

22. Hellebrekers, T.; Zhang, K.; Veloso, M.; Kroemer, O.; Majidi, C. Localization and Force-Feedback with Soft Magnetic Stickers for Precise Robot Manipulation. *IEEE International Conference on Intelligent Robots and Systems* **2020**, 8867–8874, doi:10.1109/IROS45743.2020.9341281.

23. Clark, J.J. A Magnetic Field Based Compliance Matching Sensor for High Resolution, High Compliance Tactile Sensing. *Robotics and Automation, 1988. Proceedings., 1988 IEEE International Conference on* **1988**, 772–777 vol.2, doi:10.1109/ROBOT.1988.12152.

24. Takenawa, S. A Magnetic Type Tactile Sensor Using a Two-Dimensional Array of Inductors. *Proceedings - IEEE International Conference on Robotics and Automation* **2009**, 3295–3300, doi:10.1109/ROBOT.2009.5152420.

25. Goka, M.; Nakamoto, H.; Takenawa, S. A Magnetic Type Tactile Sensor by GMR Elements and

Inductors. *IEEE/RSJ 2010 International Conference on Intelligent Robots and Systems, IROS 2010 - Conference Proceedings* **2010**, 885–890, doi:10.1109/IROS.2010.5650283.

26. Ledermann, C.; Wirges, S.; Oertel, D.; Mende, M.; Woern, H. Tactile Sensor on a Magnetic Basis Using Novel 3D Hall Sensor - First Prototypes and Results. *INES 2013 - IEEE 17th International Conference on Intelligent Engineering Systems, Proceedings* **2013**, 55–60, doi:10.1109/INES.2013.6632782.

27. Wang, H.; de Boer, G.; Kow, J.; Ghajari, M.; Alazmani, A.; Hewson, R.; Culmer, P. A Low-Cost Soft Tactile Sensing Array Using 3D Hall Sensors. *Procedia Engineering* **2016**, *168*, 650–653, doi:10.1016/j.proeng.2016.11.237.

28. Hackwood, S.; Beni, G. Shear-Sensitive Magnetoresistive Robotic Tactile Sensor. *IEEE Transactions on Magnetics* **1986**, *22*, 394–396, doi:10.1109/TMAG.1986.1064386.

29. Hackwood, S.; Beni, G.; Hornak, L. a.; Wolfe, R.; Nelson, T.J.J. A Torque-Sensitive Tactile Array for Robotics. *The International Journal of Robotics Research* **1983**, *2*, 46–50, doi:10.1177/027836498300200204.

30. Tomo, T.P.; Wong, W.K.; Schmitz, A.; Kristanto, H.; Sarazin, A.; Jamone, L.; Somlor, S.; Sugano, S. A Modular, Distributed, Soft, 3-Axis Sensor System for Robot Hands. *IEEE-RAS International Conference on Humanoid Robots* **2016**, 454–460, doi:10.1109/HUMANOIDS.2016.7803315.

31. Tomo, T.P.; Somlor, S.; Schmitz, A.; Jamone, L.; Huang, W.; Kristanto, H.; Sugano, S. Design and Characterization of a Three-Axis Hall Effect-Based Soft Skin Sensor. *Sensors (Switzerland)* **2016**, *16*, doi:10.3390/s16040491.

32. Yan, Y.; Hu, Z.; Yang, Z.; Yuan, W.; Song, C.; Pan, J.; Shen, Y. Soft Magnetic Skin for Super-Resolution Tactile Sensing with Force Self-Decoupling. *Science Robotics* **2021**, *6*, eabc8801, doi:10.1126/scirobotics.abc8801.

33. Tomo, T.P.; Schmitz, A.; Wong, W.K.; Kristanto, H.; Somlor, S.; Hwang, J.; Jamone, L.; Sugano, S. Covering a Robot Fingertip With USkin: A Soft Electronic Skin With Distributed 3-Axis Force Sensitive Elements for Robot Hands. *IEEE Robotics and Automation Letters* **2018**, *3*, 124–131, doi:10.1109/LRA.2017.2734965.

34. Tomo, T.P.; Regoli, M.; Schmitz, A.; Natale, L.; Kristanto, H.; Somlor, S.; Jamone, L.; Metta, G.; Sugano, S. A New Silicone Structure for USkin - A Soft, Distributed, Digital 3-Axis Skin Sensor and Its Integration on the Humanoid Robot ICub. *IEEE Robotics and Automation Letters* **2018**, *3*, 2584–2591, doi:10.1109/LRA.2018.2812915.

35. COEY, J.M.D. *Magnetism and Magnetic Materials*; Cambridge University Press: Dublin, 2009;

ISBN 9780521816144.

36. Model, R.; Trahms, L. An Inverse Problem of Magnetic Source Localization. *Numer Algor* **1993**, *5*, 603–610, doi:10.1007/bf02221587.

37. Wang, X.; Meng, M.Q.H.; Hu, C. A Localization Method Using 3-Axis Magnetoresistive Sensors for Tracking of Capsule Endoscope. *Annual International Conference of the IEEE Engineering in Medicine and Biology - Proceedings* **2006**, *1*, 2522–2525, doi:10.1109/IEMBS.2006.260711.

38. Sun, Z.; Foong, S.; Marechal, L.; Teo, T.H.; Tan, U.X.; Shabbir, A. Using Heterogeneous Sensory Measurements in a Compliant Magnetic Localization System for Medical Intervention. *IEEE/ASME International Conference on Advanced Intelligent Mechatronics, AIM* **2015**, *2015-Augus*, 133–138, doi:10.1109/AIM.2015.7222521.

39. Marechal, L.; Foong, S.; Sun, Z.; Wood, K.L. Design Optimization of the Sensor Spatial Arrangement in a Direct Magnetic Field-Based Localization System for Medical Applications. *Proceedings of the Annual International Conference of the IEEE Engineering in Medicine and Biology Society, EMBS* **2015**, *2015-Novem*, 897–900, doi:10.1109/EMBC.2015.7318507.

40. Ribeiro, P.; Neto, M.; Cardoso, S. Strategy for Determining a Magnet Position in a 2-D Space Using 1-D Sensors. *IEEE Transactions on Magnetics* **2018**, *54*, doi:10.1109/TMAG.2018.2851928.

41. Wu, F.Y.; Foong, S.; Sun, Z. A Hybrid Field Model for Enhanced Magnetic Localization and Position Control. *IEEE/ASME Transactions on Mechatronics* **2015**, *20*, 1278–1287, doi:10.1109/TMECH.2014.2341644.

42. Wu, F.; Robert, N.M.; Frey, D.D.; Foong, S. Enhanced Magnetic Localization with Artificial Neural Network Field Models. *Robotics and Automation (ICRA), 2013 IEEE International Conference on* **2013**, 1560–1565, doi:10.1109/ICRA.2013.6630778.

43. Derby, N.; Olbert, S. Cylindrical Magnets and Ideal Solenoids. *American Journal of Physics* **2010**, *78*, 229–235, doi:10.1119/1.3256157.

44. Silva, A. v.; Leitao, D.C.; Valadeiro, J.; Amaral, J.; Freitas, P.P.; Cardoso, S. Linearization Strategies for High Sensitivity Magnetoresistive Sensors. *The European Physical Journal Applied Physics* **2015**, *72*, 10601, doi:10.1051/epjap/2015150214.

45. Parkin, S.S.P. Flexible Giant Magnetoresistance Sensors. *Applied Physics Letters* **1996**, *69*, 3092–3094, doi:10.1063/1.117315.

46. Gaspar, J.; Fonseca, H.; Paz, E.; Costa, M.; Martins, M.; Ferreira, R.; Cardoso, S.; Freitas, P.P. Fabrication and Mechanical Characterization of Flexible Devices with Sensors with

Magnetoresistance Responses above 150 %. 10–12.

47. Valadeiro, J.; Amaral, J.; Leitao, D.C.; Silva, A. v.; Gaspar, J.; Silva, M.; Costa, M.; Martins, M.; Franco, F.; Fonseca, H.; et al. Bending Effect on Magnetoresistive Silicon Probes. *IEEE Transactions on Magnetics* **2015**, *51*, 3–6, doi:10.1109/TMAG.2015.2441956.

48. Makarov, D.; Melzer, M.; Karnaushenko, D.; Schmidt, O.G.; Makarov, D.; Melzer, M.; Karnaushenko, D.; Schmidt, O.G. Shapeable Magnetoelectronics. *Applied Physics Review* **2016**, *3*, 011101, doi:10.1063/1.4938497.

49. Uhrmann, T.; Bär, L.; Dimopoulos, T.; Wiese, N.; Rührig, M.; Lechner, a. Magnetostrictive GMR Sensor on Flexible Polyimide Substrates. *Journal of Magnetism and Magnetic Materials* **2006**, *307*, 209–211, doi:10.1016/j.jmmm.2006.03.070.

50. Karnaushenko, D.; Makarov, D.; St??ber, M.; Karnaushenko, D.D.; Baunack, S.; Schmidt, O.G. High-Performance Magnetic Sensorics for Printable and Flexible Electronics. *Advanced Materials* **2015**, *27*, 880–885, doi:10.1002/adma.201403907.

51. Singh, M.; Haverinen, H.M.; Dhagat, P.; Jabbour, G.E. Inkjet Printing-Process and Its Applications. *Advanced Materials* **2010**, *22*, 673–685, doi:10.1002/adma.200901141.

52. Singh, W.S.; Rao, B.P.C.; Thirunavukkarasu, S.; Jayakumar, T. Flexible GMR Sensor Array for Magnetic Flux Leakage Testing of Steel Track Ropes. *Journal of Sensors* **2012**, *2012*, doi:10.1155/2012/129074.

53. Gaspar, J.; Fonseca, H.; Paz, E.; Martins, M.; Valadeiro, J.; Cardoso, S.; Ferreira, R.; Freitas, P.P. Flexible Magnetoresistive Sensors Designed for Conformal Integration. *IEEE Transactions on Magnetics* **2017**, *53*, 5–8, doi:10.1109/TMAG.2016.2623669.

54. Melzer, M.; Makarov, D.; Calvimontes, A.; Karnaushenko, D.; Baunack, S.; Kaltofen, R.; Mei, Y.; Schmidt, O.G. Stretchable Magnetoelectronics. *Nano Letters* **2011**, *11*, 2522–2526, doi:10.1021/nl201108b.

55. Melzer, M.; Lin, G.; Makarov, D.; Schmidt, O.G. Stretchable Spin Valves on Elastomer Membranes by Predetermined Periodic Fracture and Random Wrinkling. *Advanced Materials* **2012**, *24*, 6468–6472, doi:10.1002/adma.201201898.

56. Mimoun, B.; Pham, H.T.M.; Henneken, V.; Dekker, R. Residue-Free Plasma Etching of Polyimide Coatings for Small Pitch Vias with Improved Step Coverage. *Journal of Vacuum Science & Technology B: Microelectronics and Nanometer Structures* **2013**, *31*, 021201, doi:10.1116/1.4788795.

57. Dick, A.R.; Bell, W.K.; Luke, B.; Maines, E.; Mueller, B.; Rawlings, B.; Kohl, P.A.; Grant Willson, C. High Aspect Ratio Patterning of Photosensitive Polyimide with Low Thermal

Expansion Coefficient and Low Dielectric Constant. *Journal of Micro/Nanolithography, MEMS, and MOEMS* **2016**, *15*, 033503, doi:10.1117/1.JMM.15.3.033503.

58. Gehanno, V.; Freitas, P.P.; Veloso, A.; Ferreira, J.; Almeida, B.; Sousa, J.B.; Kling, A.; Soares, J.C.; da Silva, M.F. Ion Beam Deposition of Mn-Ir Spin Valves. *IEEE Transactions on Magnetics* **1999**, *35*, 4361–4367, doi:10.1109/20.799086.

59. Alfadhel, A.; Khan, M.A.; Cardoso, S.; Leitao, D.; Kosel, J. A Magnetoresistive Tactile Sensor for Harsh Environment Applications. *Sensors (Switzerland)* **2016**, *16*, doi:10.3390/s16050650.

60. Fu, Y.B.; Ogden, R.W. *Nonlinear Elasticity: Theory and Applications*; Cambridge University Press: Cambrigde, 2001; ISBN 9780511526466.

Chapter 4

Simulation and testing

4.1 Experimental Setup

The transport curve and electrical characterization are essential for fabrication and manufacturing control but do not provide clear insights into the sensor operational limitations. Fully integrating the sensor on the robot hand or just the finger is a complex and time-consuming task, so it becomes valuable to test the tactile sensors as close to the application conditions as possible to an actual situation. Therefore, a setup that could apply and measure forces precisely is vital for further optimizing and developing the tactile sensor. We assembled a setup comprised of the magnetic tactile sensor, a three-axis cartesian motorized stage (Thorlabs DDS220), and a 6-degree force sensor (ATI nano 17). The tactile sensor is fixed on the stage using a 3D printed part (**Figure 57** (a.1) and (a.2)).

The ATI nano 17 is a multi-axis force and torque sensor system that can measure both forces (F_x, F_y and F_z) and torques (T_x, T_y and T_z). In this setup we attached one to an aluminum cantilever fixed to the table. A computer communicates with the stage, providing instructions to align and against each other while reading their output. This setup configuration allows an evaluation of the sensor performance under normal and shear forces. For this case, the tactile sensor curved surface top-centre point was aligned with the ATI nano sensor, and the stage presses the sensors against each other.

The sensors are aligned visually in such a way that the tactile sensor touches the ATI nano centre. The alignment results from actuating the stage and visually checking whether they are centred in X and Y directions and touching in the Z direction. After alignment, the stage moves vertically in steps of 0.05 mm up to 1 mm, pressing the sensors against each other. The recorded values from the ATI nano and tactile sensor for each step are plotted in **Figure 58** (a) and (b), respectively. The load phase corresponding to pressing the tactile and force sensors against each other is followed by an unload phase, where the opposite occurs.

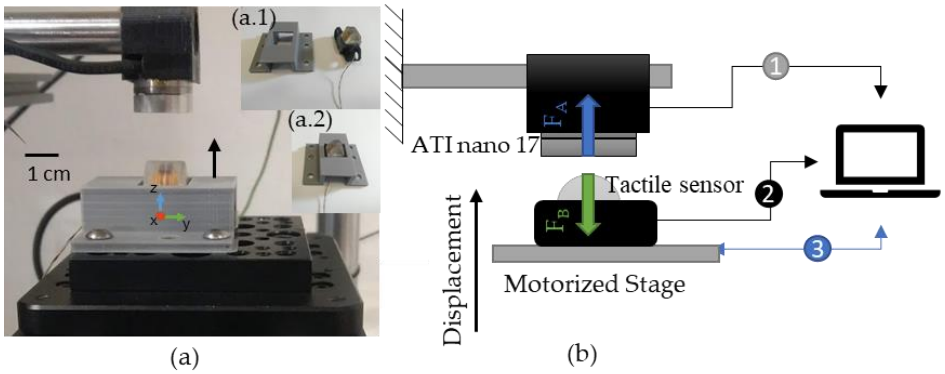

Figure 57. (**a**) The aluminium rod in a cantilever configuration, the ATI nano 17, the Magnetic tactile sensor, and the stage; (a.1) shows a 3D printed part (left) to fix the Tactile sensor (right) to the stage (a.2) shows how the 3D printed part fits with the Tactile sensor. (**b**) Force equilibrium and working principles of the setup, where the ❶ identifies data from the ATI nano 17(F_x, F_y, F_z, T_x, T_y and T_z), ❷ the data from both L-00 and R-11 lateral FPCS of the eight sensors (L1 through R4) and ❸ the data from the PC to the three servo motors Thorlabs stage controlling the displacement.

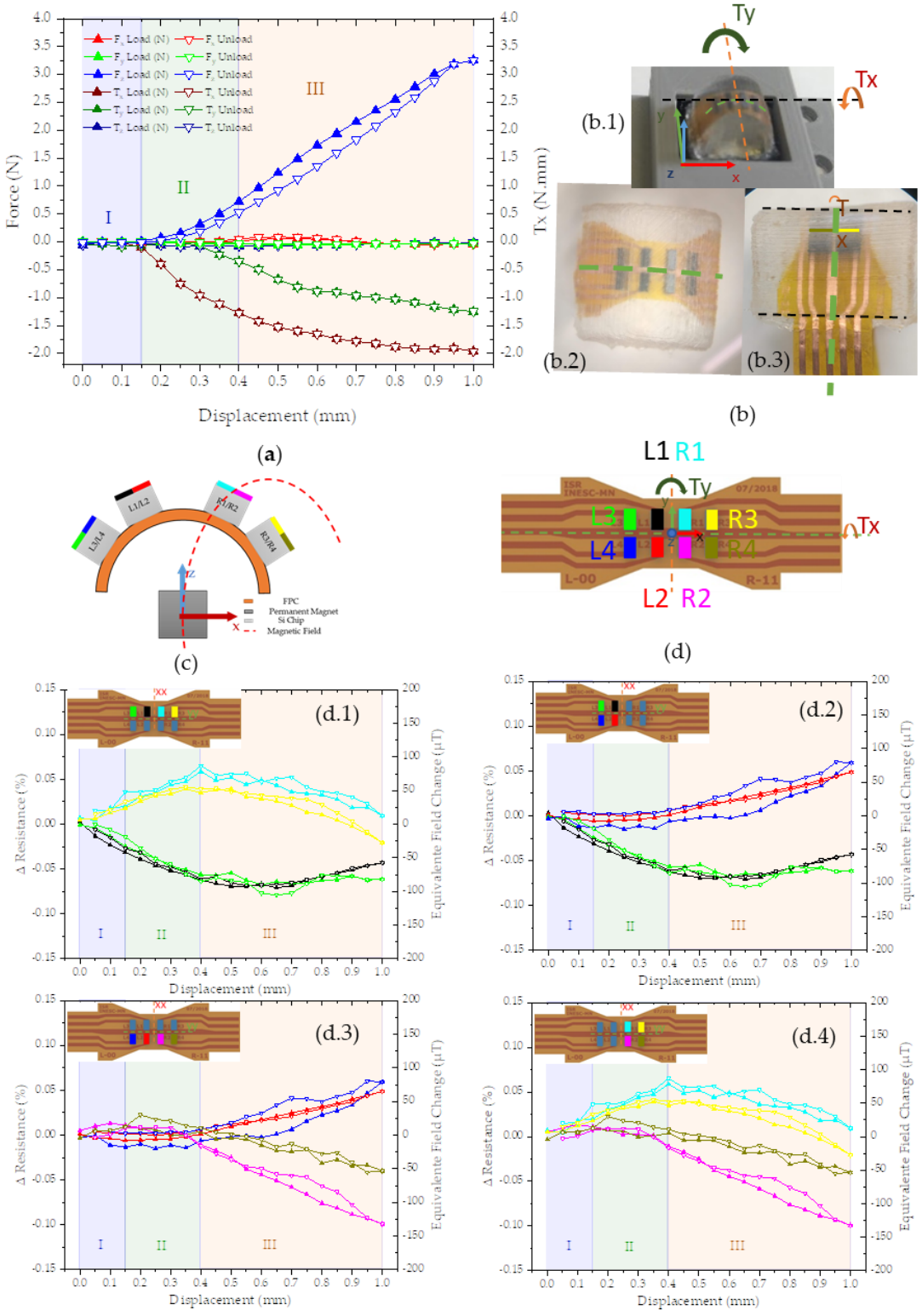

Figure 58. (a) Force and momentum data from ATI nano 17 (F_x, F_y, F_z, T_x, T_y and T_z) for the loading and unloading phases. (b) (c) Detail of the sensor with the T_x and T_y schematics detailed. (d) a schematic view of the sensor matrix in the XZ plane; (e) a schematic view of the sensor matrix in the XY plane, showing the sensors; (f) Set of four graphs showing the symmetry for the sensor output by choosing sensors: (f.1) with positive y coordinates (odd numbers – L1, R1, L3, R3); (f.2) with negative y coordinates (pair numbers – L2, R2, L4, R4); (f.3) with negative x coordinates (left side – L1, L2, L3, L4); (f.4) with positive x coordinates (right side – R1, R2, R3, R4).

The stage position changes every 30s providing the time frame to record the sensor's output. The values presented in **Figure 58** d) 1-4 show the average value for each position. The ATI nano output already considers a calibration from the manufacturer to provide the force and torque output in **Figure 58** (a). The tactile sensor output comprises individual voltage measurements of the eight Si Chips. We use the percentage of change in resistance, ΔResistance (%), to quantify the applied magnetic field change (Equivalent Field Change (μT).

The percentage of change in resistance is the arithmetic average for a sensor when the stage is in a position (p) relative to the arithmetic mean of the same sensor for the initial position of the stage, without any applied force.

$$\Delta R_p(\%) = \frac{\overline{R_{p\iota}} - \overline{R_{p=0,\iota}}}{\overline{R_{p=0}}} \times 100 \tag{3}$$

$$\text{Equivalent Field Change } (\mu\text{T}) = \frac{\Delta R_p(\%)}{Sensitivity\left(\frac{\%}{\mu T}\right)} \tag{4}$$

The equivalent field change represents the change in magnetic field aligned with the sensor plane and perpendicular to the pinned layer and we calculate it using equation (4). The change in resistance results from equation (3), while the value used for sensitivity used is 0.72%/mT. The value of sensitivity is the average of the individual sensor sensitivity obtained from the slope of the MR (H) curve shown in **Figure 53**. The Si Chips have a spin valve sensor series sensitive to magnetic fields in the x-axis and the permanent magnet aligned with the FPC center. This configuration results in the sensor output of **Figure 58** (d.1 – d.4), where sensors on the left side detect a decrease in a magnetic field (d.2) while the sensors on the right side show the opposite behavior (d.4).

The values recorded can be divided into three main phases: an initial adjustment phase (I-blue), a torque-dominated phase (II-green), and a vertical force-dominated phase (III-orange). The initial adjustment phase (I-blue) occurs in the first 150 μm of vertical stage displacement. In this phase, the forces are below the detection limit of ATI nano 17 but detectable by the tactile sensor since the tactile sensor matrix measures a change in a magnetic field coherent with the displacement, both for loading and unloading. Moreover, the sensor output has a precise symmetry, with positive y coordinates (odd numbers – L1, R1, L3, R3) and negative y coordinates (even numbers – L2, R2, L4, R4). We attribute this phase to gaps present in the whole experimental setup system that requires less force than the minimum force the ATI nano can detect.

The second phase (II-green) occurs from 0.15 to 0.4mm, and we observe a more significant increase in T_x than in F_z, thus we have named it a torque-dominated phase. Torque was not a intentionally imposed, but it is consistent with a misalignment during production or assemblage of the sensor matrix (see **Figure 58** (b.3)). The tactile sensor's output is consistent with a rotation in the x-axis, where the sensors with positive y-coordinates (odd numbers – L1, R1, L3, R3) and negative y-coordinates (even numbers – L2, R2, L4, R4) show symmetric output observable when comparing the signal output **Figure 58** (d.1) e (d.3).

The last phase (III-orange) where F_z becomes a more significant factor than any other force or torque. From 0.4mm to 1mm, F_z has a similar behaviour to the simulated force (**Figure 60** (f)).

4.2 Experimental Setup Simulation

4.2.1 Simulation Assumptions

To improve our understanding of the results and accelerate the development and optimization of new designs we represented and simulated the same system in three dimensions using finite element software COMSOL. The model only considers the Si chips, the elastomeric part, and the ATI nano 17 (**Figure 59**). The FPC, the epoxy glue and the finger part are not considered in the model since they would significantly increase the computational complexity and their contributions are most likely negligible. The main purpose of this simulation is to explore the relationship between the displacement and the magnetic field detected in the surface of the Si Chips (related to the sensor output in the experimental data). This relationship represents the working principle of the device, so understanding the metrics that have the most impact on the working principle allows us to develop better suited devices for the application. Moreover, simulation decreases the iteration time significantly, thus connecting the experimental data and simulation data is key for an efficient design and development of these sensors.

The simulation comprises: (i) a mechanical model, where the bottom of the elastomeric part was fixed (blue area in **Figure 59** (a.3)) and the ATI nano 17 was pushed against it in steps of 0.05mm until 0.5mm and (ii) a magnetic model, where the magnetic field H (H_x, H_y, H_z) was calculated for each Si chip.

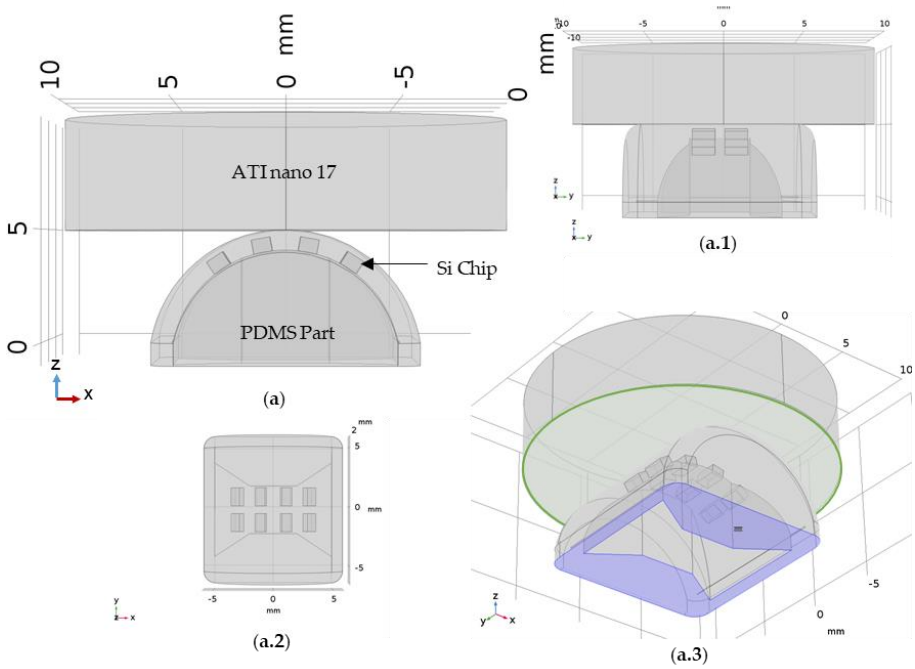

Figure 59. Three-dimensional geometry used for the simulations: (a) XZ plane view (a.1) YZ plane view (a.2) XY plane view and (a.3) an orthogonal view identifying the initial constraints, the blue represents the finger part on the Thorlabs stage and thus was fixed, while to the green area highlights the surface that will be pressed against the PDMS part by steps of 0.05mm up to a maximum of 0.5mm.

4.2.2 Mechanical Simulation

The mechanical model simulates the deformation of the PDMS part when pressed by the ATI nano 17, and consequently, how the Si Chips are displaced.

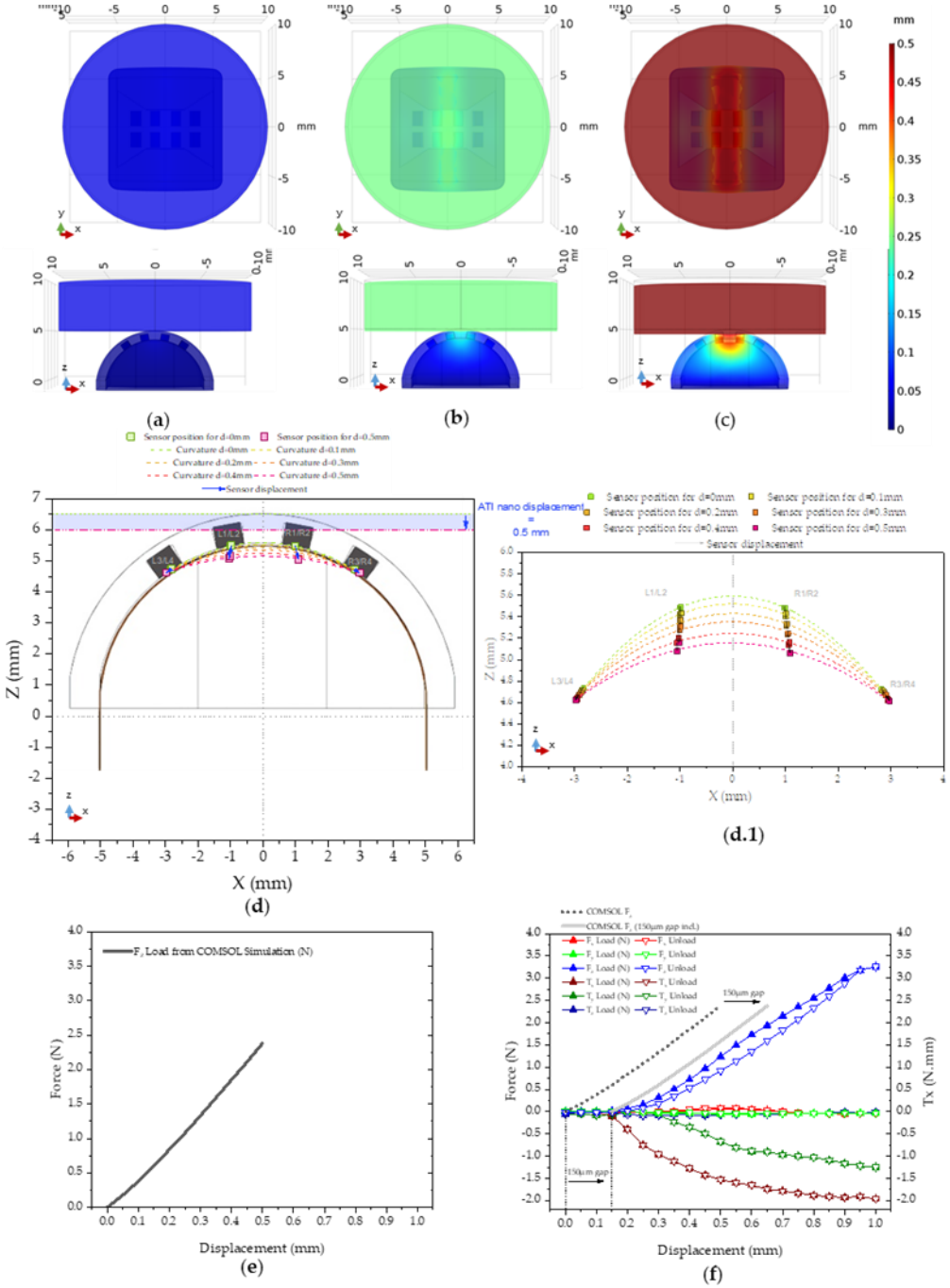

Figure 60. Results of the three-dimensional mechanical simulation detailing the xy plane and zx plane and showing in color the displacement results for the steps: (a) 0.05 mm; (b) 0.25 mm and (c) 0.5 mm. (d) XZ plane showing the position and displacement of the Si Chips (d.1) Detail of the matrix displacement for each pressing step. (e) The force value, obtained by integrating the value of force in each point of the green surface on Figure 59 (a.3) (f) Simulated force against the displacement and compared to the experimental force (F_z) measured by the ATI nano 17, also represented the 150µm gap assumed to exist in phase I.

Table 6. Parameters used for each material in the mechanical simulation.

Mechanical Properties			
Part	PDMS	ATI Nano 17	Si Chip
Material	PDMS – Polydimethylsiloxane (1:15)	Aluminum	Silicon [solid, <100> axis]
E	750 kPa	6.91 GPa	13.02 GPa
υ	0.49	0.33	0.28
K	-	25.98 GPa	79.67 GPa
μ	251.68 N/mm²	-	-
λ	12.33 kN/mm²	-	-
E = Young modulus; υ = Poisson ratio; K = Bulk Modulus; Lamé parameters - μ and λ.			

The most challenging aspect of this simulation was defining the interface behaviour correctly. The interface between the ATI nano and the elastomeric part had to be defined in such a way that allowed for the area of contact to change as the ATI nano displacement increased. This was achieved by using the Augmented Lagrange Pressure Method available in COMSOL 3.5 to simulate the evolution of the contact area. To simulate the deformations of the PDMS part an incompressible neo-Hookean hyperelastic material model was used in COMSOL [50]. The parameters used for the mechanical simulations are detailed in **Table 6**.

In this simulation we forced a vertical and controlled displacement of the aluminium cylinder to compress the elastomeric part. This displacement forced the deformation of the elastomeric part and a reaction force on the aluminium part. The total force measured in the green surface is plotted against the displacement on **Figure 60** (e) and compared with the experimental data in (f). The mechanical model seems to describe the experimental data acceptably, particularly if we consider the phase I 150μm gap discussed in the experimental data. The simulation was only done for 0.5mm to make sure we were working in the elastic domain so the model could have any significance.

4.2.3 Magnetic Simulation

The magnetic simulation is performed for each displacement step because for each displacement a different position in space results in a different magnetic field. The magnitude of the magnetic field generated by the cylindrical NdFeB magnet is simulated and measured on the active area of the Si chips for each displacement. For the geometrical configuration of the tactile sensor the magnetic field ranges between the -2 mT to 2mT on the surface of the Si chips where the sensor is fabricated (colored surfaces on **Figure 61** (a)). The transfer curve (**Figure 53**) shows that the sensors respond linearly to magnetic fields ranging from -2.5 to 2.5 mT perpendicular to their easy axis. However, each point of the colored surfaces (**Figure 61** (a)) is a three-dimensional vector of magnetic field with origin on the permanent magnet. To calculate the field detected by the sensor and be able to compare the simulation to the experimental data we must consider the active area of the sensors and the angle of the surface with respect to the XY plane.

The active sensor area of 200x95µm^2 (see in **Figure 49** (b)) in the center of the Si Chip is used for the determining the magnetic field in further calculations such as Figure 61 (c), as opposed to the average of the colored surface as a whole. In the same figure we can see a linear relationship between the magnetic field and the displacement. Moreover, symmetry between the position of the sensors in the matrix and the simulated magnetic fields is expected, as sensors on the left side (negative x-coordinates) show a negative Hx and sensors with a positive y-coordinate show a positive Hy.

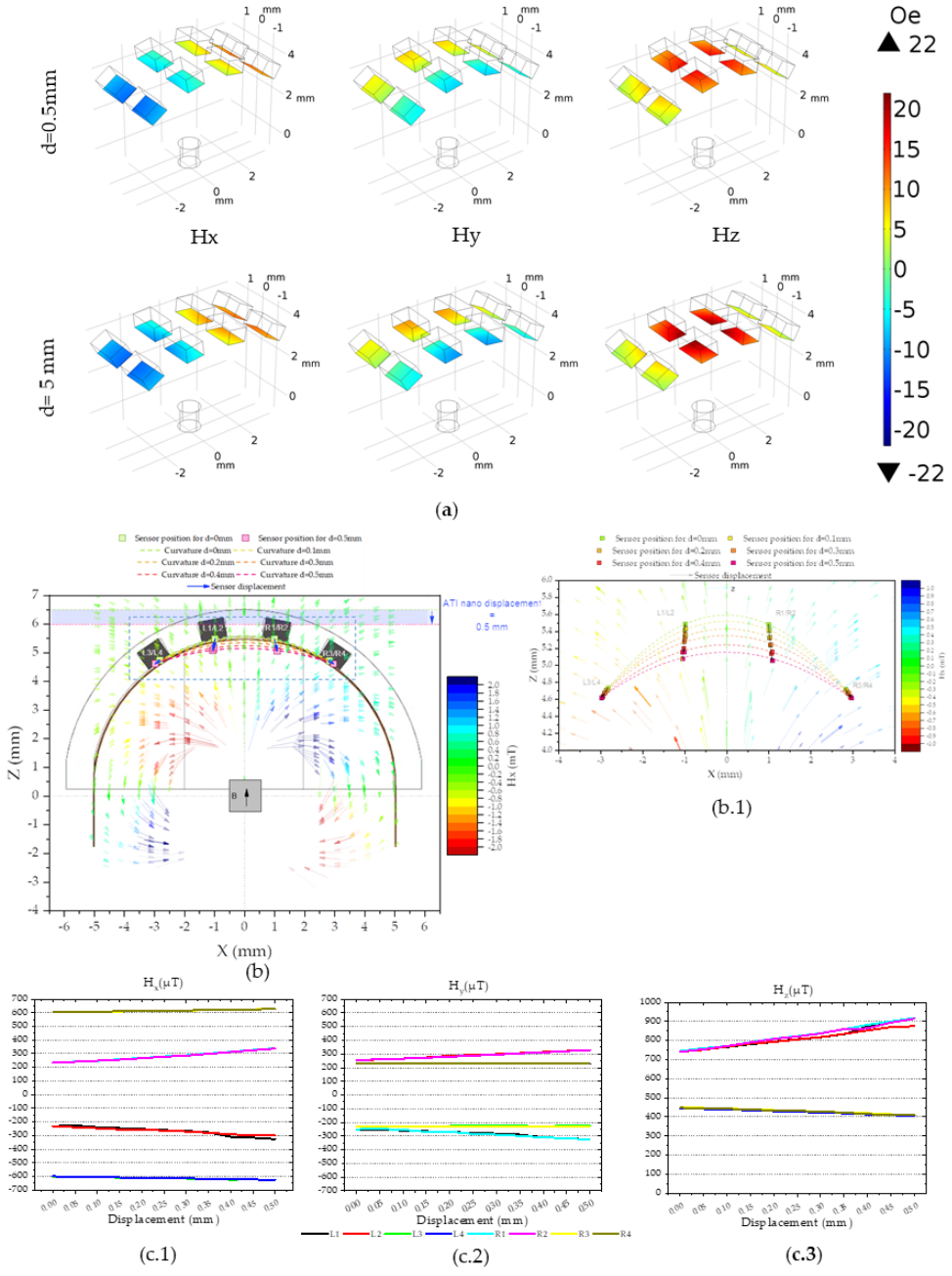

Figure 61. 3-dimensional magnetic simulation, showing (a) the Si Chip and the field magnitude in Hx, Hy and Hz magnitude on the surface where the sensors for d=0 and 0.5mm. (b) XZ plane showing the position and displacement of the Si Chips, the position of the magnet and the magnetic field lines (d.1) Detail of the matrix displacement for each pressing step. (c) Si Chip area (1.5x0.8cm^2) and active sensor area (200x95µm2). (d) Average magnetic field magnitude calculation in each Si Chip in their active sensor area (200x95µm^2) for each component in µT: (d.1) H_x (d.2) H_y and (d.3) H_z.

4.2.3.1 *Sensor tilting*

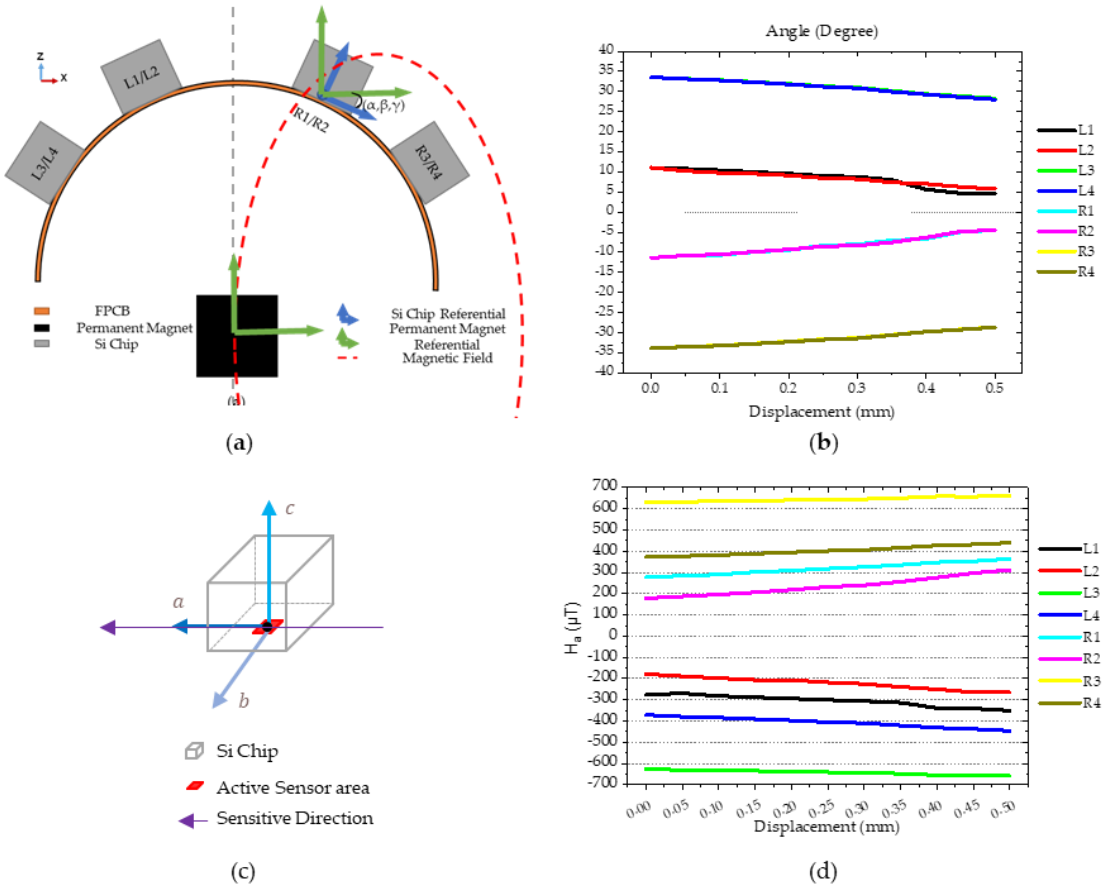

Figure 62. (a) XZ plane schematics showing the relationship between the Si Chip (blue) and Permanent Magnet (green) reference frame.; (b) angle α simulated and taken from the mechanical simulation for each Si Chip, in this case both β and γ are 0. (c) (d) The magnetic field magnitude on the active area of the sensor.

In addition to the sensors active area position in space we must consider the rotation angle of the Si Chip surface with respect to the permanent magnet referential in three dimensions (α, β, γ). The Si Chip surface plane with the XY plane is referred as α. The green referential frame represents the magnetic simulation system of coordinates (x,y,z), with origin on the center of the magnet (. The blue referential, (a,b,c), has origin in the center of the sensor and is defined with $\vec{e}_a$ and $\vec{e}_b$ being orthogonal and lying in the sensor plane and $\vec{e}_a$ aligned with the sensor sensitive direction. Because the sensor is only sensitive in one direction in plane and the field is a vector in the 3-dimensions, taking the angle (α, β, γ) of the Si Chip with the permanent magnet is the need to evaluate the magnitude of the sensor output, henceforth $\vec{H}_{sensor}$. To determine its value, we use the following:

$$\vec{H}_{sensor} = R_x(\alpha)\, R_y(\beta)\, R_z(\gamma)\, \vec{H} \tag{5}$$

$$\begin{bmatrix} H_a \\ H_b \\ H_c \end{bmatrix} = \begin{bmatrix} 1 & 0 & 0 \\ 0 & \cos\alpha & -\sin\alpha \\ 0 & \sin\alpha & \cos\alpha \end{bmatrix} \begin{bmatrix} \cos\beta & 0 & \sin\beta \\ 0 & 1 & 0 \\ -\sin\beta & 0 & \cos\beta \end{bmatrix} \begin{bmatrix} \cos\gamma & -\sin\gamma & 0 \\ \sin\gamma & \cos\gamma & 0 \\ 0 & 0 & 1 \end{bmatrix} \begin{bmatrix} H_x \\ H_y \\ H_z \end{bmatrix} \quad (6)$$

The α values obtained in the simulation for each Si Chip are shown in Figure 62 (b). For this case, the angles β and γ are considered null as no change was observed in this simulation. This is attributed mainly to the pressing object flat geometry that has an area larger than the sensor as well as the applied force only has a vertical component. Smaller or curvilinear pressing objects would have a significant impact on β, while torques and/or shear forces would impact γ.

To estimate the $\vec{H}_{sensor}\ (H_a, H_b, H_c)$ we use equation (5), where $\vec{H}\ (H_x, H_y, H_z)$ is the magnetic field vector for the coordinates in 3d space corresponding to the centre of sensor's active area. The matrices in (6) are used to obtain $\vec{H}$ in the abc referential.

The ratio between H_a and H_b is 2:1 and the fact that H_b << 1 mT, suggest that H_b influence due to crossfield phenomena on the sensor output can be discarded. The values of H_a against the displacement are shown in Figure 62 (c). With these calculations we estimate H_a range between -0.7 to 0.7mT, which is well within the linear range of the sensor – transfer curves presented in **Figure 53**.

4.2.4 Simulation vs Experimental

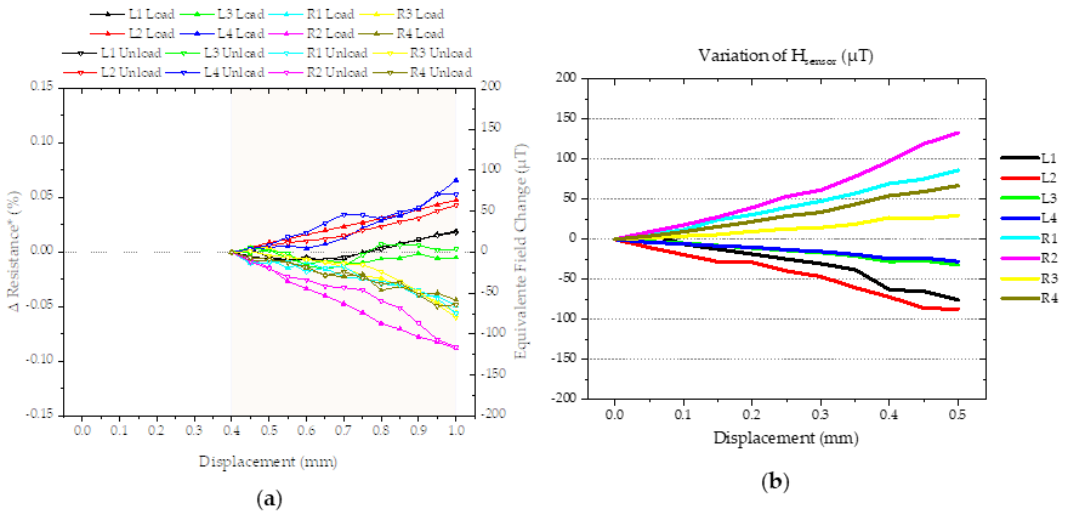

Figure 63. (a) Experimental results: sensor output as a function of displacement for phase III. (b) Simulated results considering change in angle change.

In section 4, we discuss the three phases of the physical experiment and how the change in resistance value is obtained. This means that a change of 0.05% in the signal of the sensor should correspond to a 50μT change. To compare with the simulation results we need: 1) only use the data

from phase III of experimental data; 2) to use the same principles for the simulation data, meaning we need to look at changes in magnetic field.

The first part implies we plot the change of resistance discarding Phase I and II and assume the $\overline{R_{p=0}}$ in equation (3) to be $p = 0.4$ instead of $p = 0$ (**Figure 63** (a)). As for the simulated data we use H_a and the field for the position to be visually clear the similarities between both sets of data, **Figure 63** (b) shows the variation of the H_a as a function of displacement for each sensor. This can be compared directly with the Equivalent field change (μT). The simulation seems to predict the experiment accurately for the sensors L2, R1, R2, and R4.

Chapter 5

Conclusions and Final remarks

5.1 Conclusions

We proposed, designed, developed, fabricated, simulated, and tested an innovative design for a tactile sensor integrated into the finger part of a robotic hand. The design is based on magnetic sensing and leveraging a novel working principle. The development of two novel microfabrication processes compatible with the INESC-MN facilities, designing and integrating an analog-digital circuit board to read the sensor's output, programming a new tactile sensor force characterization setup, and simulating the experimental testing using finite elements in COMSOL are parts required to develop and integrate the concept in a robotic finger.

The first contribution of this work is to clarify and discuss the interpretation of magnetic tactile sensors working principle. We use a geometrical approach to define the working principle and further explain the importance of the correlation between the three vectors the change in the magnetic field ($\Delta\vec{H}$), the applied force ($\vec{F}$) and the permanent magnet displacement ($\vec{d}$). The inversion problem is well known, but the way we approached it through the visualizations should provide better insight and intuition and help significantly further research and development of new concepts and algorithms for magnet/sensor position tracking.

Another relevant milestone in the simulation is providing methods to use finite elements (COMSOL) to predict experimental results. The ability to show a good correlation between simulation and experimental results is key for potentially design these new tactile sensors using this fabrication process. The simulation know-how should also be vital for INESC-MN development of novel designs and optimizing this because the finite element approach allows us to dimension before fabrication, whether the magnetic or the mechanical requirements.

There was significant demand for practical work, mainly focusing on optimizing parameters, including sensor dimensions, sensitivity, contact resistance, and concrete examples of flexible hybrid processes compatible with spin valves. Optimizing polyimide layers and vias definitions was a novelty at INESC-MN, so the process had to be tailored to the available facilities. The ability to process vias in polyimide layers of 10µm thickness with a diameter of 10µm and an increase in resistance under 0.3 Ω proved to be negligible in the integration with spin valve sensors. Both these arguments are vital to support the argument that spin-valve devices are compatible with flexible hybrid processes. Considering the novel fabrication processes and analog-digital electronic interface, achieving a 3µT detectivity as a digital signal is also significant. The FPC process developed was also helpful on several occasions, specifically for the manual chip placement and integrating the analog-digital interface on the finger.

5.2 Future work

There are four main drivers for future development and integration, which are essential for future devices: better and optimized designs, more standardized and characterization methodologies, improved microfabrication process, and improved electronic interface.

There are two main recommendations to improve the design: the first is to define strategies that minimize spatial positional uncertainty, whether by algorithms or by increasing the number of dimensions Si Chip is sensitive to the magnetic field. At the same time, we should avoid compromising the sensors' density because the higher the sensor density, the better our ability to measure the elastomer deformation should be. This will most likely mean trying to fit the required sensors to improve the position in space without significantly increasing the size of the island. A possible solution would be to have Si islands with sensors sensitive in two-dimensions or 2x2 matrices of one-dimensional sensors. Either would significantly improve our ability to track the position in space. More detailed and in-depth research using the proposed methodology in Chapter 2 would be an excellent starting point. The second strategy to improve design is to simplify the sensor signal reading and reduce the number of variables it depends on, in practice changing the shape, number, or volume of the permanent magnet with that exact purpose. One possible example is to calculate which permanent magnet geometry or combination of magnets could generate a magnetic field that would be proportional in all directions to the displacement of the sensor. This strategy could significantly reduce the complexity and computational time for finding the sensor displacement, as a linear correlation between the H_x and a displacement in x may be possible.

From a fabrication perspective, each process reached different integration levels. For microfabrication, the main challenge is how to go from the Si Island definition step to the injection process. Solving this will require a considerable effort to work around the central fragility of this approach, which is the film stresses of the polyimide and aluminum interconnections. Having strategies such as using the wafer as a mold to inject an elastomer around the Si islands seems to be the best attempt. The manual chip placement process is relatively straightforward, and the main challenges are the placement and handling of the small chips. The solution is to have a more systematic approach, for example, a pick-and-place machine, which would reduce chip placement error and control the conductive epoxy glue dispensed volume. The result should be higher densities as the focus would be to reduce the conductive epoxy volume and, consequently, the pads' size.

Metrics and characterization setup are the most challenging and most impactful drivers for the long-term development of tactile systems. The procedures and characterization tools to qualify tactile sensing for grasping are in early development, but their standardization is critical for developing novel tactile systems.

The use of CMOS and other integration technologies could be very beneficial for this application. As geometrical constraints are critical, miniaturization is essential; thus, CMOS and integrated electronic technologies are a definite plus. This work used discrete elements to read the analog signal from the sensors, but because the rigid part of the flexible hybrid process is silicon, an island could potentially integrate all the electronics. With higher Si Chip densities and a higher number of sensors per Si Chip or both, it becomes critical to solve the number of interconnections since there is a physical limit. Digital communication between islands could potentially be an exciting outcome and bring both the processing and the communication time down while at the same time reducing the number of interconnections.